Università
Ca'Foscari
Venezia

Scuola Dottorale di Ateneo
Graduate School

Dottorato di ricerca
in Scienze Chimiche
Ciclo XXVIII
Anno di discussione 2016

ZIRCONIA ADVANCED CERAMIC MATERIALS FOR FUNCTIONAL AND STRUCTURAL APPLICATIONS

SETTORE DISCIPLINARE DI AFFERENZA: CHIM/02

Tesi di Dottorato di Gabriele Sponchia, matricola 810660

Coordinatore del Dottorato
Prof. Maurizio Selva

Tutore del Dottorando
Prof. Alvise Benedetti

Co-tutore del Dottorando
Prof. Pietro Riello

O sol che sani ogni vista turbata,
tu mi contenti sì quando tu solvi,
che, non men che saver, dubbiar m'aggrata.

Dante Alighieri - If XI, 91-93

Acknowledgements

Dopo altri tre anni di studio e ricerca a Ca' Foscari è giunto il momento, di fare un ringraziamento doveroso e meritato a tutte le persone che hanno contribuito in maniera diretta e indiretta alla preparazione del lavoro di tesi di dottorato.

Il mio relatore prof. Alvise Benedetti e co-relatore prof. Pietro Riello, per avermi dato l'opportunità di svolgere il percorso di dottorato presso il loro gruppo di ricerca, a compimento del mio ormai quasi decennale percorso universitario; la prof.ssa Patrizia Canton, il prof. Elti Cattaruzza e il prof. Giancarlo Battaglin per la cordialità mattutina e durante le pause; la prof.ssa Loretta Storaro, Elisa Moretti, Aldo Talon e Martina Marchiori per il cortese supporto tecnico. Filippo Ghiraldo per la curata stesura e il deposito del brevetto.

Il dr. Goffredo dePortu, per l'accoglienza e la sempre viva disponibilità dimostrata verso il progetto di ricerca e naturalmente i preziosi contatti scientifici. I professori dell'Università di Siviglia Arturo Domínguez Rodríguez, Diego Gómez García, Francisco Luis Cumbrera Hernández e indirettamente Juan Manuel Perez-Mato; il dr. Miguel Castillo Rodríguez per l'amicizia, l'ospitalità durante il mio soggiorno a Siviglia e l'importante aiuto dato alla ricerca. Marco Boffelli e il prof. Giuseppe Pezzotti del KIT di Kyoto per il supporto alla ricerca dal Giappone. Il dott. Flavio Rizzolio per il supporto alla ricerca dal CRO di Aviano. Francesca Guidi per la facilitazione delle questioni burocratiche inerenti dottorato, missioni e rimborsi.

Tutte le *fie*, i *fioi* dell'ETA di via Torino e i fantastici *Venditori di ...* per tutti i momenti belli passati dentro e soprattutto fuori l'università; un immenso grazie a Gloria, Eleonora, Laura, Giulia, Martina, Francesca, Marta, Anna, Michele, Riccardo, Emmanuele, Enrico S, Enrico P, Nicolò, Tommaso, Matteo, Davide e Tiziano.

Infine, come sempre e ancora di più giunti a questo momento, tutti i miei familiari sempre presenti e mai troppo ansiosi nei miei confronti anche durante quest'ultimo triennio.

Un sincero ringraziamento a tutti.

Gabriele Sponchia

Contents

Chapter 1

Introduction

1.1 Aim of the thesis

1.1.1 Background

The aim of the project has been the production of advanced materials based on zirconium oxide (or zirconia, ZrO_2). This particular ceramic oxide is one of the most studied materials both in research and in application fields. Many technological applications have been involved on zirconia-based materials research, thanks to their good mechanical, thermal, functional and sometimes unique properties (see for example Figure 1.1) [1, 2].

The scientific interest about zirconia has been justified mainly by technological and economic motivations. Even if, as reported above, several uses already exist, many others could be exploited, widening the plethora of opportunities. Moreover, it is not clear why some devices show high performance, meanwhile, others manifest different problems during its application. For example, one of the major problems in orthopedics concerns the abrupt mechanical properties loss of the hip joint head (see Subsection 1.2.2 on page 7).

One of the principal aims of material science is to improve the performance of the materials. From this point of view, scientific research has the aim of explaining the reasons for the problem and finding appropriate solutions. As sometimes happens, the search solutions bring to light new knowledge that in turn can lead to new and unexpected use of the same material.

The material science has also the vocation to create new or still unexplored materials. In the last decades, the technological advancement, along with the scientific knowhow, produced many devices with spectacular properties. All this has been developed also thanks to the nanotechnology facility, which is the leading sector in advanced sciences. One of the main characteristics of these facilities are the possibility of producing tailored materials controlling the synthesis parameters.

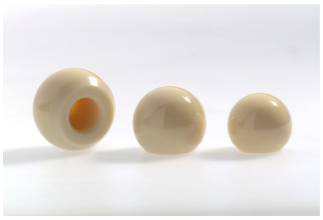

a. Zirconia femoral head

b. Zirconia dental crowns

c. Turbine blades with zirconia coating

d. Knives zirconia blades

e. Diamond-like cubic zirconia gem

Figure 1.1: Examples of zirconia engineering applications.

1.1.2 Project overview

The project has been divided into two parts focused on advanced zirconia-based materials and their characterization.

The first part has been centered on basic structural modification of ZrO_2 in presence of doping *aliovalent* cation. Several modifications of the zirconia system have been explored. First, the classic polymorphs of the zirconium oxide with yttrium Y(III) have been investigated in order to study the well-known engineered zirconia. Oxygen vacancies role with the Cathodoluminescence (CL) technique has been performed in a quite innovative way. The yttrium-stabilized zirconia in co-doped system with europium Eu(III) has also been studied. Europium is a rare earth (RE) cation, so it has luminescent property, which is strong interested by the crystal field surrounding. A study about the controlled monitoring of zirconia tetragonal-to-monoclinic transition, induced by mechanical compression cycles, has been analyzed. A quantitative monitoring of the zirconia phase by luminescence has also been performed. These studies shown a direct correlation between Photoluminescence (PL) and X-ray Diffractometry (XRD) analyses and the possibility to monitoring quantitatively the crystalline phases in an easier way. Another aspect has concerned the possible influence of the oxygen vacancies on the stabilization of the metastable tetragonal phase. Since the literature reports that this phase

is stabilized by oxygen vacancies in a tetragonal lattice (see Subsection 1.2.1 on the next page), it has been verified a possible destabilization mechanism, introducing doping agent with inverse effect, such as tantalum Ta(V). So, in order to destabilize progressively the tetragonal phase, some zirconia powder systems, co-doped with Y, Eu and Ta in different ratios, have been prepared. Luminescence and XRD analyses have been performed in order to check the role of Ta on the oxygen vacancies into zirconia system. Finally, since in literature there is still an interesting and open discussion on the properties of the tantalum-doped zirconia, a detailed study has been carried out preparing and characterized some consolidated samples of the ZrO_2–Ta_2O_5 system by a Spark Plasma Sintering (SPS). This has been made after a detailed study of the crystalline phase developed in powdered samples with a Ta doping in the range 1-20 mol%. This research has also been performed on the base of the experience of the research group on the structure analysis and their transformations of zirconia-based materials [3–7].

The second part of the thesis has been focused on the preparation of tailored zirconia nanoparticles (NPs). This part of the project has been totally new and interesting for the results achieved. The main goal has been the production of zirconia NPs with two main characteristics: mesoporous network and colloidal dimension with controlled shape and size. The samples have been prepared by the sol-gel method along with organic template synthesis. This procedure is well known in literature for other mesoporous materials, such as silica (see Subsection 1.3.1 on page 11), but no many examples are reported for zirconia. The experience about Mesoporous Silica Nanoparticles (MSNs) of the research group has been used as technical background [8–13]. Many variables have been tested during the period of the thesis in order to optimize successfully the process. The good results of the synthesis stimulated the author to investigate the applicability of this optimized system as nanocarrier for drug delivery, biosensing, imaging and theranostic. The high surface area allowed an adequate loading, reducing toxicity of the drug itself. In addition, more than one species (drugs, magnetic NPs, quantum dots) could be loaded into the same carrier with a cooperative and synergetic effect. The external surface could be also functionalized (PEGylation, labelling and targeting agents) in order to favor a pointed treatment of disease and a good final clearance. In this way, Mesoporous Zirconia Nanoparticles (MZNs) could be considered as promising multifunctional platform for delivery, diagnosis and therapy. In the last years nanomedicine produced many efforts in this research field [14]. Even though there are still key barriers that block the laboratory formulations transfer to clinical applications, recent developments on inorganic-based delivery vehicles revealed new horizons for some biomedical applications. The most used inorganic systems are based on MSNs, but also gold NPs, carbon nanotubes (CNTs) and quantum dots (QDs) are extremely interesting

[15, 16]. Among these, MZNs are quite new and less studied as nanocarrier, due to their processing difficulties and have at least three interesting advantages: excellent catalytic activity and selectivity, better chemical inertia than silica or alumina, acid-basic and redox properties at the same time [17, 18]. Furthermore, the guest species (such as phosphors, luminescent or magnetic compounds and drugs) would take a direct advantage from the zirconia host [19–24].

1.2 Zirconia structural materials

1.2.1 State of the art

Zirconium oxide or zirconia (ZrO_2) is an interesting, useful and resourceful metal-oxide. This great versatility it comes from its different crystal modifications. From structural and crystallographic point of view, zirconia has three well-known polymorphs with particular stabilization thermal range: monoclinic (m) until 1170 °C, tetragonal (t) from 1170 °C to 2370 °C and cubic (c) from 2370 °C until the melting point at 2680 °C. At very high pressure other less studied phases (especially orthorhombic) could be obtained. Crystallographic properties of the well-known phases have been reported in Table 1.1. The tridimensional views of the three unit cells have been shown in Figure 1.2.

Table 1.1: Crystallographic parameters of the principal polymorphs of the zirconium oxide. For tetragonal phase, the lattice parameter a and volume in brackets have been reported to compare with the other phases a parity of $Z = 4$.

	Monoclinic (m-ZrO_2)	Tetragonal (t-ZrO_2)	Cubic (c-ZrO_2)
Stability range (°C)	<1170	1170-2370	2370-2680
Space Group (SG)	$P2_1/c$ (14)	$P4_2/nmc$ (137)	$Fm\bar{3}m$ (225)
Z	4	2 (4)	4
Cells parameters	a =5.156 Å b =5.191 Å c =5.304 Å β = 98.9°	a =3.594 Å (a =5.094 Å) c =5.177 Å	a =5.124 Å
Cell volume (Å^3)	140.25	67.16 (134.34)	134.53
Density (g cm^{-3})	5.83	6.10	6.06

The zirconium cation Zr^{4+} has a coordination number of 7 in the monoclinic phase: the four oxygen atoms (O_{II}) have a tetrahedral symmetry with the cation, while the other three oxygen atoms (O_I) are randomly oriented. The O_{II} atoms on the (001) plane are rather mobile and they favor the twinning growth. The tetragonal phase is characterized by a distorted cubic coordination of the eight oxygen atoms around zirconium cation. One tetrahedral is elongated, the other is flattened. The cubic phase has a fluorite-type structure with perfectly eightfold symmetry

of the oxygen atoms. The different Zr(IV) coordination have been represented in Figure 1.3.

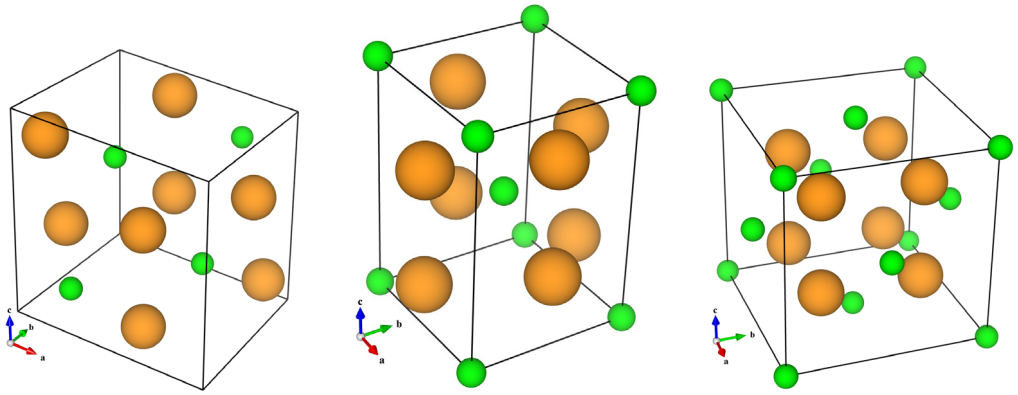

a. Monoclinic **b.** Tetragonal **c.** Cubic

Figure 1.2: Zirconia polymorphs unit cells. Zr^{4+} in green and O^{2-} in orange have been reported, respectively.

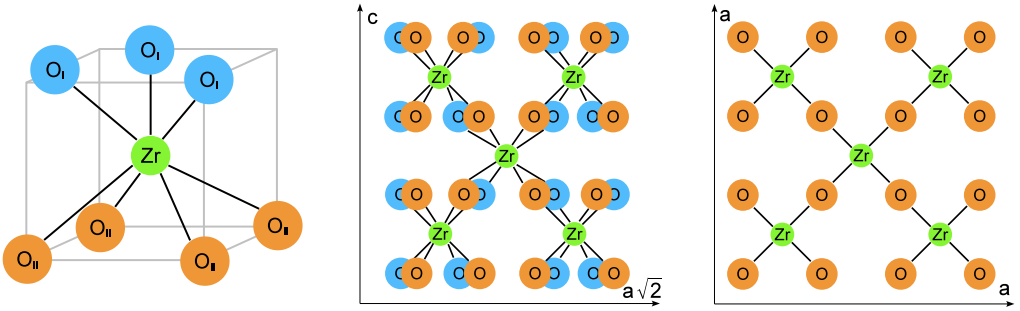

a. Monoclinic **b.** Tetragonal **c.** Cubic

Figure 1.3: Oxygen coordination in zirconia polymorphs.

The tetragonal-to-monoclinic ($t \rightarrow m$) transition starts with a 4% volume expansion and it is a reversible thermal martensitic transformation[1]. It involves a large temperature hysteresis (200 °C) and can be induced by thermal transition or mechanical stress [1, 2, 25]. On heating monoclinic zirconia, the transition occurs at 1170 °C, while during cooling, tetragonal transformation occurs between 850 °C and 1000 °C. From a mechanical point of view, this transformation typically takes place in two stages: first, the transition occurs by shear displacement of Zr^{4+} cations, then the diffusional migration of O^{2-} anions to monoclinic sites symmetry takes place as confirmed also by X-ray Diffractometry (XRD) [26]. The reverse transition is controlled by the diffusional displacements of the respective ions.

[1] A diffusionless shear process characterized by a transformation hysteresis during the heating and cooling cycles.

The $t \rightarrow m$ transition is particularly harmful for the mechanical resistance of the ceramic pieces, causing a fragile fracture. In order to avoid undesirable fractures a stabilization of the tetragonal phase is necessary. This process, known as *Transformation Toughening (TT)*, increases its tenacity producing a stabilized zirconia, defined also as *ceramic steel* [27]. This stabilization can be obtained with the introduction of doping oxides, such as yttria (Y_2O_3), magnesia (MgO), limestone (CaO) or rare-earth oxide (Ln_xO_y) into the structure. At room temperature (RT), different stabilized ceramics can be prepared using suitable amounts of these aliovalent[2] compounds. The final materials could be fully stabilized, such as Full Stabilized Zirconia (FSZ) and Cubic Stabilized Zirconia (CSZ), or only partially stabilized, such as Tetragonal Zirconia Polycrystalline (TZP) and Partially Stabilized Zirconia (PSZ) [1, 2]. The grain size also influences the transformability and the toughness of these ceramics, particularly the smaller is the grain size the higher is the stability. Really, these ceramics are metastable because under stress condition the as-mentioned transformation is activated, with a slow degradation of the mechanical properties. In fact, the TT mechanism implies the $t \rightarrow m$ transition at the edge of the fracture. The volume expansion connected at this transition induces compressive stresses that halt the crack movement. Common employments for these materials are: Thermal Barrier Coatings (TBCs) [28], dental and bone prostheses [29, 30] and high resistance laminates [31]. Finally, also water and vapor can induce a spontaneous hydrothermal degradation at low temperature, known as *Low Temperature Degradation (LTD)* [32].

Since the substituted cations are trivalent (M^{3+}) or bivalent (M^{2+}), a modification of the atomic sites is mandatory, in order to preserve the charge neutrality [1, 2]. In particular, oxygen vacancies into the stabilized zirconia (10-20% of vacancies) have been verified experimentally [33]. This defected structure determines a great anions O^{2-} mobility, high-temperature ionic conductivity and the oxygen vacancies act like positive charge carriers. This mobility is used for the so called probes-λ [3], which are used as gas sensor, such as for engine exhaust gases [34, 35]. Another recent application, based on the vacancies mobility, is the development of zirconia-doped systems as electrolytic part for Solid Oxide Fuel Cells (SOFCs) [36, 37] and in catalysis [38]. The ionic conductivity depends on intrinsic (concentration of stabilizing oxides and impurities) and extrinsic (temperature, atmosphere and time) parameters. When the radius of the dopant cation decreases the conductivity increases. The smaller is the difference between Zr (79 pm) and dopant cation radii the lower is the lattice strain, since the cations association with vacancies is reduced. Lower dopant

[2] Having a different valence respect to the substituted atom or compound.

[3] Oxygen sensors that measure gas partial pressure in carburetors equipped with a three-way catalytic converter.

concentrations do not provide sufficient vacancies for good anions mobility, while higher concentrations give rise to an ordered defected structure, vacancies clusters and electrostatic interactions, which decrease the conductivity [2].

Other important characteristics concern the thermal stability, low thermal conductivity, stress, erosion and fatigue resistance, and superplasticity at high temperature [1, 2, 39]. Thanks to its high-temperature resistance at corrosion, erosion, abrasion and fracture, zirconia found many applications in extreme environmental applications such as oil factory (pumps, valves, nozzles). High performance blades are made in zirconia because of its high resilience. Thermal properties, such as thermal shock resistance (ΔT=300-400 °C), low thermal conductivity (<2 $\mathrm{W\,m^{-1}\,K^{-1}}$) and high Coefficient of Thermal Expansion (CTE) (>$10^{-5}\,\mathrm{K^{-1}}$) are very useful properties utilized for turbine blades TBCs application. Another great advantage is the high temperature chemical resistance that allows the use of these systems as refractory fiber and furnace ceramic additive.

Cubic zirconia could be useful for nuclear waste storage, thanks to its radiative and hydrolytic stability and the possibility to incorporate actinides cations. The cubic zirconia optical properties (refractive index 2.15-2.18) make it much attractive for diamond-like brilliance gems. Moreover, the lower phonon energy (270 (m), 435 (t) and 480 $\mathrm{cm^{-1}}$ (c)), which influences the non-radiative relaxation processes, makes it better than silica (1100 $\mathrm{cm^{-1}}$) for some optical applications [40, 41].

1.2.2 Problems to solve

The most important engineering drawback of the stabilized zirconia is its metastability. There are two phenomena which plague the engineering zirconia ceramic. A schematic view of these problems have been summarized in Figure 1.4.

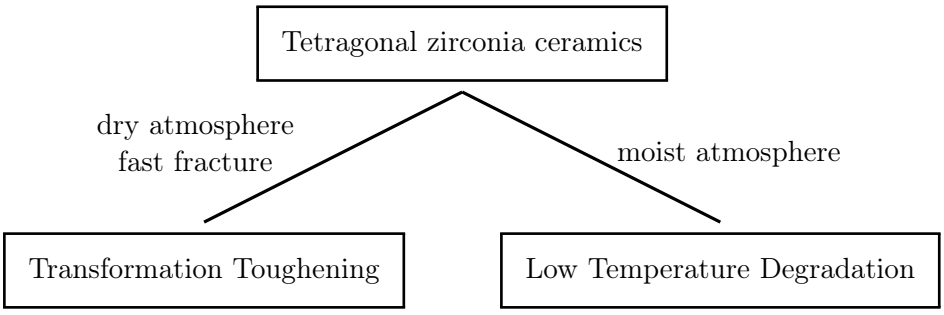

Figure 1.4: Main degradation mechanisms by which metastable tetragonal phase could transform to monoclinic phase.

The above-mentioned toughening mechanism, schematically reported in Figure 1.5, is the cause of zirconia devices failure. The $t \rightarrow m$ transition is related

to the amount of tetragonal phase present in the ceramic. Depending by the working stressed conditions the monoclinic phase amount increases at the edge of the fracture until a complete transition is achieved. So, the aging processes, more o less rapid, causes the mechanical properties decay, sometimes with catastrophic consequences. Even if, during the aging process, the creation of a compressive surface layer of monoclinic phase on the ceramic can benefit certain types of TZP improving the stress resistance for a brief period; further aging treatments, can result in a rapid mechanical deterioration [42].

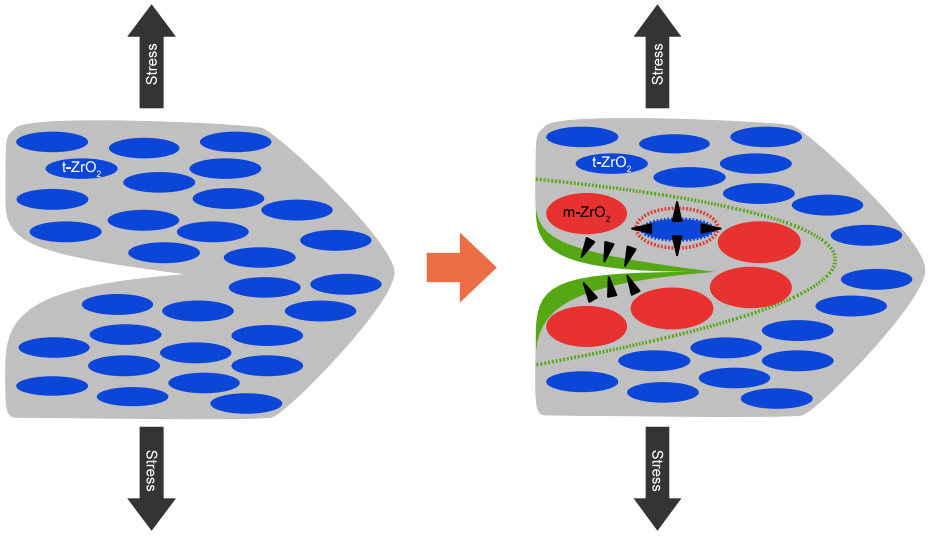

Figure 1.5: Scheme of the Transformation Toughening mechanism at crack edge.

As mentioned previously, the working conditions of the sintered systems play an important role in the final breakdown. In addition to the stresses, moisture and water are responsible for other degradation mechanism, known as Low Temperature Degradation (LTD). This kinetic phenomenon occurs from RT to about 400 °C in presence of moisture and induces a slow $t \rightarrow m$ transformation. It begins at the surface and it could accelerate the ceramic embrittlement in presence of stress. Although the precise mechanism of this destabilization remains uncertainty, it seems that LTD kinetics are similar to oxygen vacancy diffusion. In particular, it could be occurred by the diffusion of hydrated species with similar oxygen vacancy diffusion activation energy. Therefore LTD is an alternative to crack propagation, stress-induced transformation for the $t \rightarrow m$ transition [32]. In Figure 1.6 has been reported a simplified view of this mechanism.

The application of zirconia as orthopedics materials is actually much debated among scientists, industrials and clinicians. Thanks to its already mentioned excel-

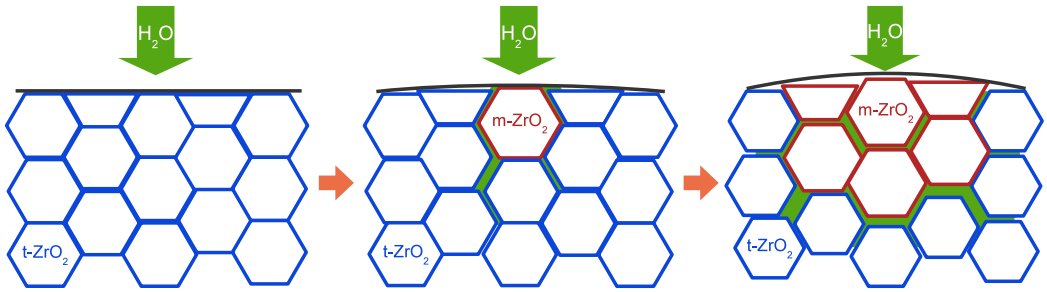

Figure 1.6: Scheme of the Low Temperature Degradation mechanism.

lent fracture toughness (K_{Ic}), stabilized zirconia (with yttria, magnesia or lime) is used for structural applications also for biomedical applications, such as dental and femoral prostheses. In the past, the utilization of zirconia in biomedicine was limited by the production process because of the raw materials (silicates and baddeleyite) contained some radioactive impurity (thorium Th and uranium U). Innovation and better purification process reduced drastically their presence favoring the zirconia applicability. Up to now, there are some disagreements about its use in biomedicine. Just in the 80s, histomorphological tests found out which zirconia should be avoided between bone and prosthesis [43]. Beresford found that the osteoblasts life cycle was interfered by zirconia covers at the interface with the bone [44]. Liu et al. assert that films of materials based on zirconia favor the proliferation of the bone marrow and apatite, and support the cytocompatibility of the same [45]. Other works consider optimal the potential gap-bridging of such type of cover without the connective tissue development [2]. The substitution of femoral heads is one of the most used application field of the zirconia (over 600 000 worldwide implants until 2006), however reports of the English Medical Device Agency (MDA) and the American Food and Drug Administration (FDA) focus the attention on the long-period dangerousness of these prostheses [46].

Biomedical grade zirconia has the best mechanical properties among the oxide ceramics as consequence of the already mentioned mechanism. Zirconia manufacturers assert that the problem was limited *in vivo* situation since 20 years ago, when a few hundred of femoral heads failed in a brief period, with a worst impact for the devices utilization. Even if the failure rate before that moment was very low, many experts declared that it was unacceptable to implant a not fully stable materials in the body [46]. Moreover, even if some excellent behavior [47] contrast with others poor follow up results [48], leaving the debate open, few studies report detailed surface degradation of the implants [49, 50].

In the last years zirconia macroporous carriers demonstrated good coverage ability with osteoconductive hydroxyapatite, but also with osteoinductive proteins[4] [51–53]. Beside the structural applications, zirconia is widely employed as stiffener in biocompatible materials. Pure hydroxyapatite has less mechanical properties than zirconia, so the addition of zirconia pellets increases its strength 2-3 times [54]. This toughening is due to the calcium zirconate ($CaZrO_3$) and to the well-known TT process. Even if $CaZrO_3$ favors the adhesion on the bone, it seems to cause delamination of the coverage decreasing the mechanical properties [55]. Finally, it is worth noting that better properties could be achieved with high-technological deposition techniques, such as plasma, sputtering and spray [2].

1.2.3 Solutions proposed

In order to monitor the zirconia degradation progress, a sensitive quantification is necessary, usually with a structural analysis, such as XRD. Since atoms positions and their coordination change from one phase to other, a crystal field sensitive tool could be a valid choice. Lanthanides cations, in particularly Eu(III), are available as tetragonal zirconia stabilizers. Moreover, its luminescence depends from the surrounding crystal field, which influences the maximum emission wavelength of a particular electronic transition. In this way, a local transformation of the phase can be visible by spectroscopic analysis and the introduction of RE dopant into zirconia, can be a valid tool for the transition $t \rightarrow m$ monitoring [6].

Since the oxygen vacancies are induced by the trivalent (or bivalent) doping cations, pentavalent cations (tantalum Ta(V), vanadium V(V) and niobium Nb(V)) could be used to prevent this type of defect [56, 57]. The possibility to prepare a stable vacancies-free ceramics, or polymorphs, with good mechanical properties can be considered as an excellent result in order to refresh the appeal of zirconia. Some technological advantages are suggested in literature from the production of zirconia tantalum-doped materials, for example a better hot corrosion resistance for TBCs [57–60]. In parallel, some papers evidenced the presence of three orthorhombic phases into zirconia systems, stabilized also by some dopant as MgO, at high pressure and temperature and for some of these systems, with specific composition, detailed structural studies are reported [61–64].

Even though Ta-doped zirconia systems are already studied, very scarce and not always coherent data are available for phase relations on this system [56, 59, 65–67]. The homogeneity range of orthorhombic phase is found to be up to 33 mol% of Ta_2O_5 in ZrO_2 [68]. Some paper reports that the addition of tantalum brings about

[4] Osteoinduction is the process by which osteogenesis is induced. Osteoconduction means that bone grows on a surface. Osseointegration is the stable anchorage of an implant achieved by direct bone-to-implant contact.

the gradual stabilization of the tetragonal zirconia; meanwhile, some others show the presence of an orthorhombic phase. Probably, XRD results are variously interpreted and the too limited range of the X-ray patterns investigated did not highlight the differences between the two phases, which are particularly evident at angles higher than 35° in 2θ. High temperature solid solutions with orthorhombic phase, such as $TaZr_{2.5}O_8$ could be instead formed [68, 69]. Another hypothetical phase reported by Sellar has the formula $Ta_2Zr_8O_{21}$ [70]. In order to investigate the stabilization process of zirconia the project research has been focused on the Ta-doped system, since, as evidenced in literature, higher valence and lower sized cation can stabilize zirconia remarkably [56]. The tantalum alloying into the zirconia systems is expected to suppress the oxygen-ion vacancy formation as a result of the cationic substitution of Zr with Ta.

1.3 Zirconia nanomaterials

1.3.1 State of the art

The long-period experience on silica-based systems and their wide applications produced a very large interest and exploitation of this oxide and it has encouraged the research on other type of oxides with different properties and for different application routes. In the last forty years zirconia, and its modifications, has been used in many high-technological fields as advanced ceramic, thanks to its unique mechanical (as previous reported in Subsection 1.2.1 on page 4) and functional properties [2]. Beside the above-mentioned applications as bulk material, in the last decades few attentions have been focused on the correspondent nanoscaled systems. The template synthesis *via* sol-gel[5], widely employed for silica materials, are used and adapted for preparing zirconia [71–73].

Sol-gel techniques allow preparing inorganic materials starting from organic precursors. *Soft-chemistry* is widely used for tailored materials and nanomaterials production [74]. The main elements that characterize the soft methods are the mild synthesis conditions and the greenest possible reagents. The first that used this term (in French *chimie douce*) was Jacques Livage in the 1977 and in his other publications [75]. In the 70s and the 80s these techniques were developed considerably, even if in the 1968 Stober, Fink, and Bohn had already developed one of the most famous soft-chemistry synthesis for tailored silica spherical NPs [76]. Actually, just in the half of XIX century, Ebelmen and Graham prepared silica gels starting from organic precursors [77, 78]. Other famous scientists that focused many attentions on this research field were Rayleigh e Ostwald, which gave the name at the well-known

[5] *Sol* is a colloidal dispersion solution, while *gel* is a solid integrated network.

Ostwald ripening process[6] [79, 80].

Sol-gel methods are much diffused and flexible techniques for the tailored structural and functional materials [81]. The main reagents are: the matrix precursors, usually alkoxides (M(OR)n), water, some catalyzer, co-solvents and/or complexant agents. The reaction products are similar to inorganic polymers where the cations are bond through *bridging oxygens* as in the glasses. Hydrolysis and condensation are the main and competitive reactions that govern the sol-gel process. Hydrolysis, schematically represented in reaction (R 1.1), forms the partially or totally hydrolyzed units

$$\mathrm{M(OR)_n + H_2O \rightleftharpoons M(OR)_{n-1}(OH) + ROH} \qquad \text{(R 1.1)}$$

as clearly understandable, when the molar ratio alkoxide:water=1:n the hydrolysis is complete. The hydrolyzed units (partially or totally) are involved in the condensation reaction. A nucleophilic attack from one hydroxide (M–OH) or alkoxide (M–OR) group happens as follow

$$\mathrm{M{-}OH + M{-}OX \rightleftharpoons M{-}O{-}M + X{-}OH} \quad \text{with X=H o R} \qquad \text{(R 1.2)}$$

A glass-like network is produced with water or alcohol as byproducts. For high coordination center (Ti(IV) o Zr(IV)) hydroxide bridging is also possibile to achieve [74]

$$\mathrm{M{-}OH + M{-}OX \rightleftharpoons M{-}(OH){-}M{-}OX} \quad \text{with X=H o R} \qquad \text{(R 1.3)}$$

The global reaction for the colloidal suspension (*sol*) depends both from precursors intrinsic and extrinsic factors, such as solvents, induction time and pH. With acid catalysis a terminal units reaction is favored, while with basic catalysis, central units are more reactive. Acid and basic catalysis promote respectively microporous and macroporous systems.

During the gelation of the sol, oligomers species (*cluster*), could react each other forming interconnected network or, alternatively, could grow. The main factors that influence this step are: pH, the sharp increment of viscosity and the gelation time. During the gelation, the solvent swells into the *gel*, and only after its removal, a dry gel is obtained. If the initial structure is preserved an *aerogel* is obtained, otherwise *xerogel* is formed.

In the early 90s, it was published the first examples of mesoporous materials prepared by template synthesis [82, 83]. Taking advantage of the *self-assembly* behavior

[6] Instability of colloidal system where the smaller particles tend to aggregate in order to form bigger and more stable entities.

of *amphiphilic molecules*[7], such as *surfactant*, a *micellar structure* could be obtained and used as template for the sol-gel synthesis. Depending on the type of molecule (cationic, anionic or neutral), its concentration and the environmental conditions, micelle with different shapes and sizes can be prepared. These structures are used as *template* scaffolding for the sol-gel synthesis. After the template removal a porous, ordered or less, network is obtained. Up to now silica has been the main system studied, thanks to the well known chemistry of its alkoxides.

Mesoporous oxide systems are attractive to their high surface area [84]. Moreover, mesoporous zirconia based materials have further additional properties, such as catalytic activity and selectivity, better chemical stability than alumina or silica, amphoteric and redox properties [1, 2, 17]. Except silica, the syntheses of other mesoporous metal-oxide materials require a more careful control of the reaction using the traditional sol-gel techniques. The two most used methodologies are the *soft-template* and the *hard-template* processes. The former involve a surfactant or co-polymer, as structure-directing agent, and an organic oxide precursor [72, 85–87]. The latter use an inorganic material as a scaffold and different oxide precursors can be used [88–90]. The major limits of the soft-template come out during the synthetic process and the surfactant removal. The moisture sensibility and the rapid hydrolysis kinetic of the zirconium alkoxides ($Zr(OR)_4$) is the most problematic issue to control during the synthesis [91, 92]. Calcination process above 400 °C affects the crystallization of the matrix and the porous network loss [72]. Scaffolding procedures allow a best synthesis control, but are time-consuming and usually the final materials are not homogeneous [88, 92], even though some interesting works, on mesoporous nanoscaled zirconia with good surface area, are presented in literature [71, 93].

The first zirconia-based stable porous materials with good specific area, are obtained as mixed oxides materials (silica-zirconia), overcoming the structural problems [84–86, 94–97]. Kaliszewski and Heuer proposed a zirconia powder system washed with alcohol that inhibited the polycondensation between Zr−OH in order to create Zr−O−Zr bridges and limiting the agglomeration [98]. Successively, Mercera et al. studied the zirconia reactivity with other solvents especially for the crystallization step [17]. They evidenced that the polycondensation inhibition is caused by the carbon byproducts derived from the superficial alkyl groups, which acted as monoclinic crystallization nuclei, preserving the porous network. Water washes, instead, favored the tetragonal phase stabilization and, during the phase transformation, the pores volume is reduced. Knowles and Hudson synthesized mesoporous zirconia starting from inorganic precursor (zirconyl chloride $ZrOCl_2$) in presence of ionic surfactant (alkylmetil amine), overcoming the stabilization problem thanks to the double action of the surfactant: it made a template function and reduced the water

[7] Compounds possessing both hydrophilic and lipophilic properties.

surface tension during the calcination step [96]. Ciesla, Schacht, and Stucky prepared mesoporous zirconia with ordered channel with high surface area ($400\,m^2\,g^{-1}$) using surfactant with different length of the alkyl tail [85]. While the thermal treatment at 500 °C induced the loss of porous network, the phosphoric acid processing completes the free Zr−OH groups condensation. In this way, a porous, but irregular, network is preserved. Ciesla et al. also observed how a template approach provided an ordered networks while the scaffolding produced only irregular structures [72]. Another method to prepare more stable structure used the introduction of inorganic anions (sulfate SO_4^{2-} 5-8%wt, and phosphate PO_4^{3-} 10%wt) which coordinate the surfactant molecules instead of water. Kim et al. used zwitterionic[8] surfactants able to bind the cationic zirconia precursors around and to prepare micellar structure [97]. Finally, Pacheco et al. reinforced the mesoporous structure using anionic surfactant (alkyl sulfate and phosphate), which are removed by mild thermal treatment and a successive extraction with ethanol acid solution [86]. Yang et al. used block co-polymers, such as polyethylene oxide (PEO), instead of amphiphilic molecules as template and halide zirconia precursors [87].

In the last decade hard-template techniques have much more been developed. The carbon structures are the most used as molds in these methods [88, 93]. Kang et al. produced a carbon mold starting from SBA-15 silica impregnated with sucrose and calcined in reduced atmosphere in order to promote the carbonization of the sugar. Then, silica is removed by HF wash and the carbon mold has been impregnated with the oxide precursor ($ZrOCl_2$). At the end of the synthesis the template is removed by calcination [88]. This *replica mode* is used also by Liu and Baker for tetragonal zirconia NPs preparation. This system resulted stable until 30 nm, thanks to the Si−O−Zr bridges that stabilized the phase [89]. Also Smått et al. used a nanocasting method with mesoporous silica nanospheres impregnated with $ZrOCl_2$ [90]. After precursor-to-oxide thermal decomposition, silica is removed by NaOH or HF washes and a not-well defined pore distribution is achieved. Liu et al. verified how a strong base post-synthesis processing increased the structure stability with pores of 3–4 nm until 700 °C without phase transition [92]. Weak base, such as ammonia, was less performant because it did not lead completeness condensation of the Zr−O groups.

Recently, Che et al. developed a combined method, called Combination of Soft-templating and Solid-Liquid method (CSSL), where soft-template technique is mixed with solid-liquid method [71]. After a classic soft-template synthesis the materials are mixed with a low melting salt, such as $Mg(NO_3)_2$ (mp=95 °C), which penetrates into the cavities. Calcination removed the organic template, but also induced the MgO crystallization inside the pores. The successive acid etching with HCl generated

[8] A globally neutral molecule that has a positive and a negative electric charge.

a porous structure, with irregular porous with not specific shape.

Other interesting zirconia nanomaterials are processed in the last years. Widoniak, Eiden-Assmann, and Maret developed spherical NPs from 100 to 2000 nm in diameter *via* sol-gel method starting from zirconium alkoxide, water and alcohol [99]. The introduction of alkali halides allowed the particles sizes control. Ballem, Córdoba, and Odén, instead, prepared zirconia NPs using SBA-15 channel as mold and removed it by sonication in basic solution (NaOH) [100].

Only few examples of nanoscopic mesoporous zirconia exists, Dong et al. developed a double casting process, using carbon hard-template, derived from silica NPs [93]. The surface area of these NPs is around $100\,m^2\,g^{-1}$. Caruso's group published another good and inspiring works in the last years [14, 101]. They obtained titania-zirconia mixed mesoporous nanoparticles with very good results.

1.3.2 Problems to solve

The main problem of the non-silica porous materials is the limited thermal stability, which induces a collapse of the network after the template removal [72]. The crystallization of the amorphous gel starts over 300-400 °C. The reorganization from short-range to long-range ordered structure causes the shrinkage of the network with loss of surface area. Usually, tetragonal zirconia can be obtained by crystallization of amorphous zirconia above 300 °C. This transition, known as *glow phenomenon*, is very exothermic [102–105]. The reason why tetragonal rather than the monoclinic phase, the thermodynamic more stable phase, is formed is not completely known, probably a *topotactic transition*[9] occurs. In this way, the manifold structure of materials with the same nominal composition could be explain.

Another problem concerns the chemistry of the organic zirconia precursor. The different chemical behavior and the different oxidation states of the metal cation is other important factors which influence the synthesis. From this point of view, zirconium has only the +4 oxidation state and a chemistry poly-oxide type in water [85]. Zirconium, as other cation with valence IV, is soluble only in a narrow pH range and forms complexes with general formula $MO_x(OH)_y$. So, zirconium does not produce a hydroxide but an oxide. Instead, when the zirconium alkoxides are dissolved in their corresponding parent alcohol, a stable coordination complex with the solvent is achieved. The oxygen of the alcohol gives an electron pair to the cation and a strong bond is formed. This is the case of the isopropanol (i-PrOH), which forms with $Zr(OPr)_4$ a stable complex. The ionic character of the metal-oxygen bond depends on the size and on the electronegativity of the metal atom. Considering the Pauling scale[10], the metal-oxygen bond is half covalent when the difference between

[9] Local and selective transition which interests any non-crystalline structure in one crystalline.

[10] Dimensionless scale that quantify the electronegativity of the elements, *i.e.* the atom tendency

their electronegativity is ≤ 1.7. For this reason, silicon alkoxides, differently from the metal salts in solutions, are sufficiently covalent to react. The solvents which dissolve the alkoxides, accentuate this effect because are weaker ionizable than water. For these alkoxide, water is considered as a reactant rather than a solvent, allowing better control of the hydrolysis that in the case of metal salts, if added carefully during the sol-gel process [106].

The sol-gel methods are well-studied and optimized for silica materials, but for other metal-oxides the above-mentioned scheme is more complex [91]. The main problem is the nature of the precursor itself. Generally, the alkoxides are more reactive in presence of heat, moisture and light. In particular, the zirconium alkoxides are more reactive than silanes, *e.g.* zirconium precursor reacts 10^5 times faster, causing an unchecked oxide precipitation. The main reason is that the *d*-block metals have a greater tendency to made complexes, unlike the *p*-block elements. This behavior is well explained by the partial charge model [106]. Their high Lewis basicity favors the ligands exchange, with a proton-assisted S_N1 mechanism[11]. It should be noted that the reaction rate is controlled by the acidity of the hydrogenated reactant (HM), while the nucleophilic properties of the entering M^- species have not any effect on the ligand exchange process. During the hydrolysis step of the zirconium alkoxides, the −OR groups are replaced with water and oxygen as in the reaction (R 1.4) [106]

$$\mathrm{Zr(OR)_x(OH)_y} \rightleftharpoons \mathrm{ZrO_{x-x_0}(OR)_{x_0}(OH)_{y-x+x_0}} + \mathrm{(x-x_0)ROH} \qquad \text{(R 1.4)}$$

As explained by Mazdiyasni this mechanism can be divided in two steps [107]. First, a hydroxyl group replaces a −OR, and then there is an alcohol removal with double bond Zr=O formation. These steps happen twice and a unit ZrO_2 is formed. The first step is slower, but the reaction kinetic depends only by initial concentration of the precursor. Since hydrolysis is faster than condensation, the final product is a hydrated zirconia cluster ($ZrO_2 \cdot xH_2O$) with somewhat variable structure. In order to decrease the reaction rate apolar solvents, complexing agents or moisture control could be used. The reaction could be slowed down by adding a sub-stoichiometric water quantity. Again, the longer is the alkyl groups the harder is the O−R bonds, furthermore beyond the first hydrolysis, a hydoxide group unlikely substitutes an alkoxy ligand.

In the 70s substituting the alkoxides groups with organic *chelates*[12] (*β*-diketones, carboxylic acids, etc.) produced stable sols [91]. The proposed description was that

to attract electrons.

[11] A nucleophilic substitution that occurs with a unimolecular rate-determining step.

[12] Compounds with ligand (usually organic) bonded to a central metal atom at two or more points.

the presence of chelating ligands: a) not changed the charge distribution, b) blocked the metal atoms coordination sites, and c) protected the metal atoms from condensation by non-hydrolysable and not removable ligands. In the view of the data available by Kessler et al. on reaction mechanism, this explanation did not appear reasonable. The authors demonstrated as the metal alkoxide precursors reactivity increased upon addition of modifying ligands, and caused the ligand exchange. However, the whole sol formation is not directed by kinetics of hydrolysis and condensation, but by the self-assembly of ligands. The complex, therefore, favored an alternative heterogenous reaction route. Liu et al. verified as the acetylacetone during the synthesis could stabilized the $Zr(OPr)_4$ hydrolysis but an excess could slowed down the gelation time [92].

1.3.3 Solutions proposed

Soft-template approaches, with respect to hard-template syntheses, are greener, use milder reaction conditions and are less time-consuming. Moreover, sol-gel method allows to manage the material adjusting environmental and reaction parameters. Since, for zirconium alkoxide, kinetic precursor reaction must be slowed down, a thermal control during the reaction is fundamental. Temperature should be maintained around RT, since the zirconia precursors reacts 10^5 times faster than silica ones.

In order to avoid NPs uncontrollable growth, the slowing down of the hydrolysis kinetic is mandatory. One of the possibilities is to limit the amount of water, in this way, a controlled growth could be reached. The presence of water is however fundamental for the sol-gel processing. A well-known method to stabilize NPs shape and size is the introduction of ionic compounds, usually alkali salts. Many examples of ionic strength particles size-dependent effect are reported in literature for different type of oxides [99, 108, 109]. Aqueous salt solution it is a good compromise to control the kinetics and particles growth at the same time. Mixing the precursor with compatible solvent, such as alcohol, is another way to reduce the kinetic reaction, since, a sort of chelating reaction happens. However, the morphological properties of the particles, however, are better controlled by hydrothermal processing, after the gel production. This type of treatment is well-known and very used for the production of porous materials [110].

In order to go beyond the porous network loss problem connected to template removal, an alternative to calcination step has to be searched. Thermal degradation of the organic scaffold structure starts over 300-400 °C, *i.e.* at the same temperature of amorphous-to-crystal transition. Chemical washing could be taken, as alternative to clean the pores from the organic but amorphous zirconia is sensitive to acid,

which can erode the particles. Physical extraction, exploiting the status diagram could be chosen as valid alternative, as proposed by Prado and Airoldi [111]. Using a vacuum system along with thermostatic bath the correct condition for the surfactant extraction could be reached without causing significant structure shrinking [112].

Chapter 2

Experimental Part

2.1 Zirconia powders and structural materials

2.1.1 Materials

The reagents used for the samples preparation, listed in Table 2.1, have been used as received without further purification.

Table 2.1: Reagents' specifications.

Reagents	Abbreviation	Purity	PM (uma)	Density ($g\,cm^{-3}$)	Supplier
ethanol	EtOH	99.8%	46.07	0.79	Aldrich
ammonium hydroxide	NH_4OH	28 wt%	35.05	0.88	Fluka
zirconyl chloride octahydrate	$ZrOCl_2 \cdot 8\,H_2O$	98%	322.25	1.91	Aldrich
yttrium(III) chloride hexahydrate	$YCl_3 \cdot 6\,H_2O$	99.9%	303.96	2.18	Aldrich
europium(III) chloride hexahydrate	$EuCl_3 \cdot 6\,H_2O$	99.9%	366.41	4.89	Aldrich
tantalum(V) chloride	$TaCl_5$	99.8%	358.21	3.68	Aldrich

2.1.2 Materials processing

Synthesis of powder samples

All the zirconia powders (Y, Eu and/or Ta-doped) have been prepared *via* the base-catalyzed co-precipitation method, already used for other similar works [6]. Briefly, the precursor ethanol solutions (0.3 M $ZrOCl_2 \cdot 8\,H_2O$, 35 mM $YCl_3 \cdot 6\,H_2O$, 50 mM $EuCl_3 \cdot 6\,H_2O$ and/or 12.5 mM $TaCl_5$) have been mixed together in different amounts and stirred at room temperature (RT). The corresponding hydroxides co-precipitation has been achieved by dropwise addition of aqueous ammonia solution (three-molar excess). After 20 min of stirring at RT, the hydroxides have been centrifuged (9000 rpm for 30 min) and washed once with distilled water and three times with EtOH to remove the ammonia excess and the unreacted precursors.

Then, the wet powders have been dried at 130 °C for 12 hours. Finally, the as-obtained powders have been calcined in air at 1000 °C for 6 hours to promote the crystallization process.

The zirconia single-doped and co-doped samples series have been listed in Table 2.2. The final number stays for the molar percentage of the dopant, for the ZYET series the Y (3.5%) and Eu (0.5%) contents have been constant.

Table 2.2: Zirconia single-doped and co-doped powder samples series.

ZY series	ZYET series	ZT series
ZY1	ZYET1	ZT1
ZY3	ZYET2	ZT3
ZY4	ZYET3	ZT4
ZY5	ZYET4	ZT5
ZY8	ZYET5	ZT8
ZY12	ZYET7	ZT12
ZY20	ZYET8	ZT20
	ZYET9	
	ZYET10	

For the luminescent study of the tetragonal zirconia phase degradation three sample have been prepared, $Zr_{0.96}Eu_{0.04}O_{1.98}$ (ZE series), $Zr_{0.96}Y_{0.035}Eu_{0.005}O_{1.98}$ (ZYE series) and $Zr_{0.995}Eu_{0.005}O_{1.9975}$ (ZEM). The sample labels and their specifications have been reported in Table 2.3.

Table 2.3: Eu-doped and Eu,Y-doped zirconia series.

Processing	ZE series	ZYE series
As obtained	ZE0 and ZEM	ZYE0
After mild mortar ground	ZE1	ZYE1
After 3 GPa applied compression	ZE2	ZYE2
After 6 GPa applied compression	ZE3	ZYE3
After 9 GPa applied compression	ZE4	ZYE4
After ball milling	ZE5	ZYE5

Powder consolidation process

The consolidation process of the zirconia Ta-doped powders (ZT5, ZT8, ZT12) *via* Spark Plasma Sintering (SPS) has been performed with two different experimental conditions sets: a) T=1250 °C, P=75 MPa, t=5 min (SPS1250 series), b) T=1150 °C, P=100 MPa, t=5 min (SPS1150 series). Lower sintering temperature needs higher sintering pressure in order to reach a good final density of the specimen.

Spark Plasma Sintering technique

Spark Plasma Sintering (SPS) is a modern and very interesting sintering technique. Even if the technology related to current assisted sintering processes started in the late 30s of the XX century, a lack of application technology at that years limited its applicability. The advent of the modern SPS technique must be moved to the 90s, also known as the third generation SPS [113].

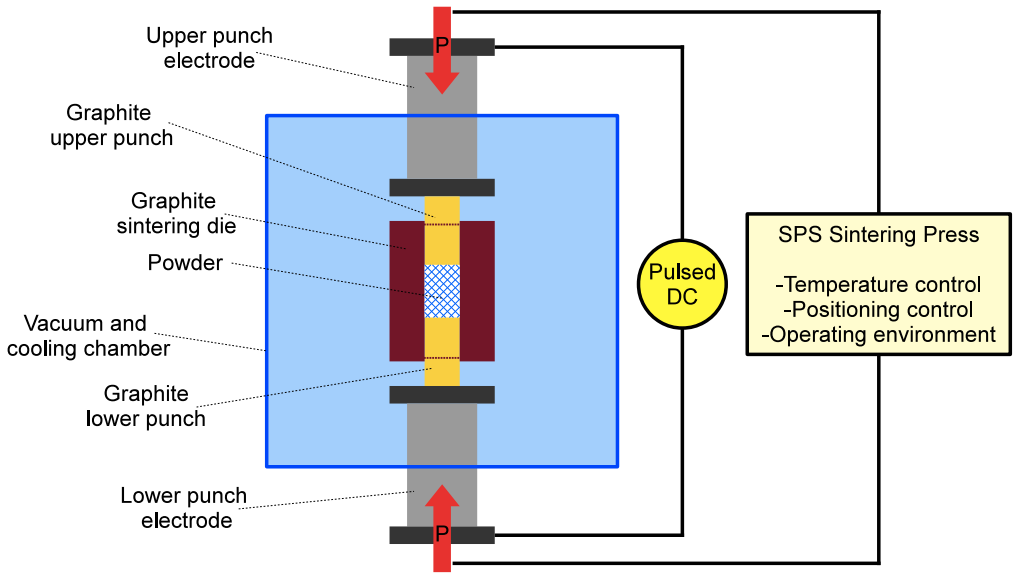

Figure 2.1: Scheme of a SPS equipment.

The process, which works at low atmospheric pressure, uses uniaxial force and a pulsed direct current (DC) to perform high-speed powder consolidation. A direct way of heating allows the application of very high heating and cooling rates, enhancing densification and maintaining the nanopowders properties into the full-dense materials. The sintering process is very rapid in order to avoid too much growth of the grain size. SPS system offers some advantages over conventional systems, such as hot press (HP) sintering, hot isostatic pressing (HIP) or atmospheric furnaces. An accurate control of the sintering energy, high sintering speed, high reproducibility, safety and reliability are the main characteristics of this process. The application of the electric current allows reaching a very rapid and efficient heating, with a rate as high as 1000 °C/ min. So the total processing time usually takes some minutes depending on the material and its dimension. Finally, the sintering temperatures range is almost 500 °C lower than the conventional ones.

SPS equipment, schematically proposed in Figure 2.1, comprises a hydraulic

press inside a heating chamber, moreover the press punches act also as electrode in order to allow the current passage. The sample holder is formed by a graphite die, which contains the powder, and it is closed by two graphite punches. This sandwich is put inside the heating press.

In origin it was claimed that the release of electric energy *via* arcing at the empties between powders could create local plasma enhancing the mass transport at the neck regions achieving a better densification. The electrical spark discharge phenomenon is the basis of the SPS process. A high energy low voltage spark pulse current produces a momentary *spark plasma* at the high localized temperatures between the particles in order to achieve a good thermal and electrolytic diffusion. The particles contact ionization, caused by spark discharges, develops impulsive pressures that promote high-speed diffusion and migration of the atoms at the contact zones. This is reason of the process name, even if, no plasma generation it has been confirmed directly by experiments yet. The existence of plasma is still discussed, but it is broadly accepted that sporadic electric discharges could take place on a microscopic level.

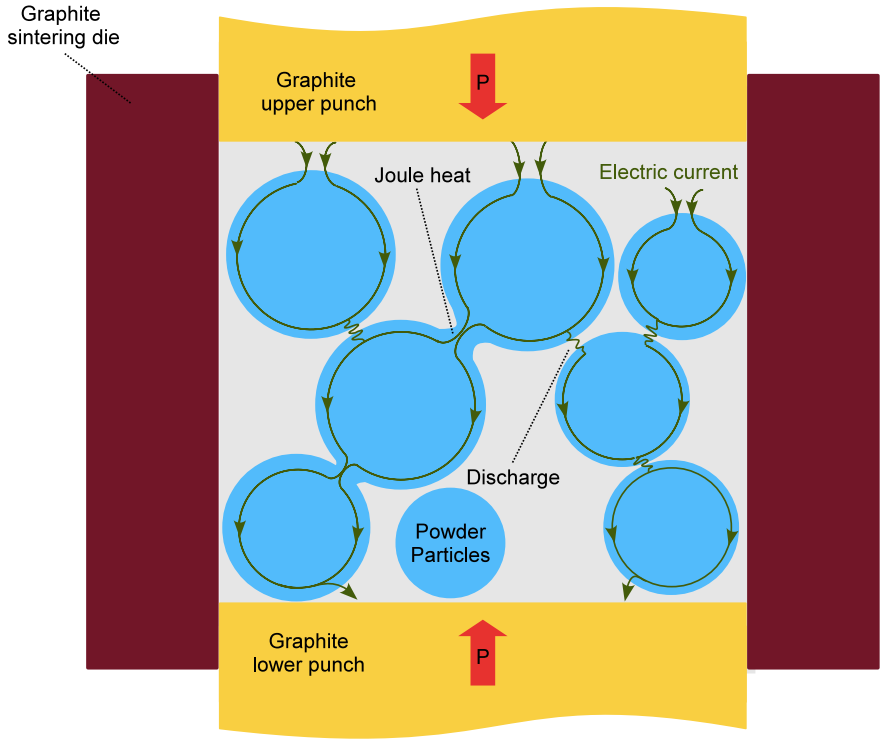

Figure 2.2: Pulsed current flow through the powder particles during the SPS sintering.

Under mechanical pressure, the electric current passage through the particles is supported by *Joule heating*[1] during the welding of the particles. This intense heating effect on the particle conducting surface, can reached the boiling point leading a localized vaporization, or cleaning of the powders surfaces, that ensures a good path for the current flow. So, the DC pulse energizing method generates four phenomena: spark plasma, spark impact pressure, Joule heating and an electrical field diffusion effect. In the SPS process, the powder particle surfaces are purified and activated, so a high-quality sintered compact is achieved at lower temperature and faster. The first two already mentioned phenomena (spark plasma and spark impact pressure) eliminate the adsorptive gas and the impurities on the particles surface thanks to the high temperature generated. When a spark discharge appears in a gap or at the contact point between the particles, evaporation and melting on the surface occurs and *necks* are formed. The heat moved from the center of the discharge column to the surface then the intergranular bonding is rapidly cooled. In Figure 2.2 a scheme of the pulsed current flow through the powder particles is reported.

2.1.3 Characterization

The microstructure of the powders has been studied by means of X-ray Powders Diffractometry (XRPD). A Philips X'Pert vertical goniometer with Bragg-Brentano geometry, has been used for all the XRPD measurements; a focusing graphite monochromator and a proportional counter with a pulse-height discriminator have been used, Nickel-filtered Cu$K\alpha$ radiation and a step-by-step technique have been employed (steps of 0.05° 2 h), with collection times of 10 s/step. These measurements have been performed c/o the Scientific Campus (ETA building) of the Università Ca' Foscari in Venezia-Mestre (VE, Italy). The *in situ* temperature XRPD measurements have been collected at the ELETTRA Laboratories of Sincrotrone Trieste S.C.p.A. (Line MCX) in Basovizza (TS, Italy) using a quartz glass capillary as sample holder [114]. The synchrotron light power has been 15 keV (λ =0.824 58 Å).

Raman spectra have been acquired with using a confocal (optical) microprobe from different areas of the samples at RT using a single monochromator (T-64000, Jobin-Ivon/Horiba Group, Kyoto, Japan) equipped with a nitrogen-cooled 1024×256 pixels CCD camera (CCD-3500V, Horiba Ltd., Kyoto, Japan), and analyzed by using commercially available software (Labspec, Horiba/Jobin-Yvon, Kyoto, Japan). The excitation frequency used has been the 532 nm green line of an Nd:YAG diode laser operating with a power of 12 mW. The spectrum integration time has been typically 30 s, the final spectrum as average of three measurements has been obtained. A confocal configuration of the Raman probe has been performed using a

[1] Also known as *ohmic* or *resistive* heating, is the heating process produced by the electric current passage through a conductor.

100× objective lens in order to exclude the out-of-regions scattered photons. Width and spectral positions of the selected Raman bands have been obtained upon fitting the collected spectra with Lorentzian curves. The Cathodoluminescence (CL) spectroscopy has been performed inside the chamber of a Field-Emission gun Scanning Electron Microscope (FE-SEM), equipped with an Schottky-emission type gun (S-4300SE, Hitachi, Tokyo, Japan) as the excitation source, with an acceleration voltage at 5 kV, and the probe current has been fixed at 180 pA. A high-sensitivity CL detector unit (MP-32FE, Horiba Ltd., Kyoto, Japan) has been employed for the collection of CL emission upon reflection into an ellipsoidal mirror and transmission through a bundle of optical fibers, using a high-resolution monochromator (TRIAX 320, Jobin-Ivon-Spex, Kyoto, Japan) equipped with a nitrogen-cooled 1024×256 pixel CCD camera (CCD-3500 V, Horiba Ltd., Kyoto, Japan). All experiments have been performed using a grating of 150 grooves mm^{-1}, 10 s of integration time and 500 nm of electron beam spot size. The average spectra have been computed from 20 randomly collected spectra for each sample. The ZY series samples have been coated with 10 nm of platinum by sputtering method and fixed with carbon tape to an aluminum sample holder. The Kyoto Institute of Technology (KIT) in Kyoto (Japan) has been made all these instruments available.

The SPS consolidation processing with a Dr. Sinter Lab SPS 515S equipment has been performed. Compression stress-strain tests with a Zwick/Roell ZMart.Pro 1185 equipment has been made. The creep tests have been performed with a home-made machine. A Bruker D8I-90 with Bragg-Brentano geometry, connected to a highly stabilized generator (40 kV), has been used for the Wide Angle X-ray Scattering (WAXS) measurements on the sintered specimens and for the XRPD measurements for the direct analysis of the pattern to solve the powder structure of ZT12 sample. The Universidad de Sevilla laboratories c/o the Departmento de Fisica de la Materia Condensada (Apartado 1065-41080, Sevilla, Spain) has been made all these instruments available.

Grain size distribution, compositional Energy Dispersive X-ray Spectrometry (EDS) analyses, Backscattered Electrons (BSE) and Secondary Electrons (SE) images have been preformed with a Zeiss Sigma VP FE-SEM c/o the Centro di Microscopia "Giovanni Stevanato" in Venezia-Mestre (VE, Italy). In order to evidence the grain boundaries on the SPS specimens, the surface have been polished (lapping with diamond paste until 1 µm) and then have been annealed at one hundred degree lower respect to the SPS temperature.

2.2 Mesoporous Zirconia Nanoparticles

2.2.1 Materials

The reagents used for the samples preparation, listed in Table 2.4, have been used as received without further purification.

Table 2.4: Reagents' specifications.

Reagents	Abbreviation	Purity	PM (uma)	Density ($g\,cm^{-3}$)	Supplier
ethanol	EtOH	99.8%	46.07	0.79	Aldrich
hexadecylamine	HDA	90%	241.46	0.81	Alfa Aesar
octadecylamine	ODA	90%	269.51	0.86	Aldrich
zirconium propoxide	ZP	70% in PrOH	327.58	1.04	Fluka
sodium chloride	NaCl	99.5%	58.44	2.16	Fluka
lithium chloride	LiCl	99%	42.36	2.07	Eurobio
potassium chloride	KCl	99.5%	74.56	1.98	Aldrich
rubidium chloride	RbCl	99%	120.92	2.80	Aldrich
cesium chloride	CsCl	99.9%	168.36	3.99	Aldrich
sodium fluoride	NaF	99%	41.99	2.56	Fluka
sodium bromide	NaBr	99%	102.90	3.21	Carlo Erba
sodium iodide	NaI	99%	149.89	3.67	Aldrich

2.2.2 Experimental procedures

Synthesis of MZNs

The MZNs synthesis has been refined from the method proposed by Chen et al. starting from the zirconium propoxide (ZP) precursor and working at RT [101]. An ethanol solution of the surfactant amine, hexadecylamine (HDA) has been prepared, then the alkali halides (MX) aqueous solution has been added in a correct quantity. An ethanol zirconia precursor solution has been prepared and then it has been added dropwise into the primary solution under vigorous stirring. The preferred molar ratio ZP: EtOH: H_2O: MX: HDA has been 1: 750: 20: 0.02: 2. After synthesis, an ethanol washing has been performed three times. A hydrothermal processing at 170 °C for 20 h of the dried powder in 6.25 ml of water and 12.5 ml of EtOH per gram of powder, into a Teflon bomb has been performed. A heat vacuum extraction process at 120 °C, in order to remove the surfactant without structural undesirable alterations has finally been performed on the dried powders [111]. In order to explore the synthesis dynamics, different alkali halides (MX, where M:Li, Na, K, Rb and Cs; and X:F, Cl, Br and I) as shape and growth controller agents have been tested; different volume of water, salts solution and surfactant have also been tested.

Cytotoxicity assay

Two cell lines (HeLa and MDA-MB-231) have been used to test *in vitro* cytotoxicity of MZNs. Briefly, 96 well plates with 3 000 cells/well have been prepared using a Dulbecco's Modified Eagle's Medium (DMEM). The MZNs have been added at the medium, after an overnight incubation time, starting from $4\,\mathrm{mg\,ml^{-1}}$ concentration and doing nine 1:2 serial dilutions. These tests have been replicated three times. The cell viability has been estimated, after 96 hours of incubation time, by reading the luminescence (Cell Titer) compared to untreated wells with a Tecan F200 instrument (Tecan, Maennedorf, Switzerland).

In vivo biodistribution

Nude mice have been procured from Harlan Laboratories and the procedures have been approved by the Institutional Ethical Committee for Animal Experimentation (CESA) and performed in accordance with the institutional guidelines. MZNs (1 mg) with lipophilic tracer DiR (Invitrogen, Carlsbad, CA, USA) and injected intravenous has been probed. After one hour, the mice have been imaged with an *In Vivo* Imaging System (IVIS) instrument (PerkinElmer, Waltham, MA, USA).

Biodegradation

Several aliquots of MZNs in human plasma with $2\,\mathrm{mg\,ml^{-1}}$ final concentration have been suspended and incubated with agitation at 37 °C. Single aliquots at 10^4 g for 5 min have been centrifuged and observed at different incubation times (0, 5, 10, 15, 30 and 60 days). Pellets containing MZNs have been collected, washed and dried out. For every time point, FE-SEM images have been taken and the average diameters have been measured using the ImageJ software. At least 50 NPs for each sample have been used for the mean diameters and the standard deviation determination. A Student's t-test for the statistical analysis has been performed and for $p < 0.01$ the differences have been considered significant, using the 0 day sample value as reference.

Drug loading and release

A simple wet impregnation method has been used as protocol for the anti-tumor molecules loading into the MZNs. A precise amount of MZNs in 1.0 ml of buffer solution containing doxorubicin (DOX) has been dispersed. The NPs working concentration has been $5\,\mathrm{mg\,ml^{-1}}$ and drug has been used at $1.0\,\mathrm{mg\,ml^{-1}}$ final concentration. The solution, protected by the light and at RT, has been stirred overnight. Impregnated MZNs by centrifugation (10 min at 10^4 rpm) have been recollected and

the free drug concentration into the supernatant, by ultraviolet-visible (UV-Vis) absorption at a wavelength of 480 nm has been determined. The drug loading amount has been calculated as follow

$$\text{Loading } (\%) = \frac{\text{Initial amount of DOX} - \text{Residual DOX content}}{\text{NPs amount}} 100 \tag{2.1}$$

The MZNs DOX-loaded have been resuspended ($1.0\,\text{mg}\,\text{ml}^{-1}$) in different phosphate buffers (pH 4.0, 5.5, 7.0 and 8.5) and left under agitation for 24 h protected from light. Released supernatant DOX concentration by UV-Vis absorption has been determined, after MZNs removal by centrifugation. Release percentage has been calculated respect to the starting DOX content

$$\text{Release } (\%) = \frac{\text{Supernatant free DOX}}{\text{Starting encapsulated DOX}} 100 \tag{2.2}$$

The experience has been repeated three times and the average value with the standard deviation has been reported.

2.2.3 Characterization

The nitrogen physisorption measurements have been collected at liquid nitrogen temperature (−196 °C) using a Micromeritics ASAP 2010 volumetric adsorption analyzer. The Brunauer Emmett Teller (BET) equation has been used to calculate the specific surface area from the adsorption branches data, the pore size distributions have been calculated from the desorption branches of the isotherms based on the Barrett Joyner Halenda (BJH) model. The Diffuse Reflectance Fourier Transform Infrared Spectroscopy (DRIFT-IR) spectra with a NEXUS-FT-IR instrument implementing a Nicolet AVATAR Diffuse Reflectance accessory have been recorded. The Thermogravimetric Analysis (TGA) and the Differential Scanning Calorimetry (DSC) with a Netzsch STA 409C have been performed in air from 30 °C to 900 °C with a heating rate of 10 °C/ min. A Philips X'Pert vertical goniometer with Bragg-Brentano geometry has been used for the XRPD measurements; a focusing graphite monochromator and a proportional counter with a pulse-height discriminator have been used, Nickel-filtered Cu$K\alpha$ radiation and a step-by-step technique have been employed (steps of 0.05° 2 h), with collection times of 10 s/step. All these measurements have been performed c/o the Scientific Campus (ETA building) of the Università Ca' Foscari in Venezia-Mestre (VE, Italy). The dimensions and the morphologies of the nanoparticles have been studied by electron microscopy using a Zeiss Sigma VP FE-SEM c/o the Centro di Microscopia "Giovanni Stevanato" in Venezia-Mestre (VE, Italy).

1×10^5 MDA-MB-231 cells have been plated on poly-D-Lysine treated slides and marked with Histone Marker GFP (CellLight® Reagents BacMam 2.0)(Life technology, Carlsbad, CA, USA) one day after. MZNs with Vybrant® DiI lipophilic labeling solution (Life Technology, Carlsbad, CA, USA) have been labeled, then washed in Phosphate Buffered Saline (PBS) and incubated with the cells for 2 hours. Cells with 4% para-formaldehyde for 10 minutes have been fixed, washed twice with PBS and mounted with anti-fade mountain solution (CALIBIOCHEM FluorSave Reagent). Images with an inverted fluorescence microscope (Nikon TE300) equipped with a confocal module (UltraVIEW, Perkin Elmer) and analyzed with the Andor Technology™iQ Classic software package have been collected. All the images have been acquired with a 100× objective. The biological characterization have been performed c/o the Centro di Riferimento Oncologico (CRO) laboratories in Aviano (PN, Italy).

Chapter 3

Results and Discussions

3.1 Zirconia Yttrium-doped powders

X-ray Powders Diffractometry (XRPD)

The better-known system, yttrium-doped series (ZY), has been first investigated. Seven samples with different Y^{3+} amount, between 1-20 mol%, have been prepared. The diffraction patterns of all the samples have been proposed in Figure 3.1, while the quantitative data derived from the Rietveld refinements have been shown in Table 3.1.

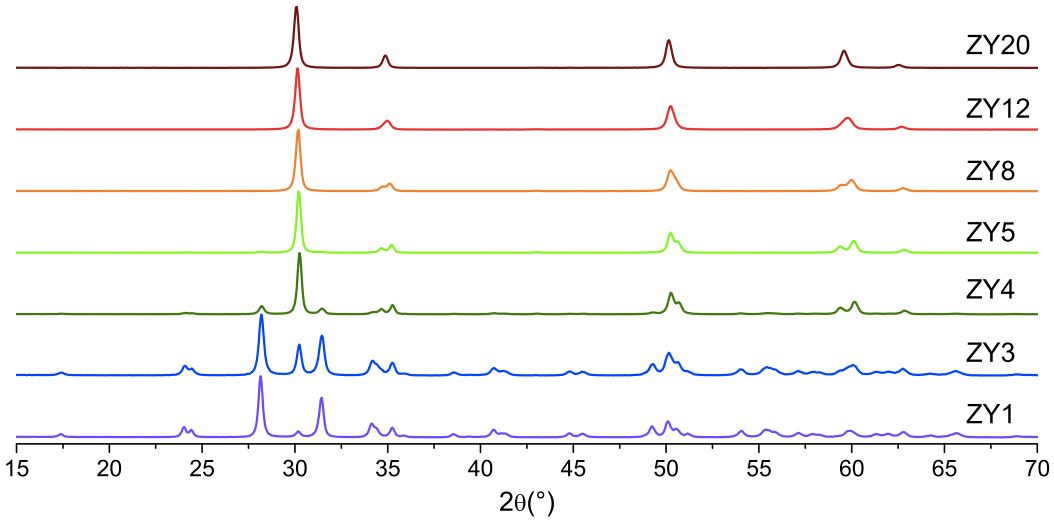

Figure 3.1: XRPD patterns of ZY series.

The XRPD data evidence the tetragonal phase growth together with the dopant percentage, until 12 mol%. The last sample (ZY20) is characterized by a more symmetric symmetry, the cubic one. The major difference between cubic and tetragonal patterns is represented by the disappearance of the peak at $2\theta = 43°$ in the former,

Table 3.1: Volume fractions of tetragonal phases for the ZY series, as obtained by the Rietveld refinements.

Sample	t-ZrO_2 (%)
ZY1	4.9
ZY3	18.4
ZY4	74.9
ZY5	96.6
ZY8	100
ZY12	100

as visible in Figure 3.2 (the peak marked with a star $*$). As well-known, a content of yttria (Y_2O_3) higher than 4 mol% stabilizes the tetragonal phase at RT, while the cubic phase of zirconia is stabilized over the 10 mol% of yttria [1].

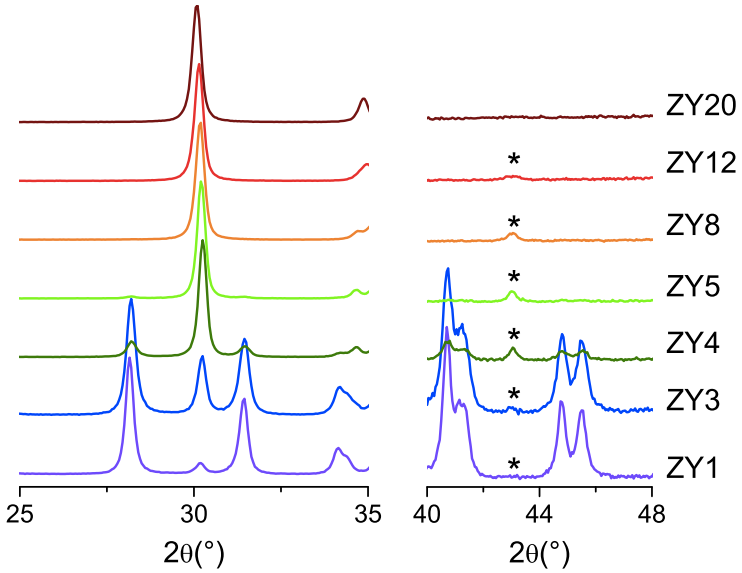

Figure 3.2: Particulars of the XRPD patterns of ZY series.

Raman Spectroscopy

The Raman spectra of the samples are in perfect agreement with the already reported XRPD data. All spectra have been presented in Figure 3.3 .

As clearly shown in the same figure, the spectra change from ZY1 to ZY20 sample. As predicted from theory, the monoclinic and the tetragonal symmetry have 18 and 6 Raman-active modes[1] respectively [115, 116]. As reported in the

[1]A vibrational mode is Raman-active when the molecular electric dipole-electric polarizability changes with respect to the vibrational coordinate corresponding to the rotational and vibrational state.

previous paragraph, the first two samples (ZY1 and ZY3) show the presence of a little amount of tetragonal polymorph. Over the 4 mol% of doping cation the tetragonal characteristic peaks increase together with the relative phase content. In parallel, the more intense peaks of monoclinic phase decrease until disappear in the last three samples (ZY8, ZY12 and ZY20). The ZY20 spectrum presents only the cubic phase.

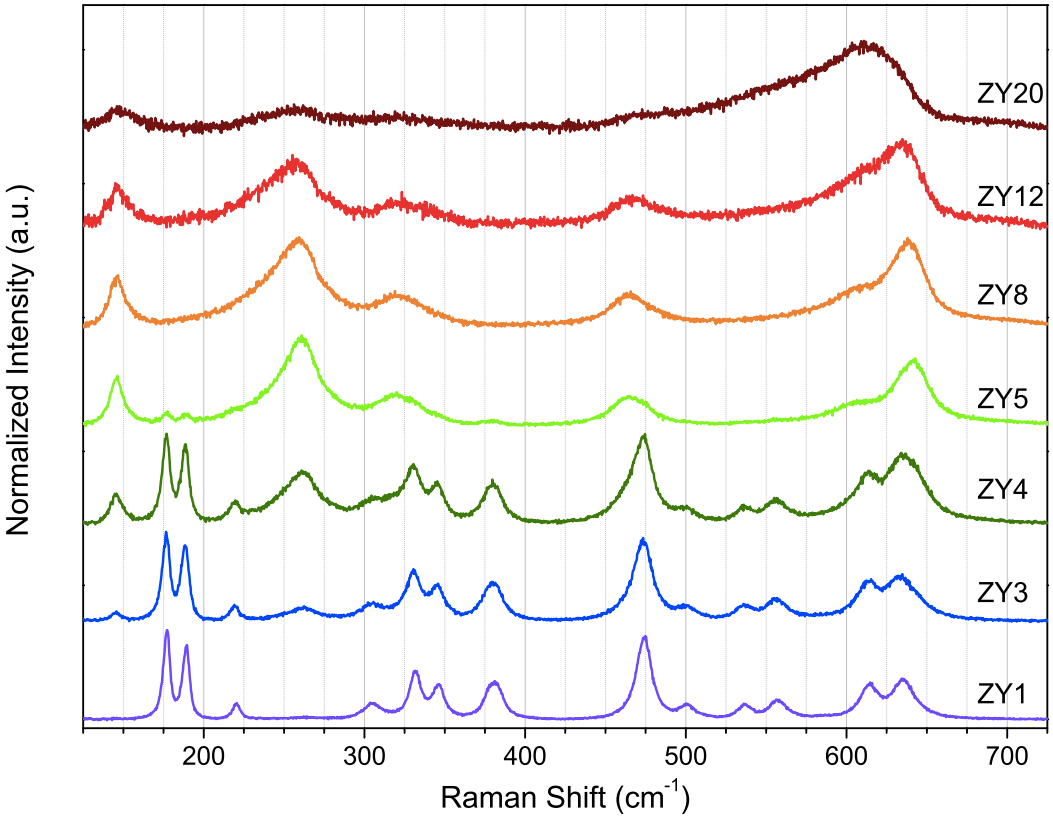

Figure 3.3: Raman spectra of ZY series.

Cathodoluminescence (CL)

As reported above in Subsection 1.2.2 on page 7, zirconia engineering properties are correlated to the oxygen vacancies, which is also the main cause of ceramic failure. The comprehension of the oxygen sublattice structure has a central key to solve this technological problems. In this case, strong influence on the physical properties seems to be given by the anion order, particularly when they are sensitive to distortions and the local disorder. Cathodoluminescence (CL) spectroscopy could be a potential technique to explain many issues [117, 118].

The zirconia CL spectra are very complicate, also for their interpretation. The CL emission from the Yttria Stabilized Zirconia (YSZ) lattice is composed of a main

broad band, which is the sum of several emissions from oxygen-related defects with different sublattice. The global band, peaked around 500 nm, could be explain as the sum of three partially overlapped bands centered at 460 nm (2.69 eV), 550 nm (2.25 eV) and 600 nm (2.07 eV). The first, known also as F^+ center, is correlated to a singly occupied vacancy and involving an intrinsic defect site, in which Zr^{4+} cations are nearest neighbors to the vacancy. The other two are usually referred to F_A^+ and F_{AA}^+ centers, depending if one or two Y^{3+} cations are nearest neighbors to the vacancy, respectively [33, 119–122]. These are extrinsic centers, because are correlated to the presence of the doping cation. Schematic representations of the oxygen vacancy sites have been proposed in Figure 3.4 [123].

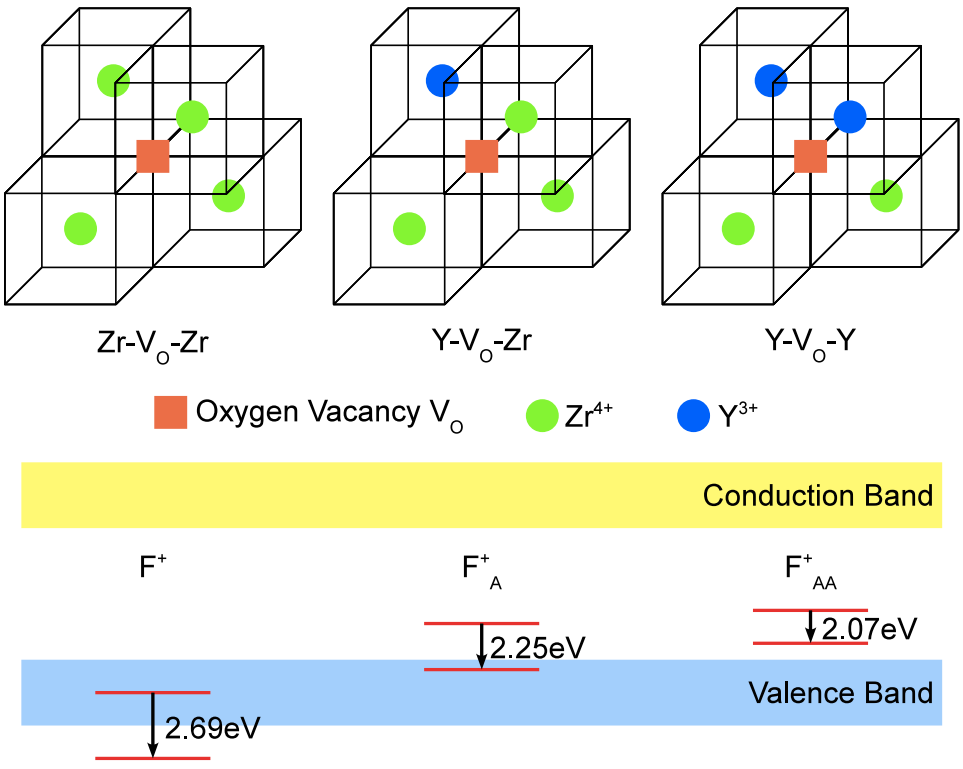

Figure 3.4: Schemes of the different vacancy sites in Y-doped zirconia and relative energies.

In order to study the global signal, knowledge of CL behavior for the single phases is necessary. Thanks to the already reported XRPD and Raman analyses, a correct evaluation about the CL bands could be done. In Figure 3.5 the CL spectra used as references for the signal analyses have been reported.

The overall CL bands with a deconvolution method have been studied, according to the previous literature [124–126]. A set of six Gaussian functions with fixed

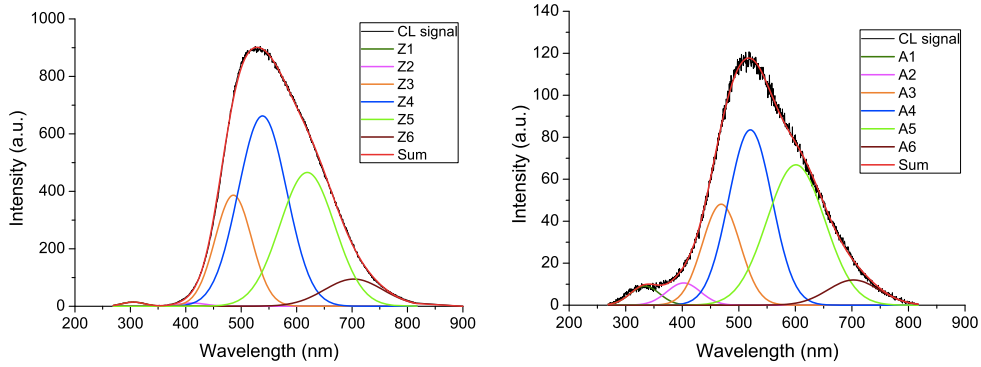

a. Undoped Monoclinic **b.** Monoclinic (ZY1)

c. Tetragonal (ZY8) **d.** Cubic (ZY20)

Figure 3.5: CL spectra of undoped zirconia, monoclinic, tetragonal and cubic samples and their relative fitting sub-bands.

positions and Full Width Half Maximum (FWHM) has been considered. This procedure has been performed only for the Y-doped samples, in order to give a rational description of the spectra morphology variation. In Figure 3.5a the CL signal of undoped zirconia sample has been reported. Although all the recorded spectra look similar, thanks to the fitting procedure some fundamental differences in their morphology could be recognize. The undoped sample has a quite strong emission, which is generated from metastable energy levels, related to the different type of intrinsic oxygen vacancies, present within the zirconia band gap [127]. Another important consideration could be done about the hafnia (HfO_2) impurities naturally present in the zirconia precursor. The presence of Hf^{4+}, which is quite common also in highly pure undoped zirconia, generates a luminescence emission around 1.7 eV [128, 129]. So, the weaker band (A6 and Z6) around 700 nm has been correlated to the oxygen vacancy emission in hafnia. Similarly, the reported band around 400 nm (Z2 and A2) could be arise from another impurity atoms, as carbon contamination present in the SEM chamber or due to synthesis byproducts.

Taking in account that the irradiation energy of the beam (5 kV) overcomes the zirconia band-gap, an excitation from the valence band to the conduction band has been achieved, and the electron-hole recombination process, which involves one or two electrons, could be possible. These infra band states, from 1.7 to 3 eV, cause the luminescence emissions. Commonly two electrons occupy the same trap, but even if one electron is removed, the other could remain strongly localized. The positive-charged defect traps one electron, forming a F^0 center, which has an emission between 430 and 460 nm [130, 131]. The main contribute in the undoped sample, according to fitting method, has been at 485 nm, that has been ascribed to the intra-defect transition F^+ center. The peak shift respect to literature could be related to a size-related effect [132]. The two main bands (Z4 and Z5) have been attributed to F centers in a different site, caused by a lattice distortions introduced by the vacancy, as suggest by Smits et al. [133].

Considering that the spectra intensity should be directly correlated to the vacancies sites, an increment of intensity should be expected together with the yttrium content. As reported in Figure 3.6, the intensity of the CL spectra decreases progressively increasing the doping percentage, underlining a sort of concentration quenching effect of the Y^{3+}.

Table 3.2: Gaussian sub-bands data set for principal ZY samples and undoped zirconia. In brackets the undoped zirconia data are reported.

Sub-band	Position (nm)	FWHM (nm)	Relative area weight (%)				
			ZrO_2	ZY1	ZY5	ZY8	ZY12
(Z1) A1	(305) 334	(47) 61	(0.4)	2.5	3.4	0.4	0.5
(Z2) A2	(410) 402	(61) 70	(0.4)	3.3	7.5	7.7	8.8
(Z3) A3	(485) 469	(78) 79	(18.2)	17.2	18.4	25	27
(Z4) A4	(538) 520	(103) 90	(41.3)	34.3	28.6	28.9	29
(Z5) A5	(619) 601	(116) 120	(32.7)	36.6	34	30.7	28.6
(Z6) A6	(703) 703	(124) 107	(7)	5.8	7.8	7	5.8

After these considerations, the CL emission intensity should be correlated to the oxygen vacancies, supposing that it is the result of an oxygen-deficient sublattice intra-band-gap activity. Regarding the data reported in Table 3.2 it is worth noting that the radiative centers of the undoped and the ZY series seem to be the same. For the doped zirconia samples the relevant sub-bands (A4 and A5) are related to the different color centers, while the new F center substitutes the intrinsic center of the undoped case, with also a different energy. The new energy is generally due to the increased mobility of the double ionized oxygen vacancy (with a formal charge +2). The migration towards the 3-fold coordinated yttrium site is allowed, thanks to its virtual negative charge compared to the 4-fold coordinated zirconium site. When the Y^{3+}–V_O is formed, in order to conserve the electrical neutrality, only

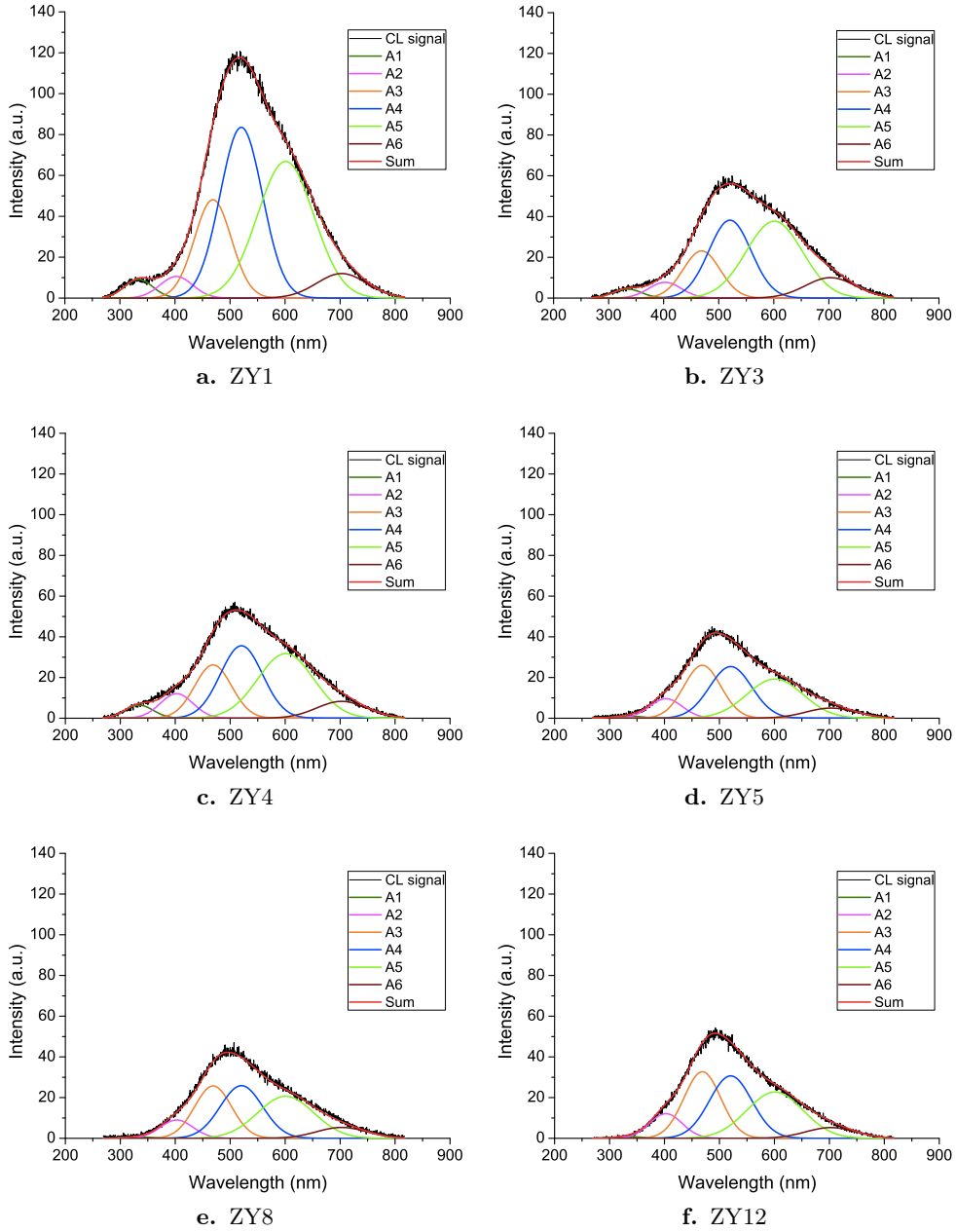

a. ZY1 **b.** ZY3

c. ZY4 **d.** ZY5

e. ZY8 **f.** ZY12

Figure 3.6: CL spectra and their relative fitting collected for the ZY series samples.

one electron could be trapped into the vacancy instead of two, as in the undoped zirconia. A two-step recombination is necessary, which is also less efficient and causes the intensity reduction together with the Y^{3+} concentration increment. Finally, the A1 sub-band seems to be relevant only in the doped sample with monoclinic phase. In the undoped and the poor-monoclinic samples, this band is weaker than in the other samples. Probably, it could be raised from a vacancy, which involves the Y^{3+} and when the band gap of the monoclinic, lower than the tetragonal one, allows it

[134, 135].

A quantitative analysis of the zirconia phase has finally been made thanks to the CL spectrum intensity. As already mentioned, higher is the dopant content lower is the spectrum intensity. In this type of analysis the area ratio of the main sub-bands A4 and A3 (R =A4/A3) has been taken into account. In Figure 3.7, the R ratio plots against the Y^{3+} content and the monoclinic fraction have been reported.

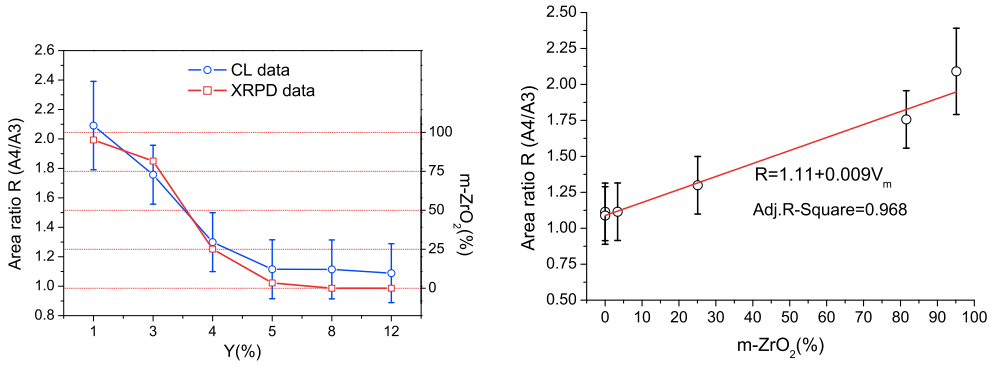

a. Confrontation between CL and XRD data **b.** Correlation between CL and XRD data

Figure 3.7: Dependence of CL sub-bands A4/A3 ratio with the monoclinic volume fraction.

Regarding the Figure 3.7a, a good agreement between the monoclinic volume fraction (V_m) and the ratio R path is visible. A linear relation has been presented between the experimental data, which has been reported in Figure 3.7b. The mean value of the ratio R as average of 20 spectra has been considered. The linear equation has been reported in the plot.

A strong dependence of the vacancies from the zirconia phase have been evidenced, even if the CL differences among the tetragonal samples it is not suddenly explainable. About this, the ratio R follows very well the phase content into the ZY samples. This could be explained considering the luminescence quenching effect as consequence of a non-radiative and competitive recombination mechanism. As suggest elsewhere, the oxygen vacancy coordinated with a Y^{3+} could be a hole trap [136, 137]. However, this cannot explain neither the intensity reduction nor the F_{AA} centers increment. It seems reasonable that the presence of Y^{3+} itself caused the failing of the CL intensity. Since the intrinsic vacancies are the most efficient (undoped zirconia), in the doped samples they move to less efficient site (*delocalization effect*). In this way, the new vacancy population correlated to the Y^{3+} content failed the compensation for the loss of CL emission due to the intrinsic vacancies annihilation. The overall intensity is dominated by this annihilation rather than by the formation of the vacancy sites related to Y^{3+}.

3.2 Zirconia Europium-doped and co-doped powders

3.2.1 Trivalent cations doped systems

An appealing property of the lanthanide cations is the marked dependence of their luminescence by the occupied crystal site. More symmetrical is the site and less allowed are their characteristic *f-f* transitions. As already mentioned (see Subsection 1.2.1 on page 4), in the monoclinic phase, there is a sevenfold coordinated cation site, whereas in the tetragonal phase has a cubic coordination (coordination number 8). Considering europium as substitutional impurity, it occupies a symmetrically different environment into the two phases. Furthermore, the different crystal field causes a shift of the hypersensitive $^5D_0 \rightarrow ^7F_2$ transition, as reported below [138]. The purpose of the powders samples prepared (ZE and ZYE series), has been the exploitation of this particular behavior in order to monitor the degradation degree of the stabilized zirconia material, starting from some previous observations [3, 4]. The stabilization of the tetragonal phase by adding europium, or both europium and yttrium, has been obtained. Then the $t \rightarrow m$ transformation by mechanical pressure has been induced progressively. The nominal content of trivalent doping cations in both cases is 4 mol% with respect to zirconium (see Subsection 2.1.2 on page 19). The phases relative content with XRPD and Photoluminescence (PL) analyses has been monitored parallel.

X-ray Powders Diffractometry (XRPD)

Observing the single-phase patterns proposed in Figure 3.8, it is evident as the $1\bar{1}1$ (at 28°) and 111 (at 31°) peaks of the monoclinic and the 111 (at 30°) peak of the tetragonal are the more intense and characteristics in order to compare the phase content. From Figure 3.9, it is noticeable how the $t \rightarrow m$ transition is easily induced by applying quite weak pressure. Really, the ZYE samples shown better stability than the corresponding ZE sample. Actually, yttrium is more suitable, and cheaper, than europium to achieve tetragonal stabilization. In Table 3.3, the percentage of tetragonal phase quantified from the Rietveld refinements have been reported (error estimation is around 2%). Some reflections arising from the monoclinic phase around 31.5°, 35°, and 50° are unusually intense, because of the positions of the oxygen atoms. These are displaced along the b and c axes and the March-Dollase preferential orientation parameter for the [111] direction have been refined [139]. This allowed reducing the mismatch between the observed and calculated diffraction patterns. The preferred orientation is caused by the application of a highly oriented pressure, especially for samples ZE2, ZE3, ZE4 and ZYE2, ZYE3, ZYE4. In the ball-milled samples the patterns resumed their usual profile (ZE5 and ZYE5).

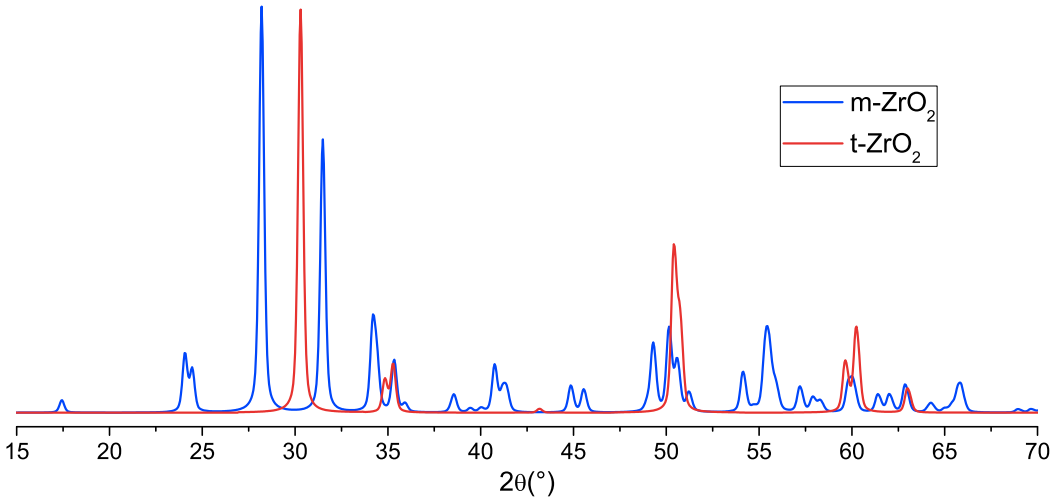

Figure 3.8: XRPD patterns of the pure monoclinic and tetragonal phase of zirconia.

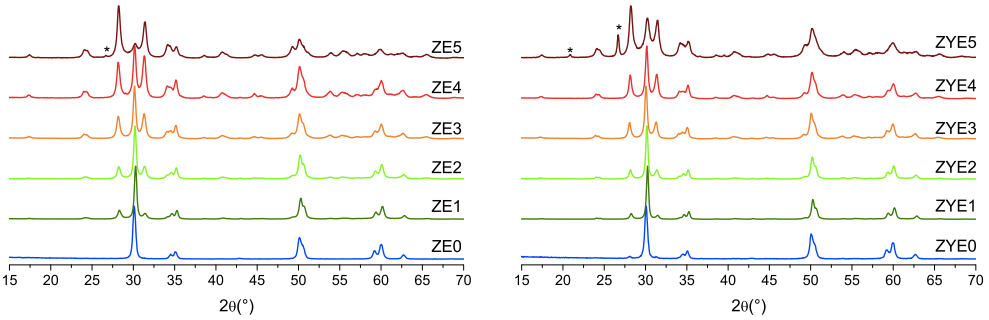

a. ZE series **b.** ZYE series

Figure 3.9: XRPD patterns of the ZE and ZYE series. The $*$-marked peaks are related to silica impurities from the ball milling jar.

The $t \rightarrow m$ transformation takes place first in those grains where the dopant content is lower. This has been underlined by the refinement of the lattice parameters. The europium quantity in tetragonal phase, could be determined by the formula

$$\mathrm{Eu}(\%) = \frac{2V_{cell} - 133.85}{0.223} \tag{3.1}$$

where 133.85 is the undoped tetragonal zirconia cell volume and 0.223 is a slope of the linear fitting for the cell volume versus europium content plot [5]. In Table 3.4, the content of europium in the tetragonal phase for the ZE series increases with the content of the monoclinic phase, as also visible in Figure 3.10 for the Rietveld refinements data. This is a signal that the tetragonal fraction poorer in europium undergoes the transformation first.

Table 3.3: Volume fractions of tetragonal phases for the ZE and ZYE series, as obtained by the Rietveld refinements.

Processing	Sample	t-ZrO_2 (%)	Sample	t-ZrO_2 (%)
As obtained	ZE0	100	ZYE0	95.5
After mild mortar ground	ZE1	68.7	ZYE1	77.5
After 3 GPa applied compression	ZE2	59.1	ZYE2	66.6
After 6 GPa applied compression	ZE3	43.3	ZYE3	54.6
After 9 GPa applied compression	ZE4	35.8	ZYE4	47.3
After ball milling	ZE5	22.8	ZYE5	36.1

Table 3.4: Cell volume variation for tetragonal phase, and the resulting Eu content for the ZE series.

Sample	V_{cell} (%)	Eu (%)
ZE0	67.353	3.84
ZE1	67.376	4.05
ZE2	67.381	4.09
ZE3	67.396	4.22
ZE4	67.404	4.30
ZE5	67.450	4.71

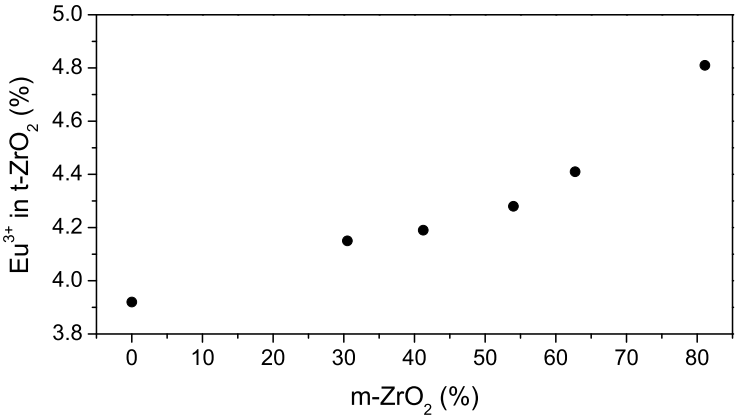

Figure 3.10: Europium content in tetragonal phase as calculated from the Rietveld refinements versus monoclinic content in the ZE series.

Photoluminescence (PL)

In order to investigate the luminescent behavior of the Eu-doped tetragonal stabilized zirconia, Photoluminescence (PL) and Photoluminescence Excitation (PLE) spectra have been recorded. In Figure 3.11 the ZE2 PL and PLE spectra have been reported as example of the typical luminescent properties of the Eu^{3+} into zirconia. The transition $^5D_0 \rightarrow ^7F_2$ is the most interesting for the above-mentioned purpose. Actually, its main component is centered at 606 nm or 613 nm depending on the Eu^{3+} cation is into the tetragonal or monoclinic zirconia, respectively. It is worth

noting that in the PLE spectra no shape difference has been noticed, so only one of them is reported, as example. The PL spectrum has been recorded exciting at 393 nm, which is the most efficient excitation wavelength for the $^5D_0$ level indirect population. From this level all the transition to the lower lying multiplet ^7F_J are present and distinguishable.

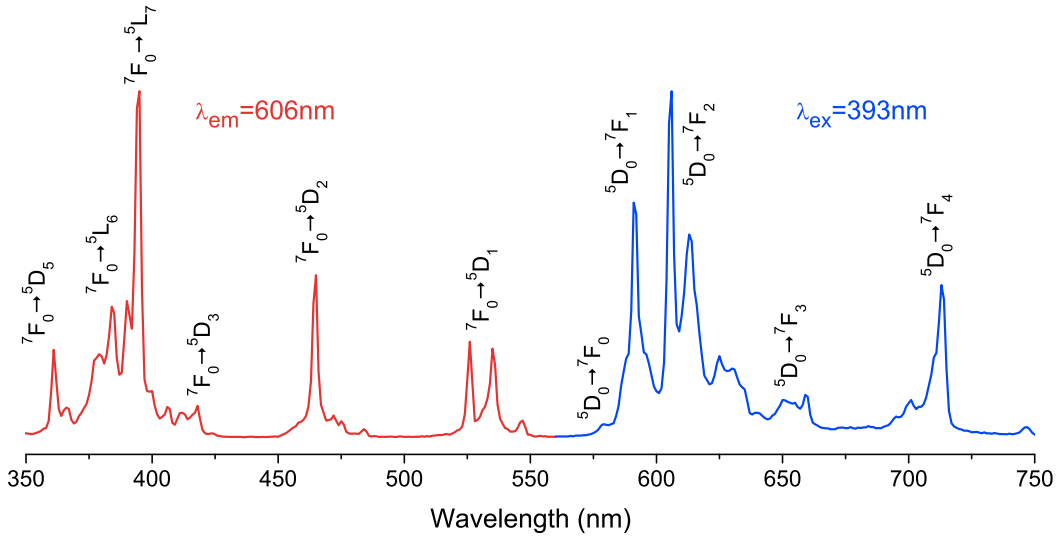

Figure 3.11: Typical PLE (λ_{em} =606 nm, red spectrum) and PL (λ_{ex} =393 nm, blue spectrum) spectra of Eu^{3+} in mixed tetragonal and monoclinic phase zirconia. The two peaks at 606 nm (tetragonal) and 613 nm (monoclinic) arise from the Electric Dipole transition of Eu^{3+} in zirconia.

All the PL spectra of the two series have been shown in Figure 3.12. Thanks to the normalization to the intensity at 606 nm, the increment of the emission at 613 nm, due to the Eu^{3+} in monoclinic phase, is evident. Supposing the europium as a substitutional impurity with respect to Zr, a coordination site changing happens from eightfold coordination in tetragonal to less ordered sevenfold in monoclinic [140–142].

It is known that Eu^{3+} has two principal transitions, the Magnetic Dipole (MD) transition ($^5D_0 \rightarrow ^7F_1$) which is environment insensitive, and the Electric Dipole (ED) transition ($^5D_0 \rightarrow ^7F_2$) which is hypersensitive to the chemical surroundings. The latter is more allowed, *i.e.* more intense, when the coordination polyhedron is less symmetrical. Qualitative information about the monoclinic phase has been possible just making the ratio between the integrated intensities of these two transitions. In Figure 3.13, the PL spectra of pure monoclinic and pure tetragonal Eu-doped zirconia have been reported in order to have the two separated references spectra. A pure monoclinic Eu-doped zirconia (ZEM) with very low content of dopant (0.05%) has been produced for this aim. Even if there is a small overlapping between them,

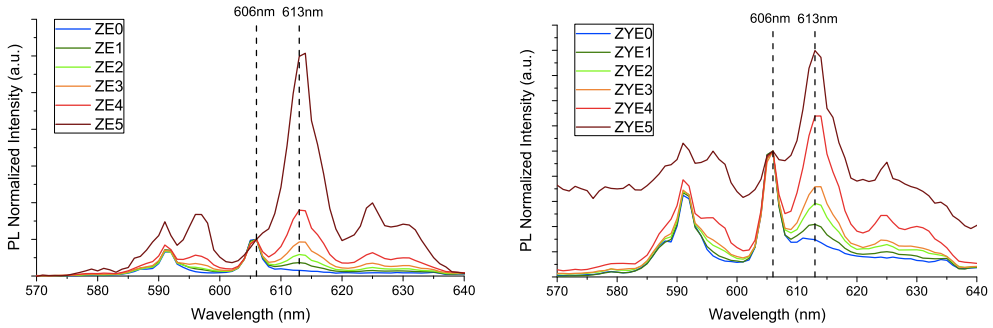

a. ZE series **b.** ZYE series

Figure 3.12: Comparison of the PL spectra of the samples of the series ZE and ZYE, excited at 393 nm.

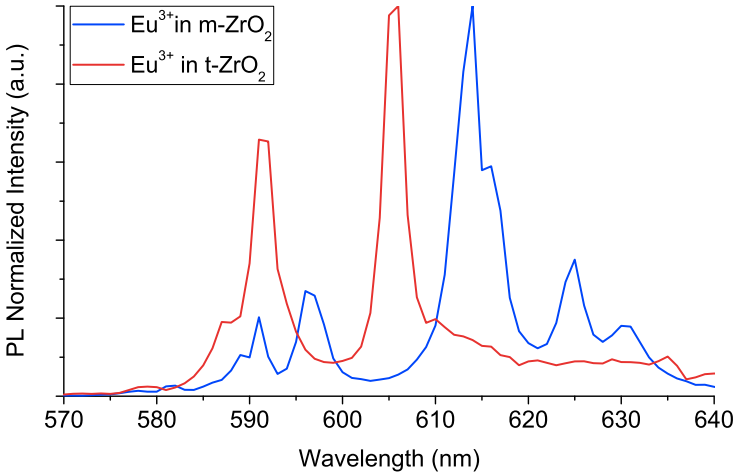

Figure 3.13: Comparison between the PL spectra of Eu^{3+} (λ_{ex} =393 nm) in pure tetragonal (ZE0, 4mol% Eu) and in pure monoclinic (ZEM, 0.05mol% Eu) zirconia. The spectra have been normalized for a better comparison.

the ranges 570-600 nm and 600-640 nm for the MD and ED transitions have been considered, respectively. The ratio $I_{600-640}/I_{570-600}$ is usually referred as R-value.

The calculated values of R, listed in Table 3.5, has a trend in accordance with the expected values, except for the sample ZYE5. This unexpected result can be interpreted by looking at the PL spectra in Figure 3.14, where a broad emission centered around 480 nm influenced the Eu^{3+} emission. In literature, this emission is correlated to the monoclinic phase, where the oxygen vacancies are less [143]. This background determines an increase of the integrated emission intensity, in particular the overlap is prominent in the monoclinic range (570-600 nm), leading to an underestimation of R.

A quantitative analysis has been performed, taking advantage of the pure Eu-doped phases spectra reported in Figure 3.13. Thanks to a linear combination of

Table 3.5: R values for ZE and ZYE series.

Sample	R	Sample	R
ZE0	1.78	ZYE0	1.96
ZE1	1.89	ZYE1	2.17
ZE2	2.41	ZYE2	2.23
ZE3	2.65	ZYE3	2.32
ZE4	3.17	ZYE4	2.53
ZE5	3.90	ZYE5	1.44
ZEM	4.30	-	-

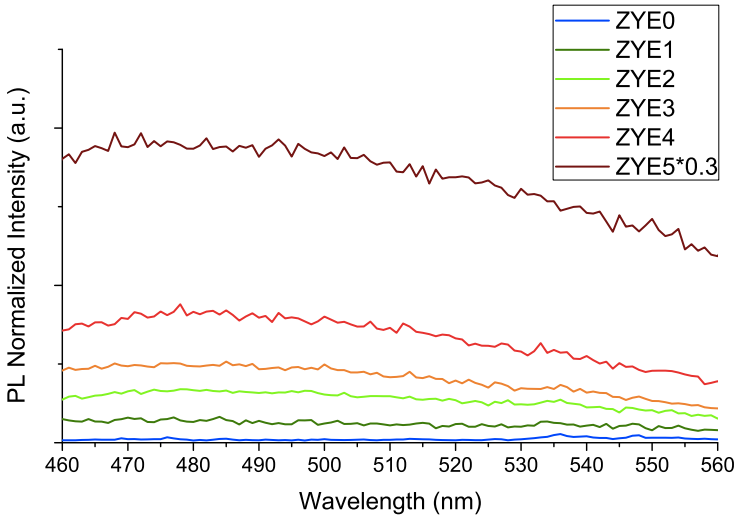

Figure 3.14: Increasing intrinsic luminescence of the zirconia matrix. The PL spectra (λ_{ex} =393 nm) have been normalized to the 590 nm intensity. The ZYE5 spectrum has been reduced by a factor of 3.

the reference spectra, the experimental data of the mixed phases samples have been fitted, considering a least-square procedure starting from the assumption

$$\sum_i (y_{i,\text{obs}} - y_i)^2 = \sum_i [y_{i,\text{obs}} - (aM_i + bT_i)]^2 = S \tag{3.2}$$

where y_{obs}, M, and T are the observed intensities of the sample with mixed phases, pure monoclinic (ZEM) and pure tetragonal (ZE0) phases, respectively for the i-th wavelength; whereas a and b are the coefficient of the linear combination. By imposing

$$\frac{\partial S}{\partial a} = 0 \quad \text{and} \quad \frac{\partial S}{\partial b} = 0 \tag{3.3}$$

a homogeneous system has been achieved which could be arranged to obtain

$$\begin{pmatrix} \sum_i T_i^2 & \sum_i M_i T_i \\ \sum_i M_i T_i & \sum_i M_i^2 \end{pmatrix} \begin{pmatrix} a \\ b \end{pmatrix} = \begin{pmatrix} \sum_i T_i y_{i,\mathrm{obs}} \\ \sum_i M_i y_{i,\mathrm{obs}} \end{pmatrix} \tag{3.4}$$

$$\begin{pmatrix} a \\ b \end{pmatrix} = \begin{pmatrix} \sum_i T_i^2 & \sum_i M_i T_i \\ \sum_i M_i T_i & \sum_i M_i^2 \end{pmatrix}^{-1} \begin{pmatrix} \sum_i T_i y_{i,\mathrm{obs}} \\ \sum_i M_i y_{i,\mathrm{obs}} \end{pmatrix} \tag{3.5}$$

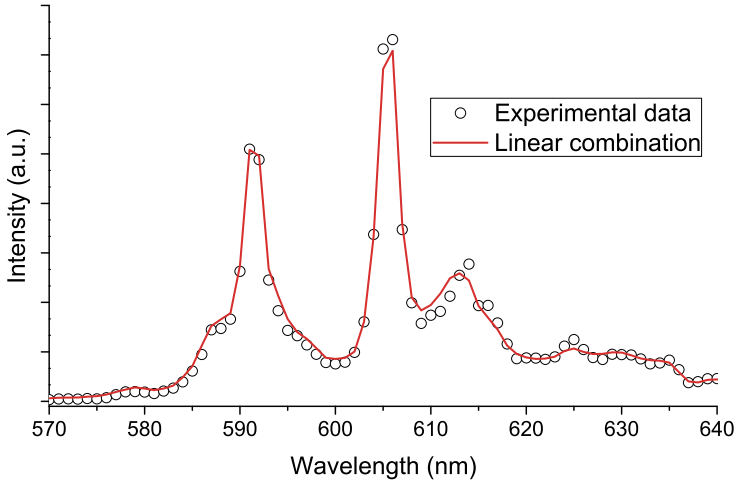

Figure 3.15: Fit of the ZE1 spectrum obtained using the experimental spectra of the pure monoclinic and tetragonal phases.

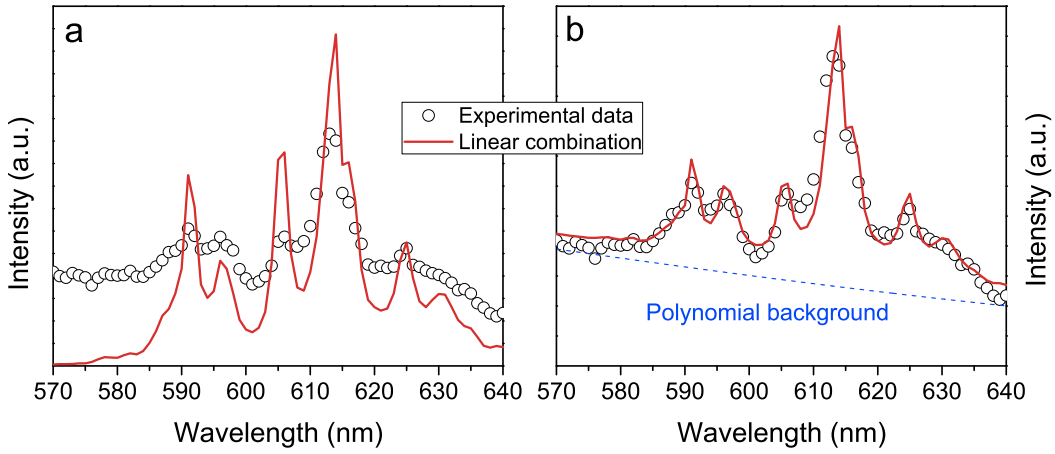

Figure 3.16: Fit of the ZYE5 spectrum obtained using only the experimental spectra of the monoclinic and tetragonal phases (a) or adding a third-order polynomial background contribution (b).

From equation (3.5) a quantitative compositional information about the sample by the simple ratio $a/(a+b)$ has been deduced. A good correspondence between the fit and the experimental data for the ZE series has been obtained, as reported

in Figure 3.15. For the ZYE samples a discrepancy, due to the aforementioned emission (centered at 480 nm), which has not been taken into account in the fitting procedure, has been observed. In order to improve the results a fit of the background with a third-order polynomial has been considered. In this way a 6×6 matrix has been obtained with evident improvement of the fit, as visible comparing the two fits reported in Figure 3.16.

Data correlation

The above reported results obtained from the PL analyses have been compared to the Rietveld refinements made on the XRPD patterns. In Figure 3.17 the monoclinic content obtained with the two procedures have been reported. A good agreement between the data is clearly visible, the points follow quite well the linear correlation $y = x$. Certain variability could be imputable to the aforementioned difficulties have been met during the development of the fitting. For example, the use of reference PL spectra of Eu single-doped samples also for the fit of ZYE series, introduced a systematic overestimation of the monoclinic phase in that series (Figure 3.17b). Disregarding this systematic error, the fit can still give useful information about the monoclinic phase content.

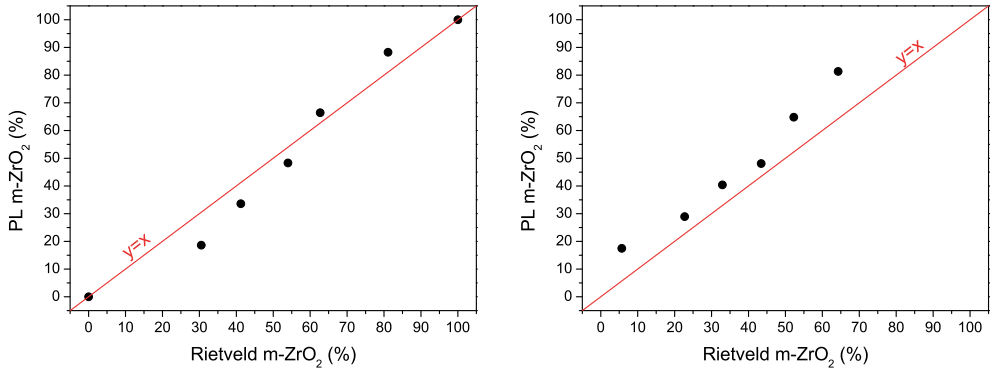

a. ZE series **b.** ZYE series

Figure 3.17: Comparison between the results obtained from the PL analyses and the Rietveld refinements on ZE and ZYE series.

An alternative approach have been counted on the calculation of $^7F_2$ peak integrated area between 600-608 nm and 608-620 nm ranges, and considering the intensity ratio ($I_{608-620}/I_{600-620}$). The new plot, reported in Figure 3.18, gives a linear relation both for ZE and ZYE series. The relation seems valid up to 70% of monoclinic content in the ZYE series, although the presence of the above-mentioned emission does not come from the RE cations. This method allows using a band filter to register the total intensity in the right range of wavelengths without collect-

ing a complete spectrum of a hypothetical ceramic piece, monitoring the presence of monoclinic zirconia, after a previous calibration curve. Furthermore, this method does not need the use of reference spectra, avoiding any error coming from its use.

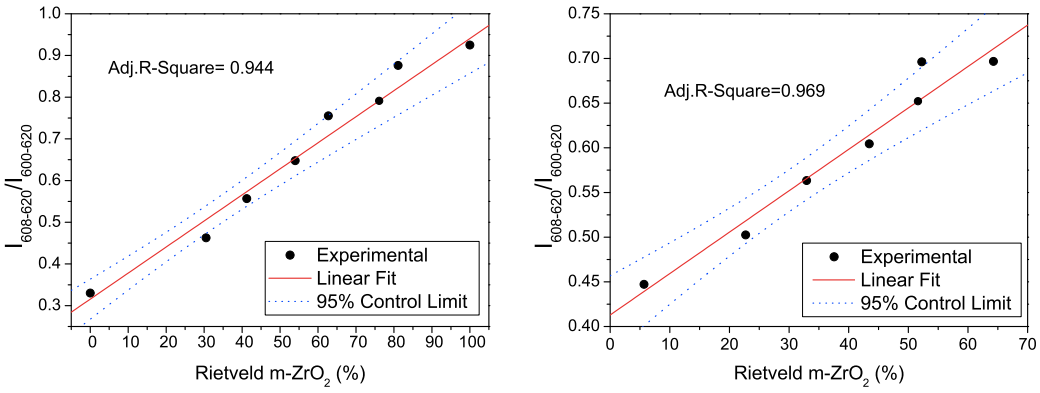

a. ZE series **b.** ZYE series

Figure 3.18: Comparison between the results obtained from the ratio between the integrated areas of the ${}^7F_2$ peaks and the Rietveld refinements on ZE and ZYE series.

3.2.2 Trivalent and pentavalent cations doped system

In order to verify the oxygen vacancies role into the YSZ materials, a co-dopant series of samples, called ZYET, has finally been prepared. The investigated sample ZYE0 (reported here as ZYE) has been considered as starting point for this new series. This sample has a concentration close to the tetragonal stabilization threshold. As reported in Subsection 2.1.2 on page 19 a progressive amount of Ta has been introduced into the (Y, Eu)-doped zirconia, from 1 to 10 mol%. As already mentioned, Ta is a pentavalent cation, so theoretically it has the opposite effect of the trivalent doping cations (Eu^{3+} and Y^{3+}). For each two trivalent cations one oxygen vacancy is introduced for electroneutrality preservation. The subsequent introduction of two pentavalent cations should plug it. While in the previous experience the tetragonal phase has been destabilized by extrinsic factor, such as a compression process, here the main idea has been to achieve the same effect by intrinsic modification, *i.e.* the oxygen vacancies reduction.

The above presented double investigation method should be very useful in order to study the phase stabilization path with the tantalum quantities. In Figure 3.19 the XRPD patterns and the PL spectra of ZYET series have been reported.

From Figure 3.19, it is evident as the tetragonal phase, which has been stabilized by trivalent doping in the starting sample (ZYE), is reduced progressively by the Ta increment. This behavior is clearly visible in the XRPD patterns where, the principal

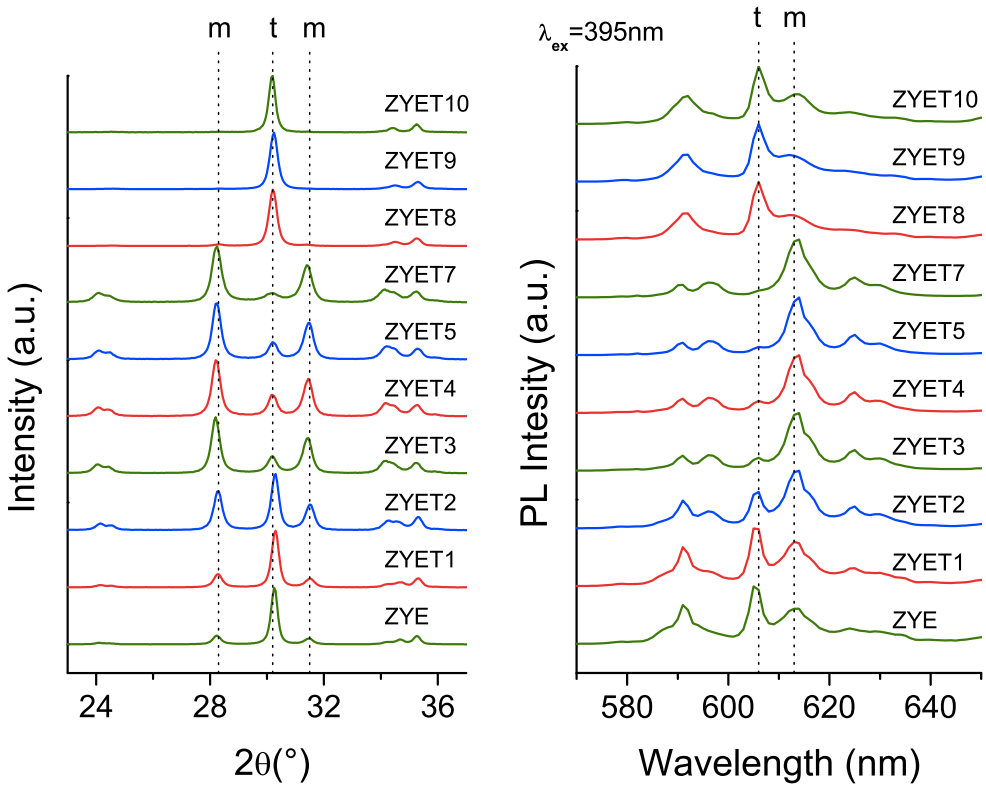

a. XRPD patterns **b.** PL spectra

Figure 3.19: XRPD patterns and PL spectra of ZYET series.

peak of tetragonal phase, around 30°, diminishes until 7 mol% of Ta. Parallel the lateral peaks (at around 28° and 32°) of the monoclinic zirconia increase. The same trend is clearly observed in the PL spectra until the 7 mol% of Ta, as expected from the previous study. Table 3.6 reports the quantitative data from Rietveld refinements. It is worth noting that even if the monoclinic phase seems to disappear from the XRPD patterns, a little amount has still been present in all the prepared samples, as reported in Table 3.6. Also in the PL spectra the monoclinic emission is clearly present in the last three samples of the series.

Some interesting consideration could be made on these analyses. As reported above, the stabilization of the more symmetrical tetragonal and cubic phases has been demonstrated to be a direct consequence of the introduction of oxygen vacancies, due to the charge compensation phenomenon, when sub-tetravalent cations is introduced in the lattice. In order to study the effect of the substitutional defects and oxygen vacancies separately, some research groups managed to co-doped zirconia with tri- and penta-valent cations simultaneously. The pentavalent cations have a vacancy annihilating effect, and it is demonstrated that the presence of equimolar quantities of them (*e.g.* Y-Ta or Y-Nb couples) leads to the absence of oxygen va-

Table 3.6: Volume fractions of tetragonal phases for the ZYET series, as obtained by the Rietveld refinements. The ∗-marked assignments are not confirmed.

Sample	t-ZrO_2 (%)
ZYE (ZYE0)	95.5
ZYET1	62.5
ZYET2	38.2
ZYET3	16.8
ZYET4	14.3
ZYET5	13.7
ZYET7	12.9
ZYET8	92.8*
ZYET9	93.4*
ZYET10	94.7*

cancies into the lattice [144]. Nominally, they do not contain any oxygen vacancies because the equal concentration of trivalent (Y) and pentavalent (Ta) cations satisfied the charge neutrality without modifying the oxygen content. This is carry out by the very low ionic conductivity of very similar materials co-doped with Nb (even ifTa) compared to stabilized zirconia, with oxygen vacancies [145]. In the ZYET series, the increment of the tantalum progressively destabilized the tetragonal phase. Differently from the previous study, the production of a less-stabilized tetragonal zirconia by oxygen vacancies reduction has been achieved, while previously the external stresses have been the cause of the tetragonal progressive destabilization.

Some unexpected results must to be, however, underline. Theoretically, the sample ZYET4 has equimolar amount of trivalent and pentavalent cations, so it should be totally monoclinic, but this has not been verified. As reported in Table 3.6, about 14% of tetragonal phase is still present. Even when the Ta content exceeds the trivalent cations nominal amount, the tetragonal phase does not disappeare totally. Furthermore, in the last three samples (ZYET8, ZYET9, ZYET10) the tetragonal phase seems to be the predominant phase. In order to explain this process, it must refer to another mechanism of phase stabilization, or new phase production. In order to understand the tantalum behavior into zirconia, a new study has been started, as reported below.

3.3 Zirconia Tantalum-doped preliminary powders

X-ray Powders Diffractometry (XRPD)

Since the study of the ZT series opened a quite new and less investigated issue on the zirconia materials panorama, it has been necessary to start from a detailed structural analysis. In Figure 3.20 have been reported the XRPD patterns. The samples could be divided in three groups. At the first group belong the samples (ZT1 and ZT3)

richer in the monoclinic phase. The patterns of the second group (ZT4 and ZT5) are very similar and a co-presence of monoclinic and a *not well-defined phase* (label as PN henceforth), usually reported in literature as orthorhombic or tetragonal, is detectable [56, 59, 65–67]. For these samples, the PN is the prevalent phase. In the last group, the three samples (from ZT8 to ZT20) show only the PN phase. In Table 3.7 the quantitative estimation of the monoclinic phase ($P2_1/c$) for the ZT series samples has been summarized.

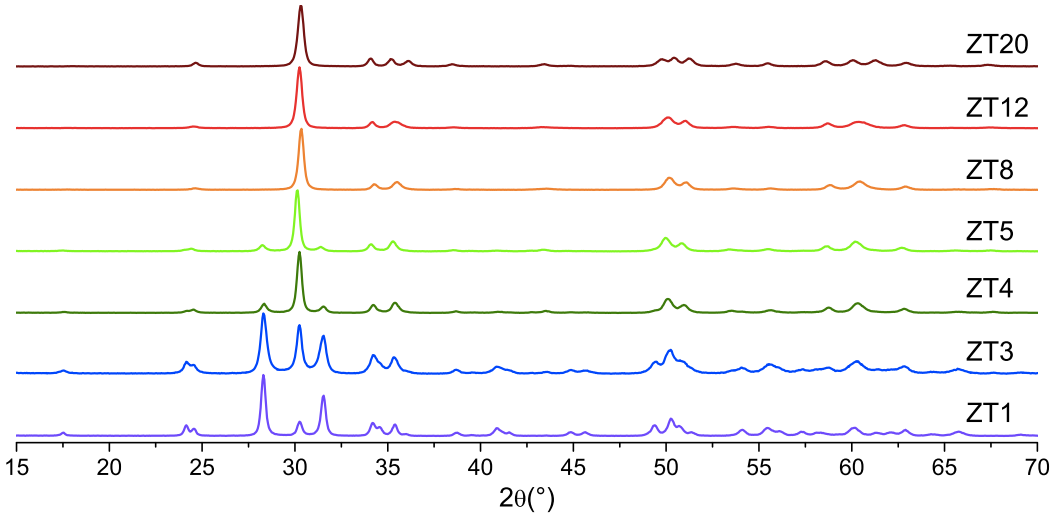

Figure 3.20: XRPD patterns of calcined powders at 1000 °C.

Table 3.7: Volume fractions of monoclinic phase ($P2_1/c$) for the ZT series, as obtained by the Rietveld refinements.

Sample	m-ZrO_2 (%)
ZT1	87.6
ZT3	69.4
ZT4	24.1
ZT5	18.1
ZT8	0
ZT12	0
ZT20	0

In order to study the single PN phase, the XRPD of the ZT12 sample has been analyzed following two approaches. The first approach considered simply the use of the Rietveld refinement, while the second utilized the more complex *direct space* method followed by a Rietveld analysis.

According to the first approach, the Rietveld refinements has been performed on the full-range XRPD patterns ($5° < 2\theta < 140°$) [146, 147]. Monoclinic ($P2_1/c$), tetragonal ($P4_2/nmc$), cubic ($Fm\bar{3}m$) and four known orthorhombic phases ($Pca2_1$,

Pbcm, *Pnam* and *Pbca*) have been chosen as initial structures to be fitted. After a careful evaluation of the different zirconia polymorphs, the orthorhombic $Pca2_1$ (Space Group 29, ICSD[2] 67004, PDF[3] 01-079-1796) phase has been selected as the best result by the Rietveld refinement. The refinement data have been summarized in Table 3.8.

The second approach is started with alternative models incorporating the known phases presented in literature. Tetragonal and monoclinic phases of zirconia together with tantalum and tantalum oxides as Ta_2O_3 and Ta_2O_5 have been explored starting from a multiphase system hypothesis. These preliminary refinements have been made with the Rietveld software Fullprof [148]. All the trials have been unsuccessful, so more as long as a simple insight revealed that the observed diagram has not been corresponded to the usual ones for the crystallographic structure, and it has been demonstrated conclusively that the new product corresponded to a new and unknown structure. Indexation of the diagram by using the X-cell software included in Reflex[4], has been allowed obtaining a monoclinic cell with the space group $C2/c$. Note that this group of symmetry is a maximal subgroup of the $P4_2/nmc$ group of the tetragonal zirconia (see below). Lattice parameters and space group have been validated by means of a Pawley refinement, where peak intensities have been treated as independent variables [149].

Then the resolution of the new structure on the basis of the so-called direct space methods has been performed, since a single crystal pattern has not been available [150–152]. The direct space methods are an alternative to the *reciprocal space* methods. The reciprocal space methods involve approaches developed for single crystal data and optimized for powder data. The direct space methods, instead, use different algorithms for the research of the structural parameters, and an agreement factor between the observed and calculated powder data is evaluated, optimizing the structural model to improve the data matching. A structural model has been optimized monitoring the agreement factor (*e.g.* R_{wp} value[5]) between the observed and the calculated powder diffraction data. Global and profile variables for the calculated diagram have been taken from the previous Pawley refinements. For the optimization, different algorithms of research have been available, mainly Monte-

[2]Inorganic Crystal Structure Database.

[3]Powder Diffraction File.

[4]Reflex and ReflexPlus are tools of the Materials Studio® program and are products of Accelrys Inc., 9685 Scranton Road, San Diego, CA-92121-3752 USA.

[5]Also known as the *weighted profile R-factor*, it is the simplest discrepancy index

$$R_{wp} = \sqrt{\frac{\sum_i w_i (y_{i,\mathrm{obs}} - y_{i,\mathrm{calc}})^2}{\sum_i w_i y_{i,\mathrm{obs}}^2}} \tag{3.6}$$

where w_i is the weight factor $(1/\sigma(y_{i,\mathrm{obs}})^2)$, $y_{i,\mathrm{obs}}$ is the observed intensity and $y_{i,\mathrm{calc}}$ is the calculated intensity.

Carlo methods in its *simulated annealing* and *parallel tempering*[6] variants [150, 151].

First, the optimization of an isolated zirconia molecule, by means of a semi-empirical approach with a NDDO Hamiltonian coupled to the PM6 forcefield, has been made [152]. The PM6 forcefield allows for the parameterization of 70 elements, including Zr and Ta. A Zr−O bond length of 1.8127 Å and a heat of formation of −84.1 kcal/mol have been determined. Then the asymmetric unit composition of the unknown structure has been adjusted considering the 12mol% Ta, *i.e.* $Zr_{0.88}Ta_{0.12}O_2$. The starting model has been built taking in account a material density of $6.40\,g\,cm^{-3}$ and a cell volume of $135.29\,Å^3$ estimating a four structural units per unit cell ($Z = 4$). The number of general positions of the space group is eight ($8f$ Wyckoff position). Therefore, the oxygen atoms have been placed in general positions while Zr, and Ta as substitutional cation, has been placed in a special Wyckoff position with multiplicity 4 (from $4a$ to $4e$). Since the correct cation position was unknown, the next procedure has been followed: the structural unit to a general position in the cell has been thrown, adjusting the occupancy of metal atoms to 0.5 in order to fit the correct density of the material. Also the close-contact penalty condition has been removed in order to enable that the $Zr_{0.88}Ta_{0.12}$ peer atoms converged into their correct special positions during the Monte-Carlo cycles. The module PowderSolve [153], available within Accelrys Reflex Plus product, has been used and five simulated annealing cycles have been performed ($2 \cdot 10^6$ steps). Indeed, the metal atoms converged in pairs towards the $4e$ Wyckoff positions while a preliminary result with an agreement factor $R_{wp} = 11.17\%$ has been obtained. A new attempt has been made with the composition constraint ($Zr_{0.88}Ta_{0.12}$) in the correct $4e$ position. After five new cycles in the same conditions as before, a hopeful agreement factor $R_{wp} = 5.85\%$ has been obtained. As long as the data for the new structure corresponds to powder data, a final refinement has been performed by the Rietveld method with the utility present in ReflexPlus tool. The plot output for the final Rietveld refinements has been shown in Figure 3.21, while the data have been summarized in Table 3.8

In order to support that Ta promotes the conversion from the tetragonal phase ($P4_2/nmc$) to the simulated monoclinic ($C2/c$) versus the usual $P2_1/c$ structure, an *ab initio* calculus for the Transition State (TS) search has been performed. The DMol software package included in Materials Studio®, which applies Density Functional Theory (DFT), has been used [154]. The TS search and optimization have been based on delocalized internal coordinates for either molecular or periodic systems [155]. Primitive cells have been chosen for both the tetragonal phase (reactant)

[6] A simulation method that improves the dynamic properties of Monte Carlo method for physical systems simulations.

Table 3.8: Comparison between the Rietveld refinement parameters achieved with the two different approaches.

	First approach	Second approach
Space Group (SG)	$Pca2_1$ (29, orthorhombic)	$C2/c$ (15, monoclinic)
R_{wp} (%)	6.46	5.34
Lattice parameters	a =5.262(4) Å b =5.023(4) Å c =5.097(4) Å	a =5.035(2) Å b =5.273(2) Å c =5.107(2) Å β = 90.05(2)°
Atomic positions [Wyckoff positions]	Zr-Ta [4a] 0.5278(1); 0.2572(1); 0.2488(1) O1 [4a] 0.8488(1); 0.0448(1); 0.0912(1) O2 [4a] 0.2377(1); 0.4640(1); 0.0166(1)	Zr-Ta [4e] 0.5 ; 0.279(4); 0.25 O [8f] 0.257(2); 0.428(1); 0.935(1)

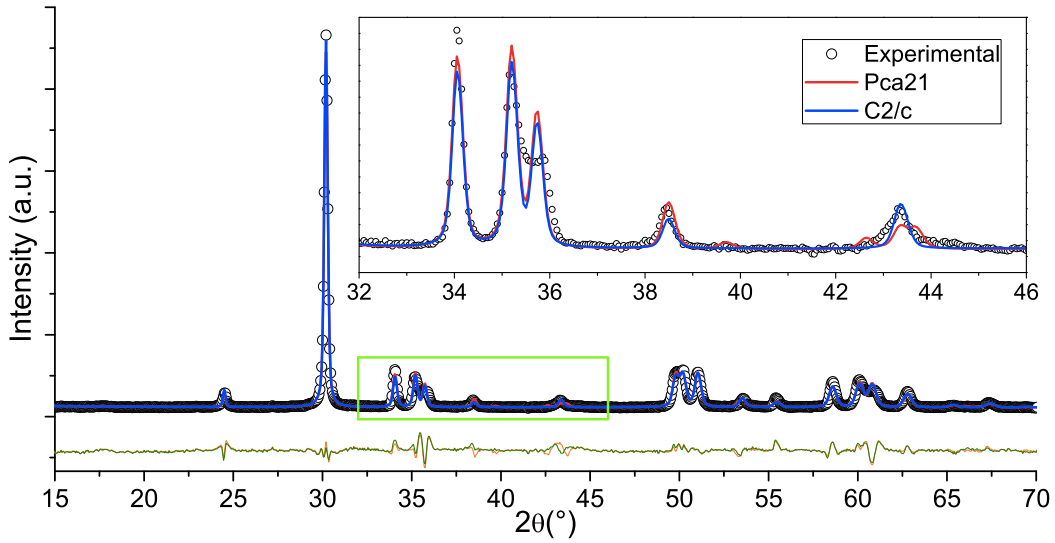

Figure 3.21: Rietveld refinement comparison between $Pca2_1$ and $C2/c$ space groups for ZT12 powder calcined at 1000°C. The residuals are reported below the fitting curves.

and the new monoclinic phase (product). Indeed, the symmetry has been moved to $P1$. The TS search has been relied on the synchronous transit method, which is a global method that interpolates a reaction pathway between reactant and product to find the TS [156]. The TS is a saddle point on the potential energy surface, which indicates the energy barrier connecting reactant and products to each other. After establishing the appropriate pairing of atoms, a full LST/QST cycle[7] has been performed with the GGA functional[8] [156, 157]. An energy barrier of 43.4 kcal/mol has

[7]Linear Synchronous Transitions (LST) and Quadratic Synchronous Transitions (QST).
[8]Generalized Gradient Approximation.

finally been calculated.

As visible in Figure 3.21, the two refinements are quite similar (see also the residuals), the main differences are visible in the inset of the figure suggesting that the proposed solutions cannot be considered conclusive. Therefore, a comparison between the atomic positions inside the cell has also been investigated. In order to compare the two space groups, a different setting for the $Pca2_1$ space group has been chosen. First, the allowed transformation (b, $-a$, c) changes the $Pca2_1$ space group into the $Pbc2_1$ modification, in this way the lattice parameters have been comparable with the $C2/c$ ones. Observing the new generated atomic positions; a translation of (1/4, −3/4, 0) it is necessary for a good match of the two cells. In Figure 3.22 a representation of the two overlapped cells have been proposed.

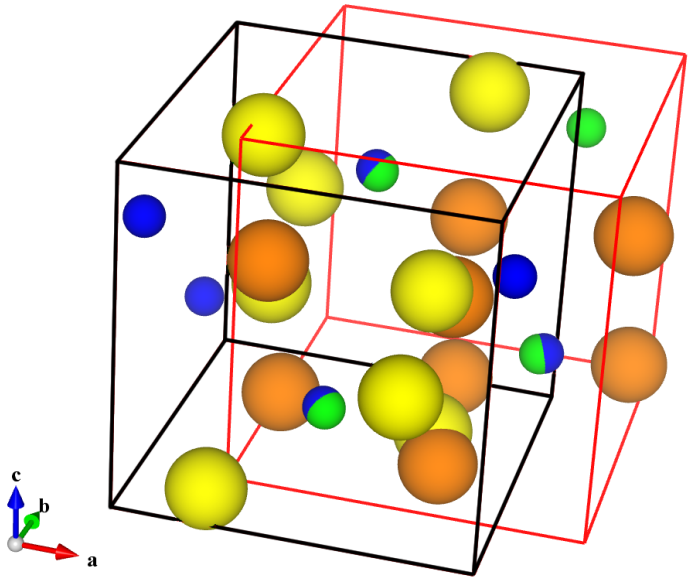

Figure 3.22: Comparison between the monoclinic $C2/c$ (black cell, Zr^{4+}: blue, O^{2-}: yellow) and the orthorhombic $Pbc2_1$ (red cell, Zr^{4+}: green, O^{2-}: orange) cells.

As shown in Figure 3.22, the Zr^{4+} cation sites are completely overlapped (taking in account the structure periodicity), while little shifts of the O^{2-} anions sites are visible. The two structures are quite similar and stackable. It is worth noting that the searched structure is a slight deformation of the fluorite-like structure of the cubic zirconia, which is also the case for the monoclinic $P2_1/c$ polymorph [158] (see Subsection 1.2.1 on page 4). The first neighbors Zr–O distances for the usual monoclinic polymorph are in the range between 2.051 Å and 2.285 Å. However, for the new monoclinic structure ($C2/c$) these distances are shorter (the range is 1.939-2.184 Å), probably due to the presence of Ta as alloying element.

Since the second approach has been much more rigorous and reliable than the

first one, comparing the refinement results, the PN phase as a distorted monoclinic structure with the cell parameters very close to an orthorhombic one ($\beta \approx 90°$) could be considered. This structural feature was probably the main cause of the ambiguous results reported in literature. From the crystallographic point of view, the $Pca2_1$ space group is *acentric* while the $C2/c$ is *centrosymmetric*, so the final decision about the space group identification would be taken only after a single crystal XRD. From a XRPD pattern is not possible to distinguish between these two cells.

As reported by Trolliard, Mercurio, and Perez-Mato, a close relation between tetragonal ($P4_2/nmc$, SG 137), monoclinic ($P2_1/c$, SG 14) and orthorhombic ($Pbc2_1$ or $Pca2_1$, SG 29) zirconia polymorphs exists [159]. All these structures derived from the cubic polymorph ($Fm\bar{3}m$, SG 225), which is a fluorite-type structure. Moreover, the phase transitions are martensitic diffusionless type, it means that they are reversible, and only bond distortions occurs. So, the modifications, from the more symmetric structure to the less one, could be described as Slightly Distorted Fluorite (SDF) or Highly Distorted Fluorite (HDF) sheets inside the different structures. In the above-mentioned work, a good and deep study on atoms displacements and lattice parameters relations among these structures is reported. It is well known that monoclinic is the thermodynamics more stable phase at RT, so the $t \rightarrow m$ transition is spontaneous when the zirconia transforms freely without external stresses. This direct transformation occurs with the axis c_m parallel to the axis c_t, producing a C-type variant crystal, which is the most observable in the zirconia microstructures. Anyway the tetragonal-orthorhombic-monoclinic ($t \rightarrow o \rightarrow m$) indirect path could also occur with a double step process which involves that axis b_m is parallel to the axis c_t (B-type variant crystal). This second indirect process can take place in stressed conditions, as in the bulk of the ceramic pieces. During the martensitic $t \rightarrow m$ transformation, the correlated volume increment (4%) leads to high stress regions, where the same transition could be avoided. So, a high-pressure orthorhombic phase could be intrinsically stabilized and later transit to monoclinic phase. In this way, both the paths occur in the same region at the same time, producing B and C-type variant crystals. The authors concluded that monoclinic and orthorhombic polymorphs are equally accessible if they are regarded as cubic phase distortion, but once the tetragonal configuration occurred (three equivalent orientations respect to the cubic setting are possible) the symmetry between them is broken and a reconstructive transition should be necessary to pass from orthorhombic to monoclinic. Moreover, it is worth noting that both monoclinic and orthorhombic needed at least two distortion modes. Furthermore, both the phases could be achieved by the contemporary presence of two distortions of the same space groups ($Pcca$ and $Pbcn$), even if with different relative orientation. Finally, the authors suggested that the orthorhombic phase is an alternative structure to the monoclinic phase rather than

an intermediate step of the martensitic transformation. As schematically shown in Figure 3.23, the monoclinic $C2/c$ as intermediate step between tetragonal $P4_2/nmc$ and monoclinic $P2_1/c$, while orthorhombic $Pca2_1$ as alternative to monoclinic $P2_1/c$ have been considered, respectively.

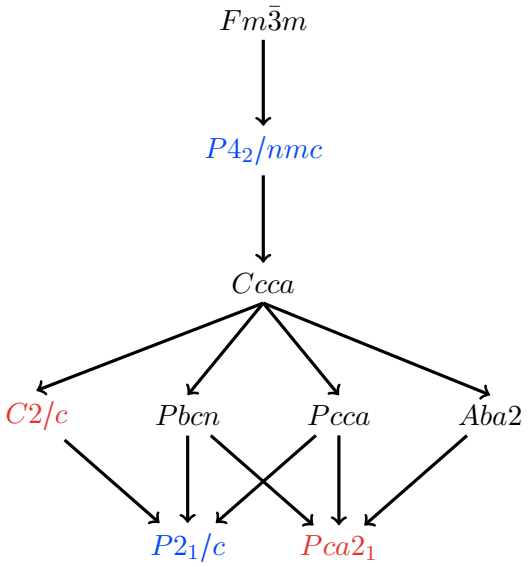

Figure 3.23: Group-subgroup lattices for $Fm\bar{3}m$ – $P2_1/c$ – $Pca2_1$ space groups.

Recent works shown the first experimental evidences about the orthorhombic phase formation at RT, even if particular external anisotropic constraints are applied [160, 161]. Other works reported how orthorhombic phase could be achieved in zirconia doped materials, where the internal stresses are introduced by doping cations that avoid the common $t \rightarrow m$ transition [162, 163].

Commonly the doping of zirconia is a wide known method to stabilize its tetragonal or cubic polymorphs. Phenomenologically, the reason why the Ta(V) stabilizes the orthorhombic phase should be view in terms of internal stresses and lacking of oxygen vacancies: a) it seems that Ta(V) doping generate internal local compressive stresses that hinder the monoclinic to tetragonal transformation, thus stabilizing the orthorhombic zirconia phase [159]; b) unlike the well-known case of Y(III) doping, in which two atoms introduce one oxygen vacancy in the zirconia structure leading the tetragonal or cubic stabilization, Ta(V) does not introduce any compensating vacancy. The Zr(IV) coordination number remains 7 and only structural changes are introduced by the smaller size of the doping cation. In conclusions, although it cannot beforehand exclude the formation of a fully orthorhombic structure, the hypothesis about having a slightly distorted monoclinic structure with the cell parameters very close to an orthorhombic one seems, until now, to be realistic.

Raman Spectroscopy

The Raman spectroscopy results have been in complete agreement with the findings obtained from XRPD patterns. As shown in Figure 3.24, for the sake of simplicity, it is possible to divide the Raman spectra into three different groups: low (ZT1 and ZT3), middle (ZT4 and ZT5) and high dopant-content (ZT8, ZT12 and ZT20) spectra. At a first glance, the first group revealed the presence of the monoclinic structure as the dominant phase. This symmetry is distinguishable by 18 Raman-active modes [115]. Unlike the XRPD patterns, a second phase is not still detectable in the Raman spectrum of sample ZT3, even though a peak broadening has been observed.

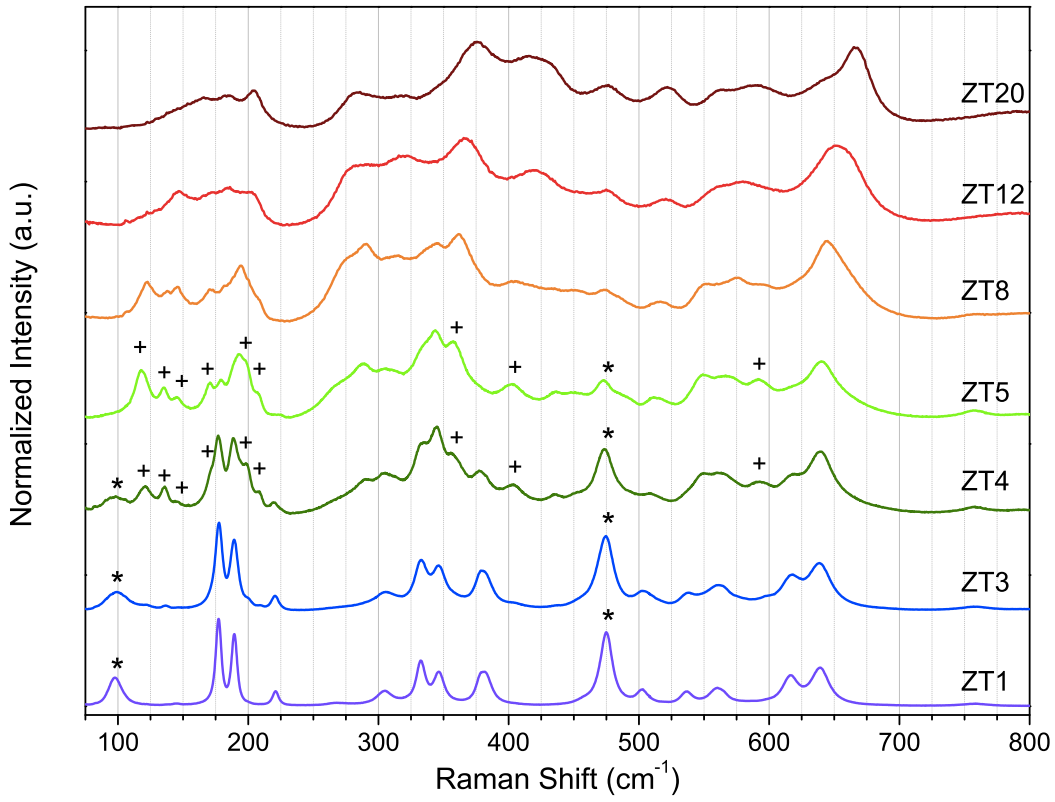

Figure 3.24: Raman spectra of ZT series calcined powders at 1000 °C.

The second group clearly show the co-presence of monoclinic structure with a different polymorph. In particular, new weak lines in the low-frequency range at 146, 170, 180, 208 cm^{-1} (marked with a cross +) that could be characteristics of an orthorhombic system, have been observed [164–166]. Moreover, also the 359, 405 and 593 cm^{-1} peaks can be ascribed to the new phase, referred from now as orthorhombic. At the same time the intensity of the isolated monoclinic Raman modes at 96 and 475 cm^{-1} (marked with a star $*$) contemporaneously decrease.

These spectral features indicate that the PN phase content increases, while the monoclinic one decreases progressively. Above 5 mol% of Ta doping, the related peaks to the monoclinic polymorph has not been clearly detectable, especially those at 96 and 475 cm^{-1}. Finally, the third group (ZT8, ZT12 and ZT20) spectra profiles differ slightly among them, maintain the features of the orthorhombic symmetry.

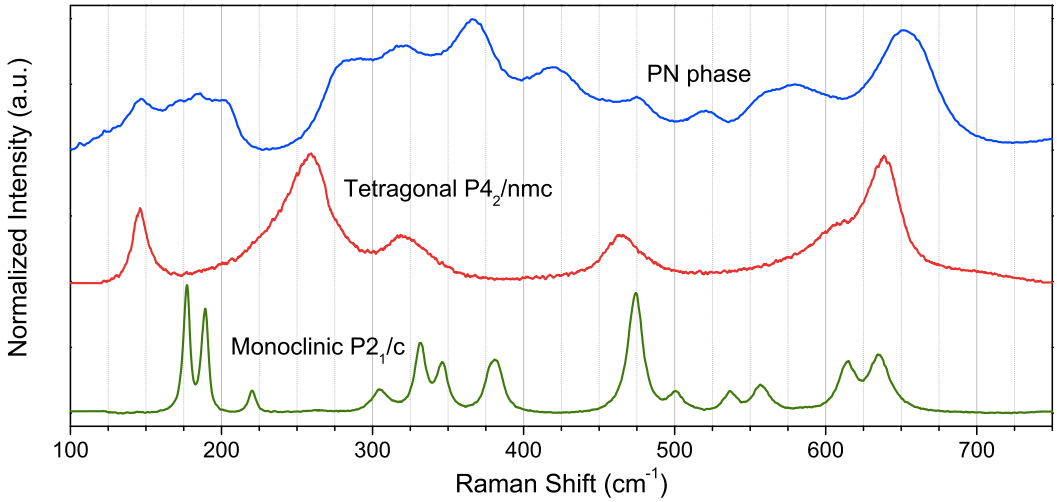

Figure 3.25: Zirconia single phase Raman spectra.

Table 3.9: Theoretical Raman-active modes for the atomic sites (Wyckoff positions) relative to the investigated space group of the zirconia polymorphs.

Mode	$P4_2/nmc$		$Pca2_1$	$C2/c$		$P2_1/c$
	$2a/2b$	$4a$	$4a$	$4e$	$8f$	$4e$
A_{1g}		1				
B_{1g}	1	1				
E_{1g}	1	2				
A_1			3			
B_1			3			
A_2			3			
B_2			3			
A_g				1		3
B_g				2		3
A_u					3	
B_u					3	
Sites	Zr	O	Zr, O1, O2	Zr	O	Zr, O1, O2
Total	6		36	9		18

The experimental data of the PN phase structure have been compared with the literature ones, keeping in mind the XRPD results. First, the *Pbcm* geometry can be excluded as a candidate for the orthorhombic phase, since several authors [165, 167] considering it as a not reliable structure for a stable polymorph of zirconia

[168]. Also the *Pnma*, structure, seems to give a quite different spectrum pattern, having different vibration modes [169], and thus can be excluded as well. Moreover, the *Pbca* Raman spectrum reported by different authors does not match exactly with the spectra experimentally achieved, even though, in the first range of the spectra, new frequencies are not clearly distinguishable due to the overlap with those of the monoclinic symmetry. Therefore, according to the results obtained by the analysis of the XRPD patterns, only the $Pca2_1$ symmetry has been considered for the description of the phase. Since the $Pca2_1$ Raman spectrum has not yet been reported, this phase as indicate from XRPD results and from the Raman spectra obtained, could be considered as a slightly distorted monoclinic structure. In fact, looking at the high concentration dopant series spectra (*i.e.* 8-20 mol%), the main change, as a result of subsequent Ta(V) doping, consists in a continuous broadening and shifts of the peaks frequency. This is a common observation in Raman spectroscopy of solid solutions when disorder due to a substituting dopant is introduced in the crystal structure [170]. Surely, Raman data about $C2/c$ cell are not reported too, since its existence has been proposed in this project for the first time. Actually monoclinic ($P2_1/c$) to orthorhombic phase transformation required only a slight structural change, as already mentioned. Nevertheless, it is only observed in his pure form as a high-pressure polymorph [115, 164, 166, 167, 171] or as isolated island on a sapphire substrate [165]. Here, for the first time, the Raman spectrum of this phase at room temperature and at normal pressure has been observed.

Of course, prediction of the $Pca2_1$ Raman modes by first-principles calculations will help to elucidate and confirm the spectrum associated to this structure. The evolution of the different zirconia polymorph Raman spectra have been reported in Figure 3.25: undoped ZrO_2 for monoclinic, ZT12 sample for PN phase and ZY8 for tetragonal [7].

From the Raman theory, it is possible to check how many Raman-active modes are correlated with the atomic sites for each polymorphs. In Table 3.9, the Raman-active modes have been reported for the Space Group investigated and their relative Wyckoff positions. From Table 3.9, the total number of theoretical modes for $Pca2_1$ (36) is higher than the $C2/c$ (globally 9) ones. Observing the spectrum shape of the PN phase, it seems that more than 9 modes are present. So, at least qualitatively, the Raman spectroscopy seems to favor the orthorhombic solution respect to the monoclinic one.

In situ X-ray Powders Diffractometry (XRPD)

The XRPD patterns in Figure 3.20 evidence that, in the investigated samples with higher tantalum content, the monoclinic phase decreases, while the PN phase in-

creases and no tetragonal phase is found when Ta(V) is added as a doping ion. As reported above, this seems to be in contrast with some papers on similar systems studied without a detailed and consistent phase analysis [61–64] . The three most significant samples ZT3, ZT5 and ZT8, one for each group reported above, have further been investigated with *in situ* XRPD by the synchrotron radiation. Figure 3.26 show the thermal evolution of the XRPD patterns from 100 °C to 1000 °C and the subsequent cooling down to RT, every 100°C.

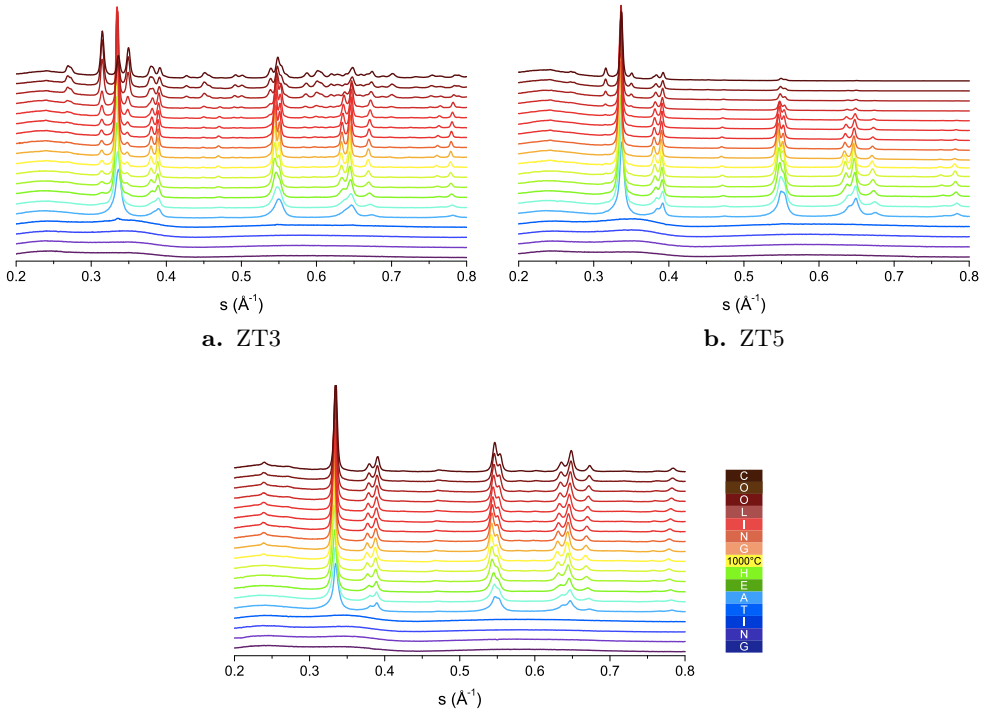

a. ZT3 **b.** ZT5

c. ZT8

Figure 3.26: *In situ* XRPD thermal patterns of the samples from 100°C to 1000°C and back with synchrotron radiation (λ =0.824 58 Å).

All the as prepared powders are amorphous at RT. This is coherent with the hydroxide co-precipitation synthesis method used. The crystallization process starts above around 400°C. This is verified for each sample. Up to 500°C, no crystalline peaks are detectable in the patterns. The PN phase starts to grow at the same temperature for all the samples. This demonstrates the role of the Ta(V) ion as stabilizer of the PN phase. The patterns of the ZT3 sample show the formation of a small amount of the monoclinic phase at temperature higher than 900°C. Then, during the cooling process, the monoclinic phase content increases, while the PN phase decreases as expected from the XRPD obtained at RT (see Figure 3.20). The monoclinic phase is still present in the sample ZT5, at 900°C, but in a smaller

amount. Again, during the cooling process below 300°C, monoclinic slightly grows up, while the amount of the PN phase decreases showing that the stabilization of this phase is not still completed. In the ZT8 no monoclinic phase is detectable at all. The PN phase that grows in that sample is the same during all the thermal process. This phase is stable until 1000°C and no transformation occurs even during the cooling.

The analysis of the cooling process is very interesting because it is an index of the thermal stability and some other useful properties for the ceramic materials could be determined. From the profile analysis made on the *in situ* XRPD patterns, the unit cell parameters have been refined. In this way, the cell volume could be estimated at different temperature. When a material is heated, the thermal agitation causes the bonds lengthening, the volume of crystalline materials increases and a correlation between volume and temperature, known as *Coefficient of Thermal Expansion (CTE)*, could be defined. From classic physics, the one-dimensional thermal elongation is

$$L = L_0(1 + \lambda T) \tag{3.7}$$

where L is the final length, L_0 is the initial length and λ is the linear CTE, characteristic for each material. For three-dimensional expansion, the expanded volume V of a cube, with L_0 initial side, is determined as follow

$$\begin{aligned} V &= [L_0(1 + \lambda T)]^3 = L_0^3(1 + 3\lambda T + 3\lambda^2 T^2 + \lambda^3 T^3) \\ &\approx V_0(1 + 3\lambda T) = V_0(1 + \alpha T) \end{aligned} \tag{3.8}$$

where V_0 is the initial volume and α is the volumetric CTE. The relation $\alpha = 3\lambda$ is true only for isotropic materials, *i.e.* those that expand equally in all directions. From the linear dependence between volume and temperature, α could be calculated as derivate

$$\alpha = \frac{1}{V_0}\frac{\mathrm{d}V}{\mathrm{d}T} \tag{3.9}$$

The α (or λ) values reported in literature are always referred at 20 °C, *i.e.* considering V_0 as the volume at that temperature.

From the microstructural point of view, the material with a non-cubic crystallographic system symmetry should be considered anisotropic, *i.e.* with different CTE along the three lattice parameters (a, b, c). As reported by Kisi and Howard, the lattice parameters of the different zirconia polymorphs, have well-defined linear behavior [158]. In this way, the volume linear behavior could be calculated for the same

validity range, and the crystal volumetric CTE could be estimated. Since the α (or λ) values are reported in literature for massive materials, *i.e.* with polycrystalline structure, the anisotropic effect, evident in a single crystal material, is mediated by the random crystals orientation. In first approximation, the α value calculated by this procedure could be considered as an average product of λ_a, λ_b and λ_c. The value of α extrapolated by the literature for monoclinic phase ($22.8 \cdot 10^{-6}\,\mathrm{K}^{-1}$) satisfied, inside the error range, the reported one in Table 3.10 calculated as product of the three lattice linear behavior ($V = bca\sin\beta$, $a\sin\beta$ is used instead of a in order to consider the angle) [172].

Taking these assumptions as correct, the evaluation of PN phase (considered as orthorhombic cell) CTE, not reported in literature yet, has been proposed. Figure 3.27 shows the behaviors of the calculated cell volumes obtained from the profile analysis of the XRPD synchrotron patterns.

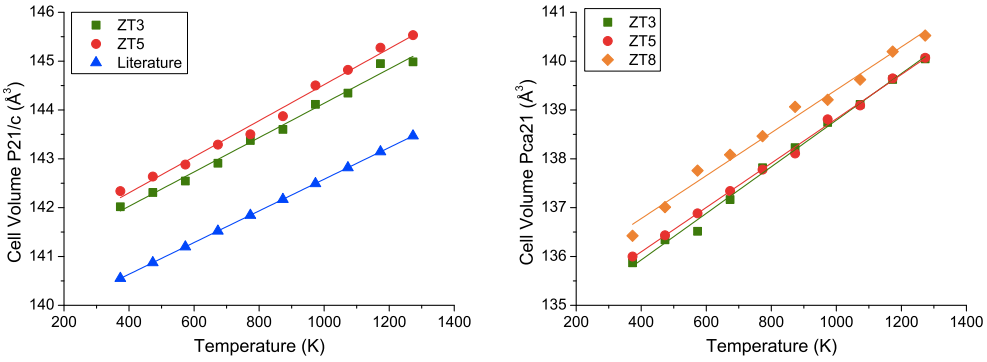

a. Monoclinic **b.** PN phase (as orthorhombic)

Figure 3.27: CTE for monoclinic and PN phases.

Table 3.10: Linear fit parameters for monoclinic phase volumetric CTE calculation.

	Intercept	Slope	R-Square	V_0 (Å^3)	α ($10^{-6}\,\mathrm{K}^{-1}$)
Literature	139.339 ± 0.001	0.003234 ± 0.000001	1.000	140.287	23.1
ZT3	140.6 ± 0.1	0.0035 ± 0.0001	0.989	141.6	24.7
ZT5	140.8 ± 0.1	0.0037 ± 0.0001	0.988	141.9	26.1

Table 3.11: Linear fit parameters for PN phase (as orthorhombic) volumetric CTE calculation.

	Intercept	Slope	R-Square	V_0 (Å^3)	α ($10^{-6}\,\mathrm{K}^{-1}$)
ZT3	134.0 ± 0.1	0.0048 ± 0.0001	0.994	135.4	35.4
ZT5	134.28 ± 0.01	0.00454 ± 0.00001	0.998	135.61	33.5
ZT8	135.0 ± 0.1	0.0044 ± 0.0001	0.986	136.3	32.3

Independently from the doping amount, the very similar slopes of the lines underlined the same behavior for each phase. The Ta content concerns, instead, the intercepts values, higher the doping amount bigger the cell volume.

Considering the zirconia engineering availability as Thermal Barrier Coating (TBC), a good blades protection is achieved when the top coat has a) high melting point, b) low density, c) low coefficient of thermal conductivity, d) good corrosion, oxidation and wear resistance and e) a CTE value very similar to the substrate one [173]. Usually the zirconia YSZ, used for this application has a CTE of $31 \cdot 10^{-6}\,K^{-1}$. The superalloy metal substrates of the turbine blades, such as Hastelloy® or Inconel®[9], have values around 36-44 $\cdot 10^{-6}\,K^{-1}$. From this study the CTE of Ta-doped zirconia materials is higher than the YSZ one. So, the difference between substrate and coating CTE values is smaller and a better protection should be achieved. Furthermore, as already discussed, some examples in literature are reported about the improvement of the corrosion resistance [57–60] and the lowering of the thermal conductivity coefficient [174] in the Ta-doped zirconia materials.

3.4 Zirconia Tantalum-doped sintered materials

In this paragraph, the last part of the project about the zirconia structural study has been presented. A first attempt about the production of sintered Ta-doped zirconia materials with PN phase has been presented.

3.4.1 Structural analyses

Wide Angle X-ray Scattering (WAXS)

Two series of specimens have been prepared: SPS1150 (T=1150 °C, P=100 MPa, t=5 min) and SPS1250 (T=1250 °C, P=75 MPa, t=5 min). A sintered material has been considered as *full-dense* when its bulk density is as close as possible to its theoretical density[10]. In Table 3.12 the calculated bulk density, by Archimedes' method, have been reported.

As clearly reported in Table 3.12, the density of the same specimen is higher for the second experimental conditions (SPS1250). The quantities of the monoclinic phase have been calculated from the Rietveld analysis of the WAXS patterns re-

[9] Nickel-Chromium-based superalloys.

[10] The theoretical density of a crystalline material is calculated from its lattice parameters by the formula

$$\rho = \frac{ZM}{V_{cell} N_A} \tag{3.10}$$

where Z is the number of asymmetric unit into the cell, M is the molecular weight of the compound, V_{cell} is the unit cell volume and N_A is the Avogadro's number ($6.022 \cdot 10^{23}\,mol^{-1}$).

Table 3.12: Bulk density of SPS specimens. The values in brackets are relative to the theoretical density estimated considering the Rietveld refinement phase content and the PN phase as orthorhombic.

	Bulk density ($g\,cm^{-3}$)	
	SPS1150 series	SPS1250 series
ZT5SPS	5.965 (96.8%)	6.094 (98.9%)
ZT8SPS	6.262 (98.8%)	6.340 (99.5%)
ZT12SPS	6.505 (98.1%)	6.547 (98.8%)

ported in Table 3.13. The specimens show a similar behavior increasing the Ta quantity. The classic monoclinic phase ($P2_1/c$) amount clearly decreases from 5% to 12% of doping as shown in Figure 3.28. This could be an evidence of the gradual PN phase stabilization by Ta content. Finally, it is worth noting that the completely stabilization of the PN phase at 1000 °C, demonstrated by the *in situ* XRPD patterns performed at the Synchrotron facility, is not possible at the two sintering temperature, moreover higher the temperature higher is the monoclinic content. From the patterns comparison in Figure 3.29, a different phase content is visible for the three experimental conditions (calcined powders at 1000 °C, sintered materials *via* SPS at 1150 °C and at 1250 °C).

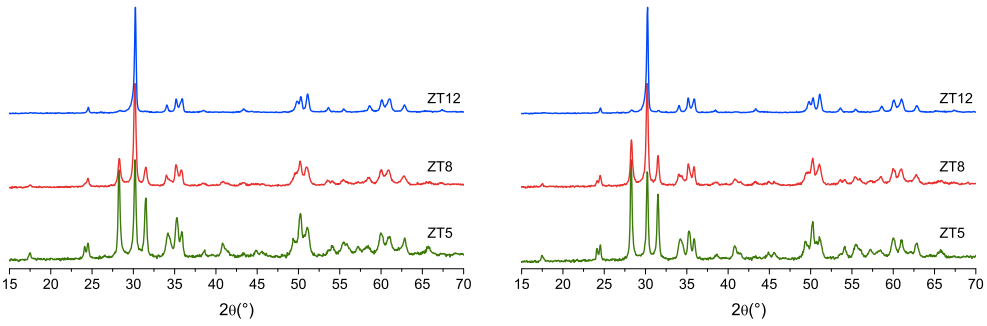

a. SPS1150 series **b.** SPS1250 series

Figure 3.28: WAXS patterns of the sintered SPS1150 and SPS1250 series.

These data revealed that, probably, higher doping content it is necessary to completely stabilize the PN phase in full-dense sintered material. SPS specimens at 1000°C, also with a uniaxial pressure pre-consolidation of the powder at 1.24 GPa ($10t_f$), have been performed. The specimens shown around 80% of the theoretical density, too much low in order to performed mechanical tests. The WAXS patterns of these specimens did not show any monoclinic residuals (data not reported).

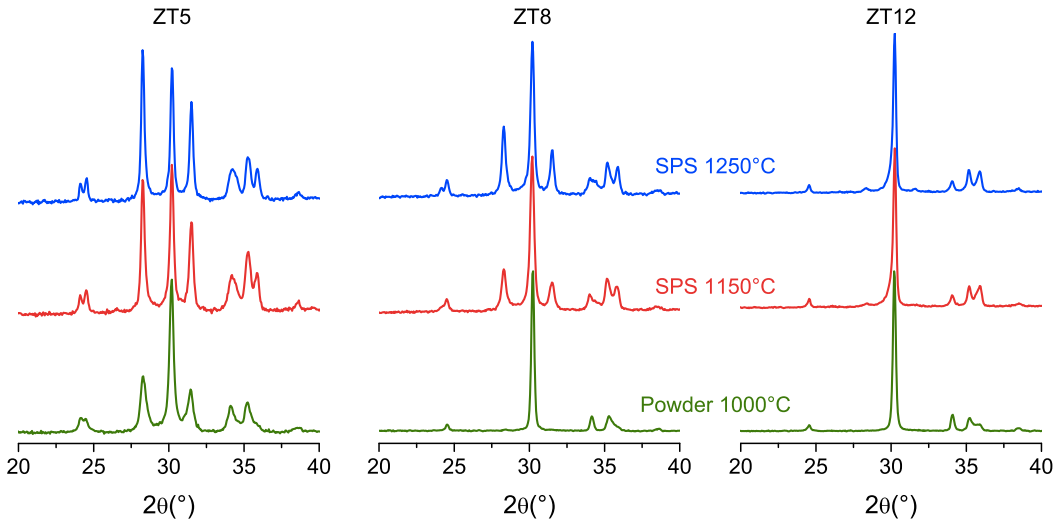

Figure 3.29: Comparison between XRD patterns of sintered materials and powders ones.

Scanning Electronic Microscopy (FE-SEM)

In Figure 3.30, the FE-SEM images of the polished and annealed surface of SPS specimens have been reported. In order to emphasize a compositional contrast, the images have been recorded in Backscattered Electrons (BSE) mode.

An evident atomic weight contrast is visible on the polished surface of the sintered specimens. The lighter zones are related to the heavier composition grains, so they are richer in heavier element, *i.e.* Ta. It is worth noting that the lighter zones increased from 5% to 12% of Ta as expected by the Rietveld refinements. The punctual Energy Dispersive X-ray Spectrometry (EDS) analyses of the two different zones (Figure 3.33), point out a higher percentage of Ta on the lighter grains. Instead, the darker zones are very poor in doping cation. Considering tantalum as PN phase stabilizer, the lighter grains could be associated to PN phase and the darker to the classic monoclinic one. The results of the statistical analysis based on the grayscale quantification of the two zones made with the ImageJ program has been reported in Table 3.13. The quantitative estimation matches very well also with the Rietveld calculations, independently to the considered space group for the PN phase. The difference between the two specimen series has also been estimated. A good agreement with WAXS patterns has been found as clearly evidenced in Figure 3.31.

Observing carefully the Figure 3.30 it is possible to distinguish also the grain boundaries between the two areas. In order to emphasize the grain boundaries the same focused fragments have been recorded in Secondary Electrons (SE) mode, which displays a morphological contrast. In Figure 3.32 an evident comparison

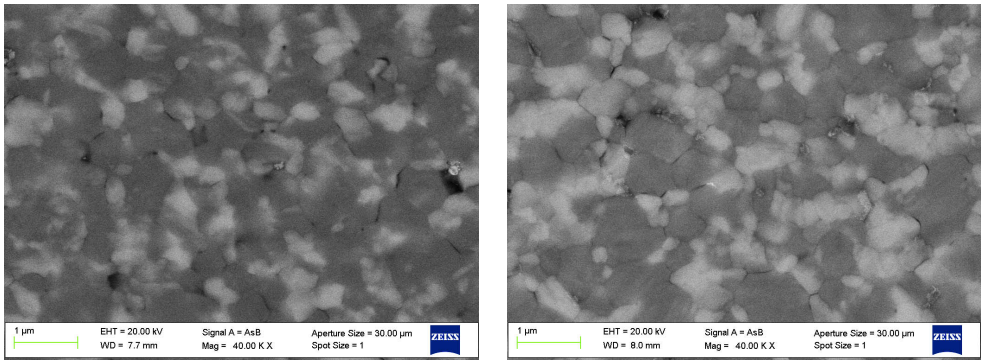

a. ZT5SPS1150 **b.** ZT5SPS1250

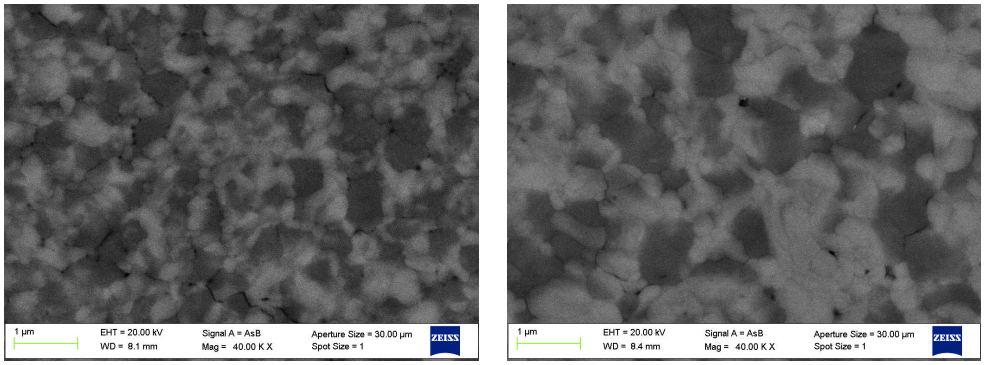

c. ZT8SPS1150 **d.** ZT8SPS1250

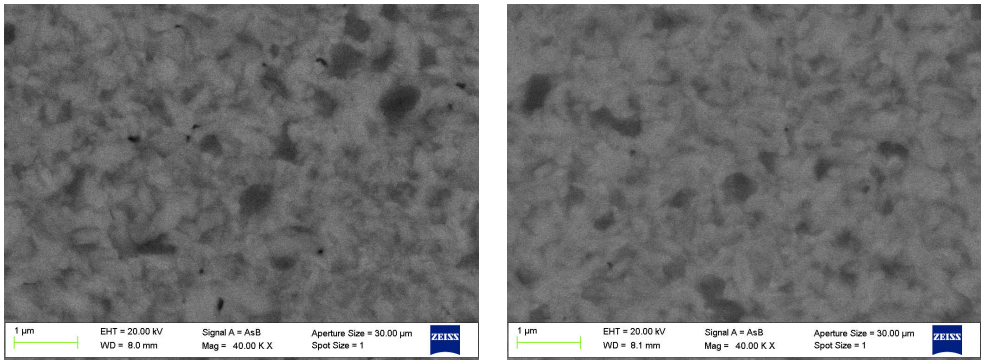

e. ZT12SPS1150 **f.** ZT12SPS1250

Figure 3.30: FE-SEM images in BSE mode of the polished SPS specimens surfaces.

between the BSE and SE mode of the same pictures has been reported.

From these experimental evidence, the grain size for the two different EDS zones has been estimated. Once again, the ImageJ program has been used for the determination of the grain area A and its perimeter p. The equivalent planar diameter D has been estimated as follow

$$D = \sqrt{\frac{4A}{\pi}} \tag{3.11}$$

Table 3.13: Comparison between statistical estimation of the dark zones in FE-SEM images (BSE mode) and monoclinic quantification by Rietveld method on WAXS patterns.

	SPS1150 series		SPS1250 series	
	BSE dark zones %	WAXS monoclinic %	BSE dark zones %	WAXS monoclinic %
ZT5SPS	55 ± 4	53 ± 3	61 ± 4	59 ± 3
ZT8SPS	38 ± 4	41 ± 3	40 ± 4	42 ± 3
ZT12SPS	11 ± 2	10 ± 3	13 ± 4	11 ± 3

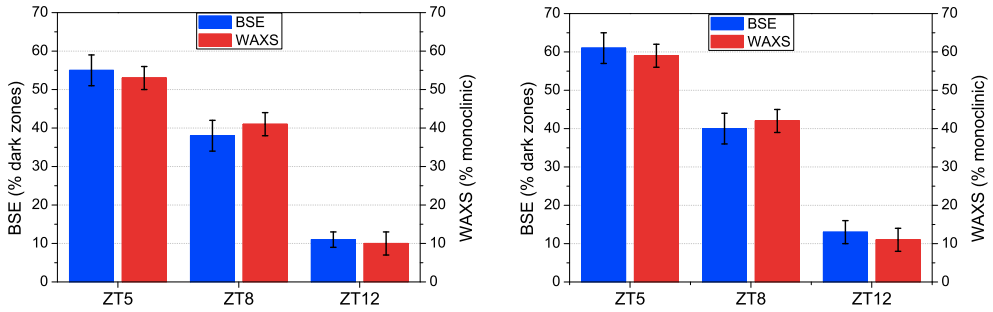

a. SPS1150 series **b.** SPS1250 series

Figure 3.31: Comparison between statistical estimation of the dark zones in FE-SEM images (BSE mode) and monoclinic quantification by Rietveld method on WAXS patterns.

Another important value is the *shape factor* F that has been determined as follow

$$F = \frac{4\pi A}{p^2} \tag{3.12}$$

The shape factor indicates how the grains have been close to the ideal circular shape, so it takes values between 0 (infinitely elongated grain) and 1 (ideal circular grain). In Table 3.14 the statistical estimation of the grain size and the relative shape factor have been reported. At least 300 grains per type have been considered for the statistics.

From the above reported data, the light grains are smaller than the dark ones. The monoclinic phase grows more rapidly than the PN phase, because of it is poorer in doping cation. Observing the shape factor, both the grain types show the same growth path, without any preferential elongation.

Figure 3.33 show the comparison between the EDS spectra of the bulk samples, and the comparison between the different compositional zones for each sample. From EDS analysis an elemental composition estimation has also been achieved. The

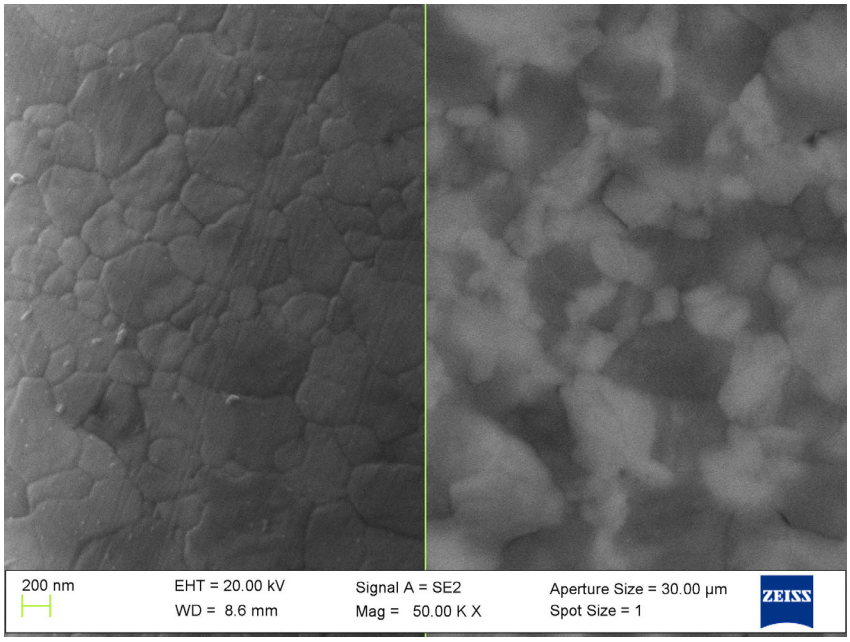

Figure 3.32: Comparison between SE (right) and BSE (left) mode fragment of the specimen ZT8SPS1250.

Table 3.14: SPS specimens grain size D statistical estimation and shape factor F.

	SPS1150 series				SPS1250 series			
	Dark grain		Light grain		Dark grain		Light grain	
	D (nm)	F	D (nm)	F	D (nm)	F	D (nm)	F
ZT5SPS	550 ± 80	0.69	320 ± 60	0.66	600 ± 80	0.69	350 ± 40	0.68
ZT8SPS	560 ± 70	0.69	340 ± 50	0.67	580 ± 60	0.70	330 ± 60	0.67
ZT12SPS	540 ± 50	0.68	350 ± 40	0.67	590 ± 30	0.69	340 ± 30	0.68

quantitative evaluation has been made on the peaks areas relative to Zr and Ta energy lines (Zr: L_I =1.792 keV, $L_{\alpha 1}$ =2.042 keV, $L_{\beta 1}$ =2.124 keV, $L_{\beta 2}$ =2.219 keV and Ta: M_Z =1.329 keV, $M_{\alpha 12}$ =1.71 keV, M_β =1.765 keV). The lowest beam energy (5 keV) is used in order to achieve a more superficial signal minimizing the pear-shaped interaction volume.

The quantitative results, on the average composition of the specimens reported in Table 3.15, match very well the nominal content of the as prepared powders. The tantalum signal in Figure 3.33a and Figure 3.33b increases from sample ZT5 to ZT12 as foreseen by the BSE images. No differences have been registered between the two sintering condition series. An important consideration must be done on the punctual analyses performed on the two grayscale areas. In each sample, the same spectrum has been measured, both for light and dark grains. Once again, it

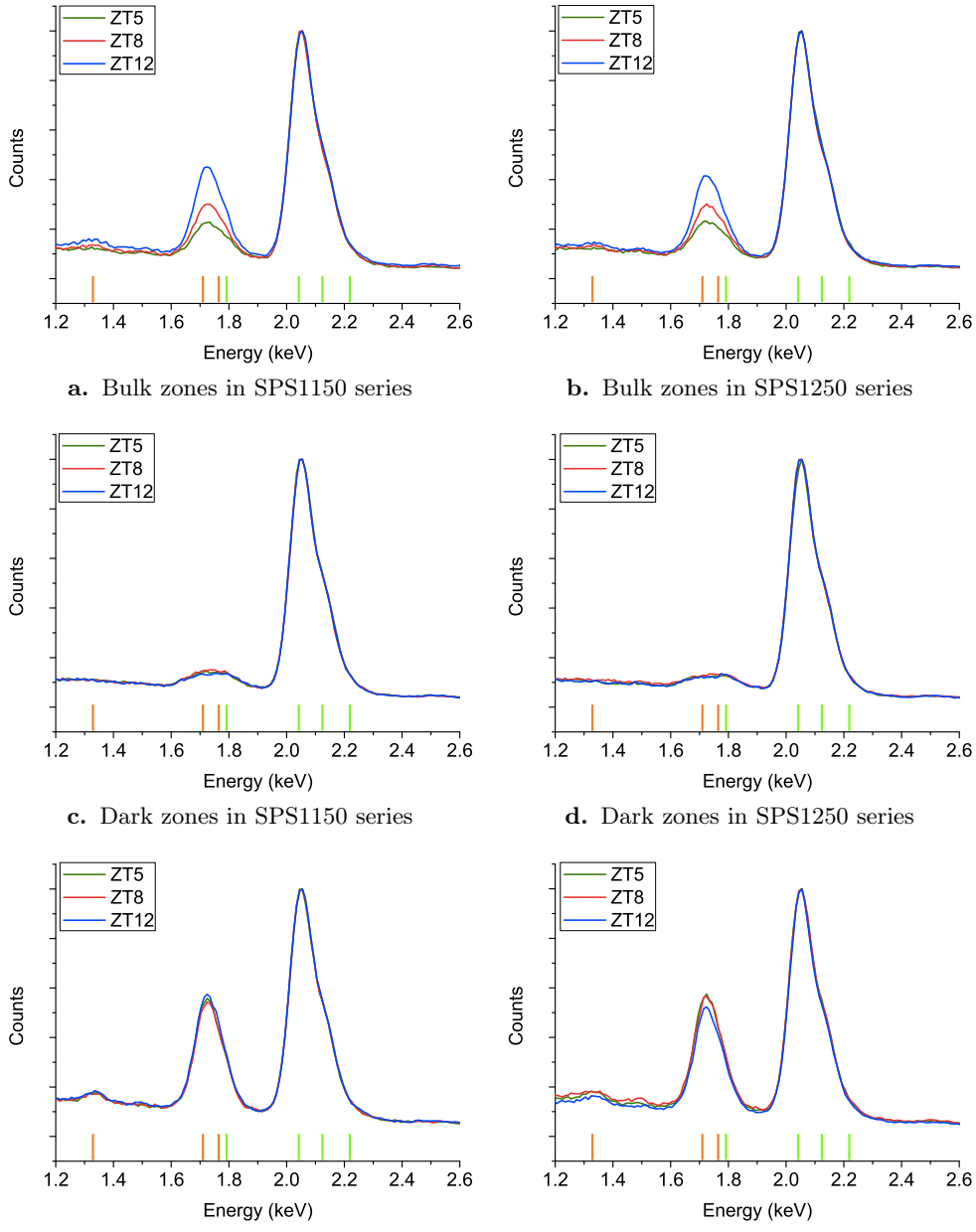

a. Bulk zones in SPS1150 series

b. Bulk zones in SPS1250 series

c. Dark zones in SPS1150 series

d. Dark zones in SPS1250 series

e. Light zones in SPS1150 series

f. Light zones in SPS1250 series

Figure 3.33: EDS analyses on bulk, dark and light zones in SPS series. The orange lines are related to Ta (M_Z =1.329 keV, $M_{\alpha 12}$ =1.710 keV, M_β =1.765 keV), the green lines are related to Zr (L_I =1.792 keV, $L_{\alpha 1}$ =2.042 keV, $L_{\beta 1}$ =2.124 keV, $L_{\beta 2}$ =2.219 keV).

seems that the former is related to the classic monoclinic phase and the latter to the PN phase. A constant composition for each phase has been estimated. The dark monoclinic grains are very poor in Ta that do not stabilize another zirconia phase. This assumption could suggest the Ta-poor phase (*i.e.* the monoclinic) separation,

which maybe occur during the cooling rate of the SPS process. Observing the Ta-richer phase, it has a rough formula very similar to the $Ta_2Zr_8O_{21}$ phase, which is already reported in literature by Sellar [70]. An average content of Ta around 15-16mol% seems be the minor doping amount for a full stabilization of the PN phase.

Table 3.15: Tantalum molar quantitative estimation from EDS peaks analyses.

	SPS1150 series			SPS1250 series		
	Ta % bulk	Ta % dark	Ta % light	Ta % bulk	Ta % dark	Ta % light
ZT5SPS	5 ± 1	2 ± 1	15 ± 1	5 ± 1	2 ± 1	15 ± 1
ZT8SPS	8 ± 1	2 ± 1	16 ± 1	8 ± 1	2 ± 1	16 ± 1
ZT12SPS	13 ± 1	2 ± 1	16 ± 1	12 ± 1	2 ± 1	15 ± 1

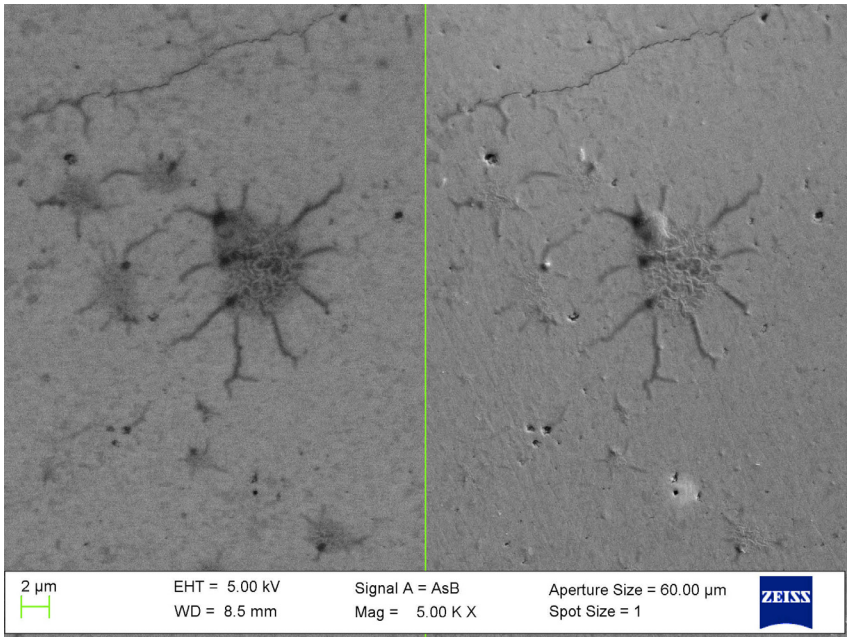

Figure 3.34: Sintered zirconia (ZT12SPS1250) crack fractures FE-SEM image in BSE mode (left) and normal mode (right).

Finally, another interesting experimental evidence has been observed. From data reported in Subsection 3.3 on page 57, it is worth noting the different thermal behavior of the two phases, *i.e.* monoclinic expanded less than PN phase. This means that during cooling a weakening between the two phases boundaries occurs. It could produce radial micro-fractures around the inclusion, whose CTE is lower than that of the main phase [175]. In Figure 3.34 some fractures inside the sintered material are clearly visible. It is also evident, as the radial fractures are correlated to the lower weight fraction grains, *i.e.* the darker zone in the left side of the

figure recorded in BSE mode. These fractures are probably generated, during the cooling rate, by the lower thermal expansion of the monoclinic inclusion respect to the matrix behavior (PN phase). Once more the dark zone could be related to the monoclinic fraction of the materials.

3.4.2 Mechanical tests

As final argument, the first mechanical tests results performed on the Ta-doped zirconia sintered materials, have been proposed. This section has not been completed, because of the tests have been made in the last period of the project. Nevertheless, some interesting and uncommon behavior has been obtained. Therefore, this data could be proposed as starting point for a next and deeper study.

Compression test

In order to determine the mechanical strength, a material must be deformed by an increasing stress. The external stress produce a deformation of the specimen dimensions. In particular, for a compression test, the strain ε along the dimension L is

$$\varepsilon = -\frac{\Delta L}{L_0} = \frac{L_0 - L_i}{L_0} \tag{3.13}$$

where L_0 is the initial length and L_i is the final length. The stress σ is the pressure imposed on the specimen cross-section S

$$\sigma = \frac{F}{S} \tag{3.14}$$

where F is the applied compressive strength. Imposing an increasing stress and recording the relative strain, the well-known stress-strain curve are achieved.

Every material subjected to stress deforms itself. In the first part of the deformation, if the stress is removed the material, returns to its initial condition. This is called *elastic deformation*, which could be followed by a permanent *plastic deformation*, over the as called *yield point*. For ceramic materials, which are brittle, over the elastic deformation the material fails. In the elastic regime, the stress is linearly dependent by the strain as follow

$$\sigma = E\varepsilon \tag{3.15}$$

where E is the *Young's modulus* or *elastic modulus* for compression, which is an index of the material stiffness. In Figure 3.35, the compression strain-stress curves made on the SPS1250 series at 1100 °C have been proposed.

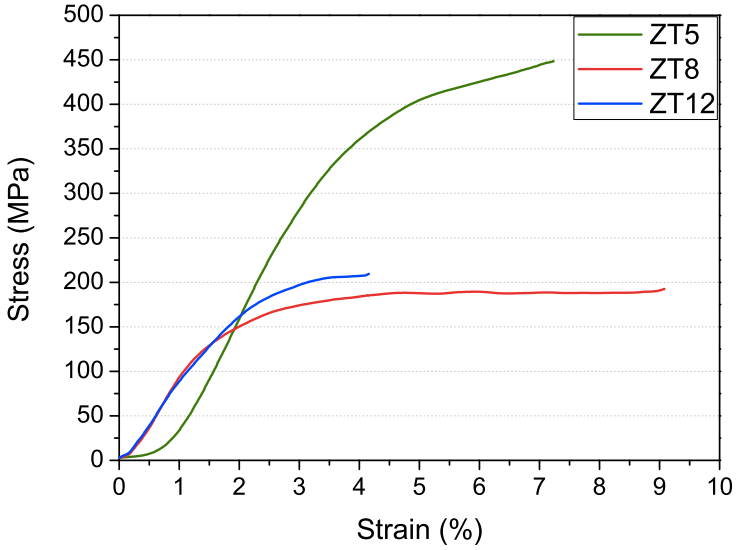

Figure 3.35: Compression stress-strain curves performed on SPS1250 series at 1100 °C.

Table 3.16: Compressive test data on SPS1250 series performed at 1100 °C with a compression rate of 5 µm/ min.

	E (GPa)	ΔL (mm)
ZT5SPS1250	13.6 ± 0.5	−0.19
ZT8SPS1250	11.7 ± 0.5	−0.34
ZT12SPS1250	10.3 ± 0.5	−0.17

The Young's modulus is related directly to the bond strength, so it depended also by the temperature. Since, at high temperature the atom separation is easier, E decreases with temperature. In literature the pure monoclinic zirconia elastic modulus at 1100 °C is 21 GPa, while it is 186 GPa at RT [172]. The presence of two or more phases affects also this property; in particular the phase with the lower modulus influences the overall mechanical behavior [176]. In Table 3.16, all the calculated moduli are evidently lower than the literature value already mentioned. The double phase (monoclinic and PN phase) present in SPS1250 series specimens reduces the materials stiffness. Besides, higher is the quantity of PN phase lower is the overall elastic modulus. In Figure 3.36 the Young's modulus dependencies on the Ta and the monoclinic phase content have been reported.

As reported in Figure 3.36a, an exponential decay of E (at 1100 °C) with the Ta content has been found. This trend it is very interesting because, over a specific threshold, the modulus reaches a constant value. This should be correlated to the modulus of a new phase, with a constant composition, *i.e.* the PN phase. It is worth

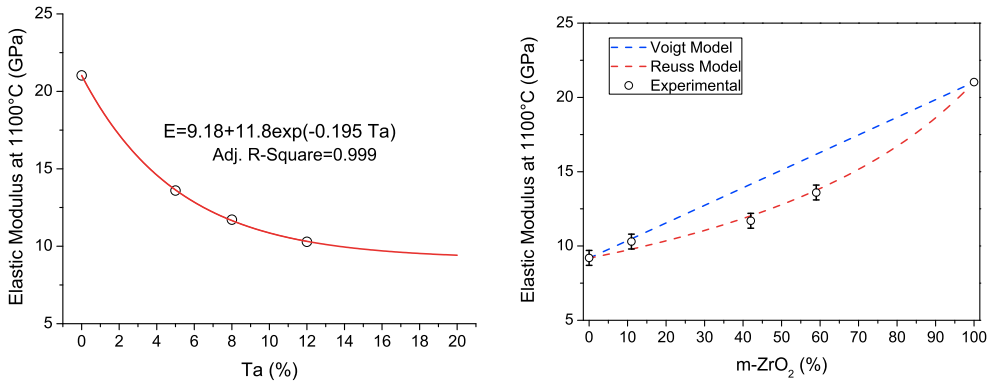

a. Ta content **b.** Monoclinic content

Figure 3.36: Elastic modulus at 1100 °C correlation with Ta content and monoclinic phase content.

noting that the curve asymptote (9.2 GPa) is reached over the 16 mol% of Ta which could be related to the composition of this new phase. The EDS analysis made on the PN phase (columns Ta % light in Table 3.15) suggestes similar result. So, even if only few data have been reported in Figure 3.36a, this result could be considered as the second raw evidence about the PN phase theoretical composition.

As already mentioned, the tantalum amount is directly connected to the PN phase quantity present in the ZT series. When two phases are present, the global modulus could be estimated by the combination of the single-phase moduli. Imposing the E =9.2 GPa as the PN pure phase modulus, it is possible to calculate the modulus variation with the phase content in the double phase system. Generally, it is possible to estimate the theoretical limits of the elastic modulus for a mixed phase system with two models. Assuming that the strain is the same in each phase (monoclinic m and PN phase in the present case), the Voigt model represents the elastic modulus upper limit as follow

$$E = V_m E_m + (1 - V_m) E_{\mathrm{PN}} \tag{3.16}$$

considering $V_m + V_{\mathrm{PN}} = 1$. Assuming, instead, that the stress is the same in each phase, the Reuss model represents the elastic modulus lower limit

$$\frac{1}{E} = \frac{V_m}{E_m} + \frac{1 - V_m}{E_{\mathrm{PN}}} \tag{3.17}$$

In Figure 3.36b, the Young's modulus against the monoclinic $P2_1/c$ volume fraction has been reported. The Voigt and the Reuss limits have been achieved placing E_m =21 GPa and E_{PN} =9.2 GPa. As shown, the elastic modulus extrapolated

from the stress-strain curves, are comprised between the theoretical limits of Voigt and Reuss. As the previous analysis, a deeper study and many data should be confirmed this first raw approximation. It seems clear that the PN phase is less stiff than the monoclinic one, *i.e.* the Ta-doped zirconia has a higher *strain tolerance*, which is another good property for the material engineering application as TBCs [173]. The strain tolerance increase is usually connected to a controlled porosity of the top coat in the TBCs technology, which however produced a less dense coating. The SPS Ta-doped zirconia materials are full-dense, so they could be provided a more compact layer with a high strain tolerance.

Creep test

The creep phenomenon occurs when a material is exposed at high temperature and constant stress. Depending on the type of material, creep is evident over a specific temperature, for ceramic material it must be higher than half of its melting point. Two main phenomena are involved during the creep deformation: *hardening* and *annealing*. The former increases the dislocation density and the mechanical strength of the material. The latter allows the dislocation diffusion and the recovery of the deformation process. During the test, the specimen is subjected to a constant stress, σ, and the corresponding strain, ε, is evaluated. The *strain rate* $\dot{\varepsilon}$ is calculated as the time derivate of the strain

$$\dot{\varepsilon} = \frac{\mathrm{d}\varepsilon}{\mathrm{d}t} \tag{3.18}$$

A typical creep curve could be divided in three steps. In the *primary* step (*transient*), governed by hardening, the $\dot{\varepsilon}$ decreases; the *secondary* step (*steady-state*), is characterized by a constant $\dot{\varepsilon}$ due to the balancing between the two above mentioned phenomena; and finally the *tertiary* step, where the $\dot{\varepsilon}$ increases in an uncontrollable way until the failure of the specimen, caused by the formation of necks and cavities inside the material. The secondary stage is the most important step, and it is characterized by the sequent general creep equation for the steady-state strain

$$\dot{\varepsilon} = \frac{B\sigma^n}{d^m} \exp\left(-\frac{Q}{k_B T}\right) \tag{3.19}$$

where B is a constant of the material, σ is the applied stress at temperature T, n is the *stress exponent*, Q is the *activation energy*, d is the grain size and m its exponent, and k_B is the Boltzmann constant[11]. The n and m values are characteristics of the creep mechanism, while the activation energy Q is an estimation of the

[11] $k_B = 1.38 \cdot 10^{-23}\,\mathrm{J\,K^{-1}}$

materials deformation resistance, higher the energy stronger the material.

The equation (3.19) has a stress-dependent part (power law) and a temperature-dependent part (Arrhenius type law), so the n and Q values could be experimentally calculated. The apparent stress exponent can be estimated from the stress dependence of the strain rate at constant temperature

$$n = \left(\frac{\partial \ln \dot{\varepsilon}}{\partial \ln \sigma} \right)_T \tag{3.20}$$

While the apparent activation energy can be estimated from the temperature dependence of the strain rate at constant stress

$$Q = -k_B \left(\frac{\partial \ln \dot{\varepsilon}}{\partial (1/T)} \right)_\sigma \tag{3.21}$$

the activation energy could be estimated per mole considering the relation between k_B and R, the ideal gas constant[12]. However the as calculated n and Q values are only apparent and usually overestimate the true values, which take into account the temperature dependence of the stress. Of course, also the grain size exponent m could be determined. Even if the creep equation is quite easy, in practice the creep mechanism identification is very difficult because it depends on both the chemical composition and the microstructure, moreover two or more mechanisms can occur at the same time [177].

In Figure 3.37 and Figure 3.38 the creep tests performed on ZT12SPS1250 specimen in air and in argon have been reported, respectively.

Comparing the data at the same experimental conditions (77 MPa at 1100 °C), it is worth noting that in air the specimen exhibits a higher strain rate. This could mean that the specimen microstructure is modified during the creep test by some oxidation process. Really, the specimen that was initially black after the SPS production, becomes white after the creep performed in air, while it does not change color in argon. The whitening of the sample heated in air (or oxygen richer atmosphere) is well known, *e.g.* the annealed polished specimens for the FE-SEM images are totally white. Commonly, the creep behavior of zirconia it is not influenced by oxidation process, unless a microstructural reconstruction is occurred, so, the presence of Ta seems to affect the specimen microstructure. Another qualitative observation is the specimen hardness after the test: the black sample is very hard, while the white sample is very soft. Some hypotheses could be done about this uncommon and unexpected behavior. Ceramic materials at high temperature are usually employed, they have a critical oxidation behavior, which could be further complicated when two or more phase are present. Each component has a different

[12] $R = k_B N_A$ =8.314 J mol^{-1} K^{-1} where N_A is the Avogadro's number.

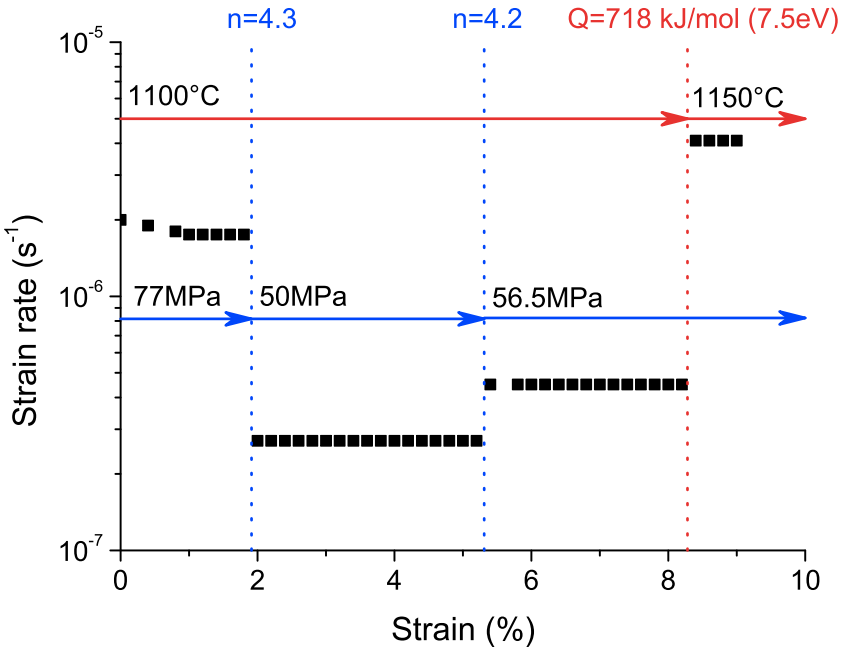

Figure 3.37: Creep rate of ZT12SPS1250 in air.

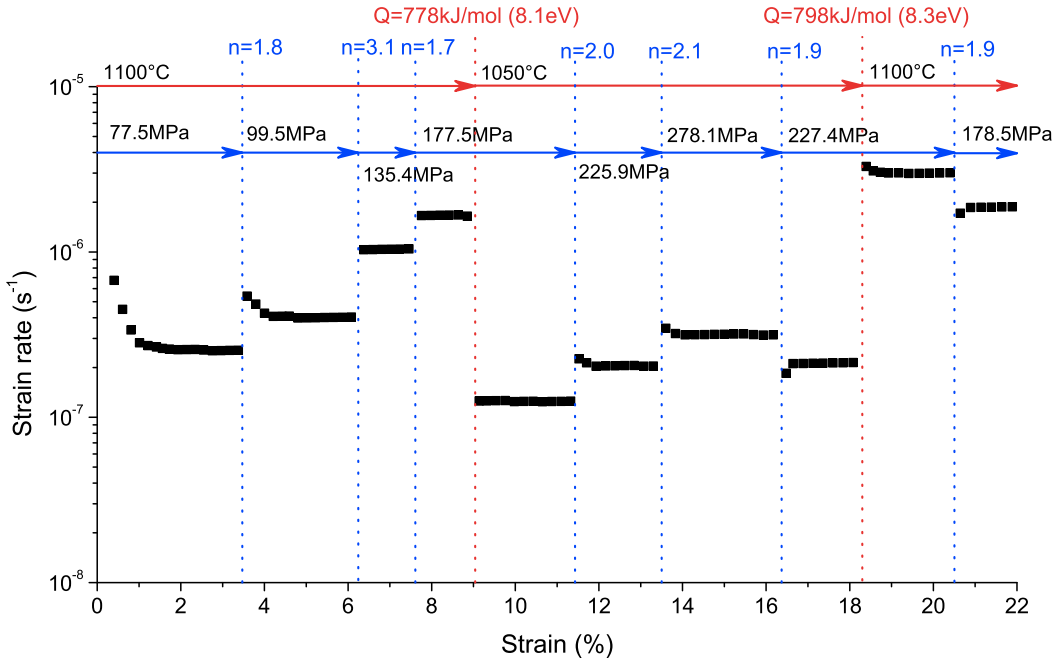

Figure 3.38: Creep rate of ZT12SPS1250 in argon.

behavior and the interface reaction must be considered. Other important factors are the stability, the crystallization, the transformation or the formation of new phases due to the element diffusion and the preferential oxidation [178].

As mentioned above, from the above creep curves, the n stress exponent could be calculated. From the equation (3.20), n has been estimated as slope of the strain rate-stress logarithmic linear plot, as proposed in Figure 3.39.

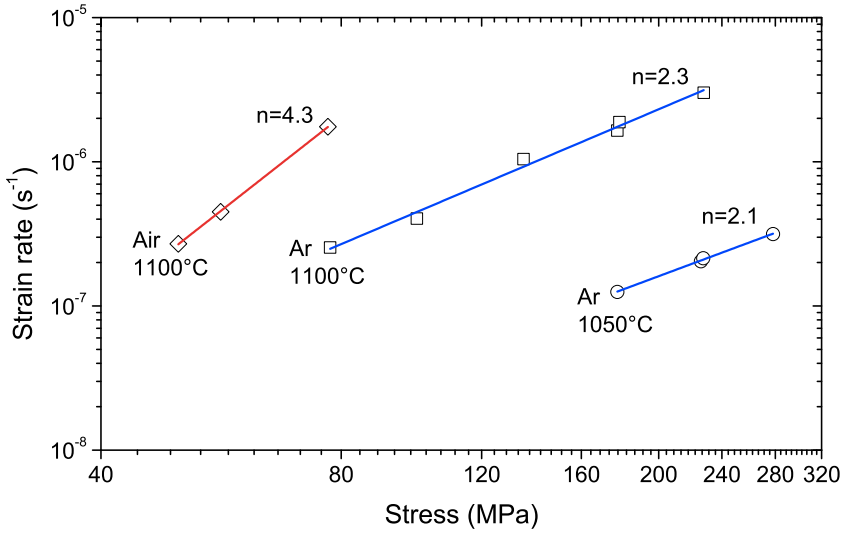

Figure 3.39: Stress exponent plot of ZT12SPS1250 specimen in air and argon.

As clearly reported, the stress exponent has a different value if the mechanical test is performed in air or in argon. In a reduced atmosphere $n \approx 2$, and different hypotheses could be done about this result. For example, a diffusion creep with an interface reaction control could take place [176, 179, 180]. In this mechanism the grain boundaries act as sources and sinks[13] for the vacancies and all the applied stresses drive their diffusion along the grain boundaries. The energy is spent to add or remove a vacancy from the grain boundaries and an interface reaction control occurs, also spending a part of the applied stress. Usually the interface processes are important for very fine-grained materials (with grain size below the micron) or in multi-phase system [180]. The stress quadratic-dependence of the strain rate can be correlated also at the *Grain Boundary Sliding (GBS)* creep. This type of creep is grain-size sensitive and alters the grains shape, which can slide on each other avoiding friction and the creation of big cavities. So, a small internal grain deformation against very large strain is achieved, except at the grain boundaries. The as called *superplastic deformation* takes place, which is the main reason of the high temperatures failure for ceramics, caused by the formation of a glassy phase into the grain boundaries [176].

In oxidative conditions, instead, $n \approx 4$ and a dislocation creep is possible. Dif-

[13]The *source-sink dynamics* is a theoretical model, developed by ecologists, used to describe how the habitat quality variation affects the growth or the decline of the population.

ferently from the previous case, it is grain-size insensitive and is held by climb and glide of the defects, moreover a dynamic recrystallization and preferred orientations can occur. In this case a climb controlled mechanism or dissolution of dislocation loops could be possible.

From the equation (3.21), the activation energy could be calculated when the strain rate is plotted logarithmically against $1/T$. Here, Q per mole has been achieved multiplying the slope of the linear fit by the ideal gas constant R. As reported in Figure 3.40, a higher activation energy is obtained when the creep is in argon, so in reduced atmosphere the material is stronger than in air, endorsing that the specimen is harder during the test in argon.

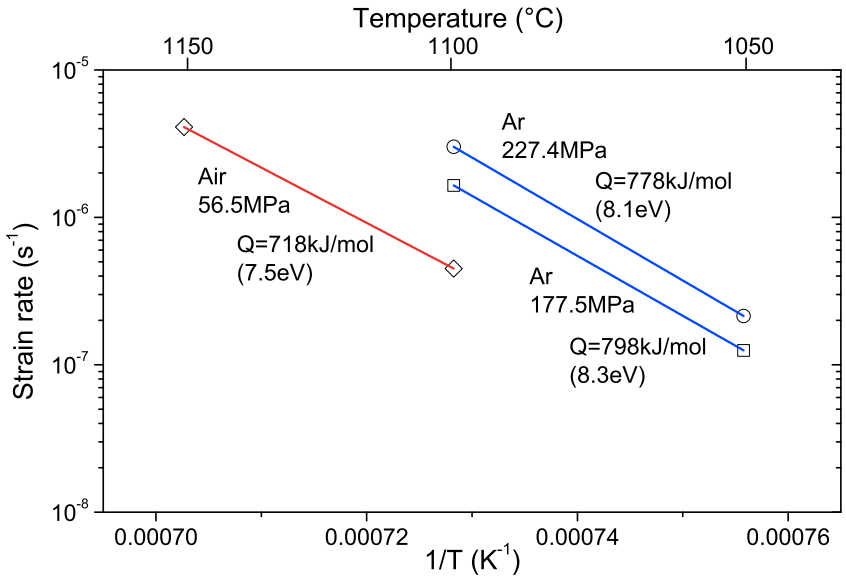

Figure 3.40: Activation energy plot of ZT12SPS1250 specimen in air and argon.

3.5 Mesoporous Zirconia Nanoparticles

3.5.1 Morphological characterization

The employment of a porous material as host specie depends principally on its morphological properties, such as shape, surface area and size. This is equally true in nanocarriers application field. As reported in Subsection 1.3.2 on page 15 the major problem for the zirconia porous nanomaterials is the low stability of its porous network. So, too much stressed thermal treatment should be avoided. In order to achieve zirconia NPs with a large surface area, avoiding any morphological changes or aggregation phenomena, a heat vacuum extraction process to remove the surfactant has been chosen. The n-alkyl primary amines boiling points study

developed by Ralston et al. has been very useful to perform the complete vacuum extraction of the template [181]. The crystallization causes the shrinkage of the zirconia sample with a consequent surface area reduction. This process, also known as glow phenomenon, has to be avoided [41, 102, 104, 105]. A Differential Scanning Calorimetry (DSC) on the MZNs has been performed in order to confirm the negative consequences of the calcination process, usually employed to remove the template. Crystallization process and an abrupt decrement of the porosity are the main harmful effects. In Figure 3.41a the exothermic peak around 300 °C is visible both in the as synthesized Z01 sample and in after the extraction process. This peak is related to the amorphous-to-crystalline transition. The consequences of this exothermic phenomenon is visible both in the XRPD patterns (Figure 3.43) and in the nitrogen physisorption analysis reported in Figure 3.44b. In Figure 3.41b a direct comparison between the Z01 sample as prepared and after the vacuum extraction has been proposed. The major difference between the TGA curves concerns the mass loss over 130 °C. This mass loss only in as synthesized MZNs is present, which still holds hexadecylamine (HDA) inside the network [182]. Thanks to the extraction process, the purified MZNs should have an amorphous and porous structure, since no phase transition happens with the correlated and unwanted shrinkage phenomenon.

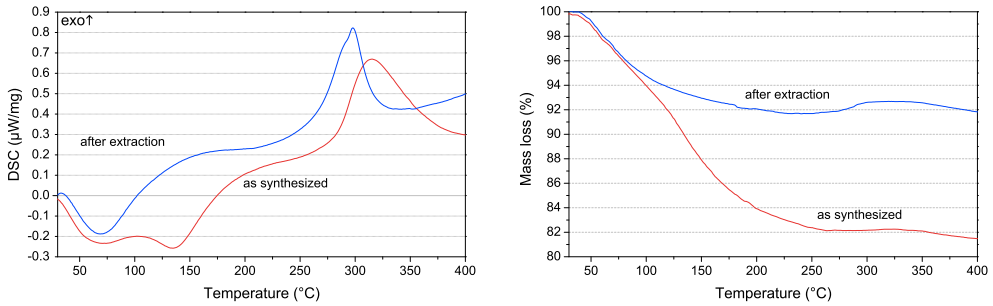

a. DSC **b.** TGA

Figure 3.41: Thermal analyses of MZNs (Z01) as prepared (red line) and after extraction process (blue line).

In Figure 3.42 the Z01 sample the infrared (IR) spectra before and after the vacuum extraction have been reported together with the HDA spectrum.

From the comparison between the spectra it is evident the amine presence into the pore network before the extraction process. The most intense signals below 3000 cm^{-1} are characteristic of the alkyl chains (stretching vibrations) of the surfactant tails. After the extraction (blue spectrum) these vibrations disappear, underlining the good process efficiency. In the same spectrum a peak around 3700 cm^{-1}, usually referred to the free hydroxyl groups is clearly visible. The presence of these groups on the MZNs surface should be fundamental for a surface functionalization.

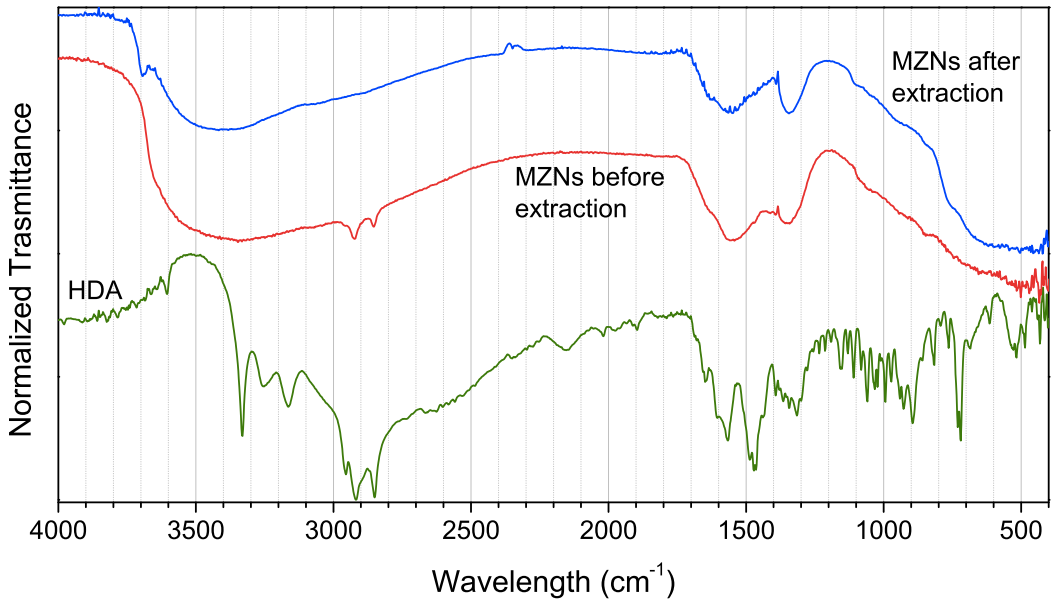

Figure 3.42: DRIFT-IR spectra of hexadecylamine (HDA) and MZNs (Z01) before and after vacuum extraction process.

In Figure 3.43 the Z01 sample patterns, taken as an example, before and after a thermal treatment at 350 °C have been proposed. This temperature has been chosen to verify a possible phase transformation after the exothermic peak present in Figure 3.41a.

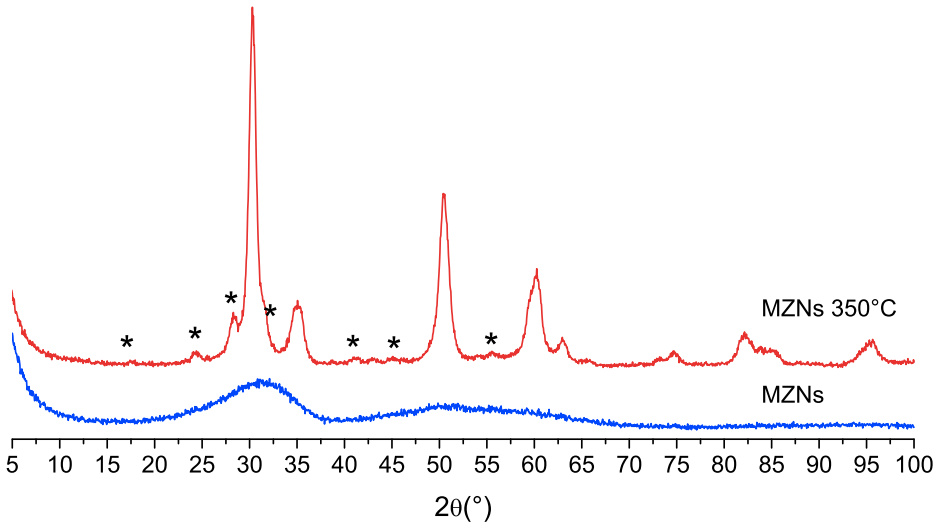

Figure 3.43: A representative XRPD pattern of the MZNs (Z01) after purification process *via* vacuum extraction, and after heating at 350 °C. The ∗-marked peaks are related to monoclinic zirconia phase.

Before heating, two evident halos are visible around 30° and 55°, which are

characteristics of an amorphous material pattern. No diffraction peaks have been detectable in the whole diffraction range [183]. In the MZNs heated at 350 °C pattern, the tetragonal zirconia reflections, with a slight amount of monoclinic phase (marked with $*$), confirmed that a calcination process at around 350 °C could promote the crystalline transition. The crystallization process, as already reported above in Subsection 1.3.2 on page 15, causes a reorganization of the microstructure of the NPs. When an amorphous material becomes crystalline, the volume decreases because of the atomic arrangement gets more order. So, shrinkage of the whole network is obtained, also with evident loss of specific surface area (see Figure 3.44b).

Figure 3.44 shows a representative nitrogen adsorption-desorption isotherm (sample Z01). All textural parameters (specific surface area, average pore size distribution and specific pore volume) have been summarized from Table 3.17 to Table 3.22.

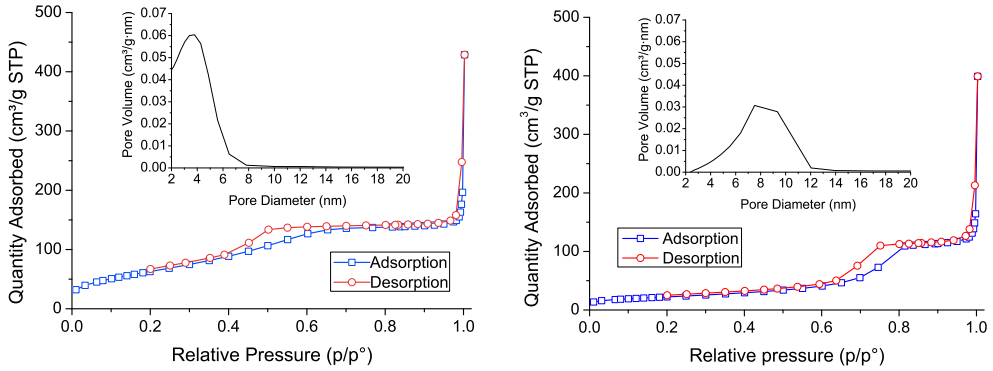

a. After extraction **b.** After heating at 350 °C

Figure 3.44: Characteristic adsorption-desorption curves of MZNs (Z01) as synthesized and before heating at 350 °C.

The isotherms of all the prepared samples displayed the type IV profile with a H1 hysteresis loop (according to the IUPAC classification), typical of mesoporous materials [184]. The samples show a specific surface area with values between 130 to 240 $m^2\,g^{-1}$. The pore size distributions according to the BJH model applied on the desorption branch of the isotherm are quite narrow. In Figure 3.44b the adsorption-desorption curves of MZNs samples Z01 after heating at 350 °C has been proposed. An evident change respect to the sample after vacuum extraction (Figure 3.44a) has been found. The surface area decreases from 240 $m^2\,g^{-1}$ to 80 $m^2\,g^{-1}$ after heating. An increment of the pore size should be attributed to the coalescence of the pores inside the shrinking network, but also to the MZNs agglomeration during the heating. So, this distribution could be correlated to a new internal pore distribution or it could be consequence of the space among the agglomerated NPs, as shown in Figure 3.46b. In this way, the thermal heating have a double undesired effect: the

loss of the surface area and the agglomeration of the NPs. The former limit the guest species loading capacity, the latter gets worse the distribution and dispersion properties of the NPs.

In Figure 3.45a a magnification of one MZN demonstrate the spherical shape of the particles and also its rough surface, which is characteristic of porous NPs with high surface area. In Figure 3.45b, instead, a population of MZNs with a sharp size distribution has been reported. In this figure it is evident as the particles are well dispersed on the plane and no agglomeration is visible. Figure 3.46a shows another well-dispersed population of MZNs. After heating over the above-mentioned amorphous-to-crystalline transition temperature (350 °C) the MZNs approach each other forming agglomerates, as reported in Figure 3.46b.

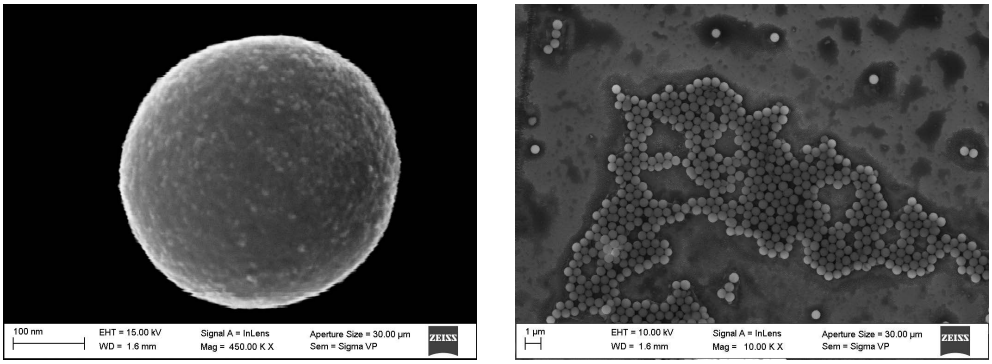

a. Single MZN (Z01) **b.** Population of MZNs (Z10)

Figure 3.45: FE-SEM images of MZNs example samples.

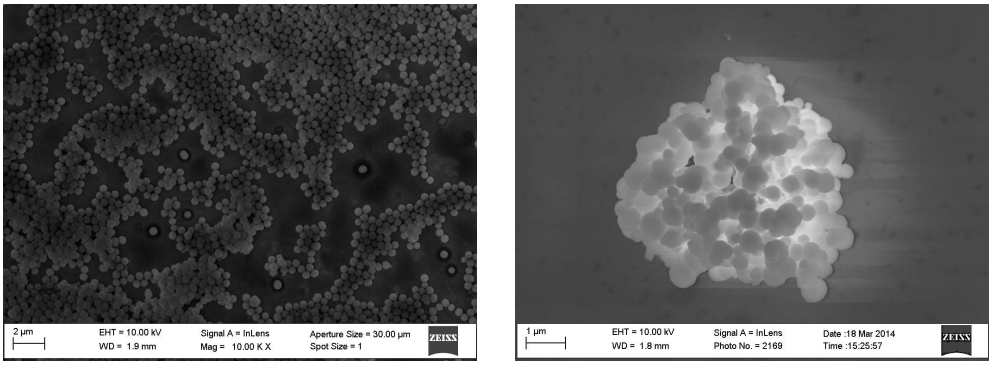

a. Well dispersed MZNs before heating **b.** Agglomeration of MZNs after heating

Figure 3.46: FE-SEM images of MZNs (Z01) before and after heating at 350 °C.

The Z01 sample has been taken as reference for all the investigations. The relative concentration of the reagents is the principal variable of the synthesis. The molar ratio proposed in Subsection 2.2.2 on page 25, has been the better for a

homogenous growth of the MZNs, to best of our knowledge. Different alkali halides (MX) and their concentration, surfactants and amount of water have been tested. The FE-SEM images, reported from Figure 3.47 to Figure 3.52, show all the samples prepared in order to propose an hypothetical synthesis mechanism.

First, the cation effect has been investigated, so different alkali chlorides (Li, Na, K, Rb, Cs) have been tested. The data relative to these samples have been reported in Table 3.17 and in Figure 3.47. All the systems present a well defined spherical particles with a short range of size. The low polydispersion of the average diameter, underline the optimal growth process of homogeneous MZNs. It is worth noting that the specific surface areas have similar values around $200\,m^2\,g^{-1}$. There are not significant differences between the mean pore diameters considering the standard deviation of the single values. The mean value is about 4 nm. Talking about the particles size, no apparent relationship between size and alkali chlorides is evident.

Table 3.17: Summary of MZNs alkali chlorides samples properties derived from nitrogen isotherms and FE-SEM measurements.

Label	MCl	BET surface area ($m^2\,g^{-1}$)	Total pore volume ($cm^3\,g^{-1}$)	BJH pore diameter (nm)	FE-SEM average MZNs diameter (nm)
Z02	LiCl	190	0.25	5.3 ± 2.0	620 ± 30
Z01	NaCl	240	0.23	3.4 ± 1.7	450 ± 20
Z03	KCl	230	0.22	3.6 ± 1.8	400 ± 30
Z04	RbCl	190	0.25	5.3 ± 2.0	460 ± 30
Z05	CsCl	220	0.23	3.8 ± 2.0	700 ± 70

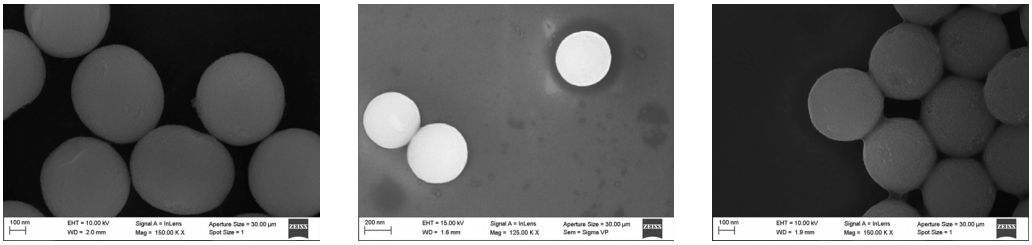

a. LiCl (Z02) **b.** NaCl (Z01) **c.** RbCl (Z04)

Figure 3.47: FE-SEM images of alkali chlorides MZNs series.

Secondly, the anion effect has also been explored testing different sodium halides (F, Cl, Br, I). The data of these samples have been reported in Table 3.18 and Figure 3.48. As in the previous case, the NPs present a well-defined spherical shape with a narrow distribution of the diameter. The specific surface is slightly reduced, because of the pore size increases.

Based on these experimental data, a discussion about the alkali halides effect has been proposed. The use of the different inorganic salts produces zirconia NPs with

Table 3.18: Summary of MZNs sodium halides samples properties derived from nitrogen isotherms and FE-SEM measurements.

Label	NaX	BET surface area ($m^2\,g^{-1}$)	Total pore volume ($cm^3\,g^{-1}$)	BJH pore diameter (nm)	FE-SEM average MZNs diameter (nm)
Z06	NaF	150	0.26	6.4 ± 2.0	290 ± 20
Z01	NaCl	240	0.23	3.4 ± 1.7	450 ± 20
Z07	NaBr	130	0.20	6.1 ± 2.4	670 ± 20
Z08	NaI	130	0.23	6.6 ± 1.9	630 ± 40

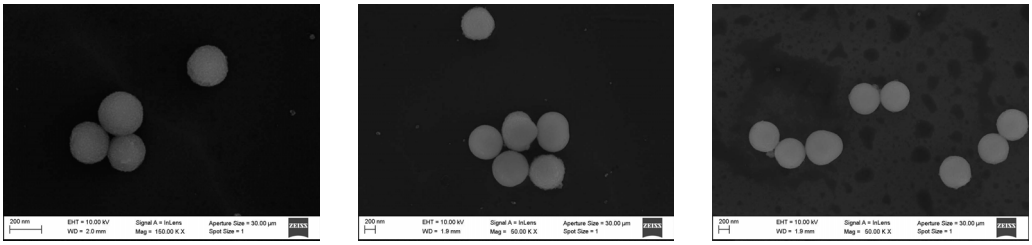

a. NaF (Z07) **b.** NaBr (Z08) **c.** NaI (Z09)

Figure 3.48: FE-SEM images of sodium halides MZNs series.

regular shape and controlled size, as also reported in literature [99]. The principal role of the salt is the surface stabilization of the MZNs. As known, alkali halides dissolve completely in water as alkali cation (M^+) and halogen anion (X^-). These ions create an Electrical Double Layer (EDL) on the surface of the particles, which are electrostatically stabilized avoiding their coalescence. As reported in Table 3.19, the salts have different solubility in water, which is ascribed to the ionic pair. These ions could be organized into two groups based on its aqueous affinity and hydration capacity. The more hydrated smaller ions (Li^+, Na^+ and F^-) are known as *kosmotropes* (k), because they tend to organize the water molecules. They are also known as *water structure maker* because of they reduce the water molecules mobility around them. The larger ions (K^+, Rb^+, Cs^+, Cl^-, Br^- and I^-) have the opposite character, so they are known as *chaotropes* (c) and *water structure breaker* [185, 186]. It is evident that four type of couples are possible (as evidence in Table 3.19): k^+k^-, c^+c^-, c^+k^- and k^+c^-. The different size and water affinity of the single ions influence the salts solubility. In particular, similar-size ions couples are less soluble as visible in Table 3.19 [185].

Observing the MZNs size trend with the salt used (Figure 3.49), a similar path between particles size and salt solubility is detectable. Despite the literature [105, 108, 109, 181], which reported a correlation among the size and the shape of the particles with the ionic strength of the salts, these results show an evident relation among the size and the alkali halides solubility. The MZNs diameter increases

Table 3.19: Molar solubility in water of alkali halides. Ionic radii in angstrom (Å) have been reported in brackets. The four type of couple (k^+k^-:blue, c^+c^-:red, c^+k^-:purple and k^+c^-:violet) have been evidenced.

MX	F^- (1.33)	Cl^- (1.81)	Br^- (1.96)	I^- (2.20)
Li^+ (0.74)	0.1	19.6	20.4	8.8
Na^+ (1.02)	1.0	6.2	8.8	11.9
K^+ (1.38)	15.9	4.8	7.6	8.7
Rb^+ (1.49)	12.5	7.5	6.7	7.2
Cs^+ (1.70)	24.2	11.0	5.1	3.0

when a more soluble salt is used, meanwhile a lower solubility seems to promote the formation of more particles nuclei, and a smaller final size. In particular less soluble is the salt and smaller is the diameter. Assuming that in less soluble salts the ion pairs are more bound, because the ion-ion interactions are stronger than ion-water ones, a lower amount of water is necessary to dissolve the salt itself. The remaining free water molecules are involved in the formation of particles germination nuclei. So, at constant precursor quantity, more particles are formed with smaller dimension. However, the EDL is thinner thanks to the stronger interaction cation-anion, allowing a good particle separation. These assumptions can be reasonable remembering that small and controlled amount of water is present in the synthesis solution. It is considered as a reagent rather than as a solvent.

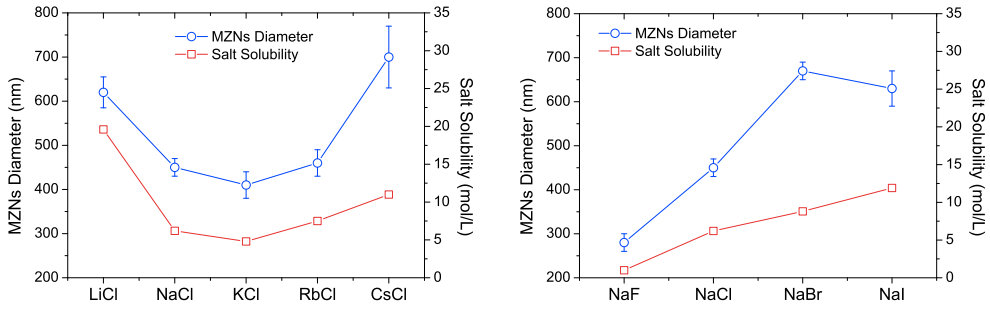

a. Alkali chlorides (MCl) series **b.** Sodium halides (NaX) series

Figure 3.49: Mean MZNs diameter course and alkali halides solubility.

Secondly, the type of couple should be considered. The smaller MZNs with NaF, the less soluble k^+k^- salt, are achieved. Both the ions are water structure maker and bind a little amount of molecules. The bigger particles with CsCl, well soluble and c^+c^- salt, are achieved because of a large amount of water is necessary for solubilize the ions. For a mixed couple (c^+k^- and k^+c^-), the dominant contribution should be considered. For example, LiCl is more soluble and the particles size is big enough. As reported in Figure 3.50, Cl^- have a mild chaotropic effect respect to the strong

kosmotropic effect of Li^+ [185]. In this figure the water mobility changes, caused by the ions presence, have been visualized in terms of entropy variation (ΔS), calculated from thermodynamic data. The entropy change has been plotted as a function of the ionic radius and the values where $\Delta S = 0$ (1.06 Å for cation and 1.78 Å for anion) defines the ionic sizes that do not change the entropy of the neighboring water molecules. The particles achieved with the sodium halides, except for NaCl, have larger pore size. Taking in account the Figure 3.50, both Na^+ and Cl^- do not affect very much the entropy of the water molecules. Really, they are near the horizontal axis, *i.e.* where entropy is zero. The anion influences more the neighborhood water mobility. Alkyl amines are bases, which in water forms ammonium cation, while halides act as its counterions. A modification of the micelle size could be reached because of the interaction among anion, water and amine. The bigger chaotropes anions, Br^- and I^-, have a steric hindrance that could enlarge the distance between the ammonium heads. The smaller F^-, instead has a great kosmotropic effect on the water molecules causing a similar hindrance among the surfactant heads.

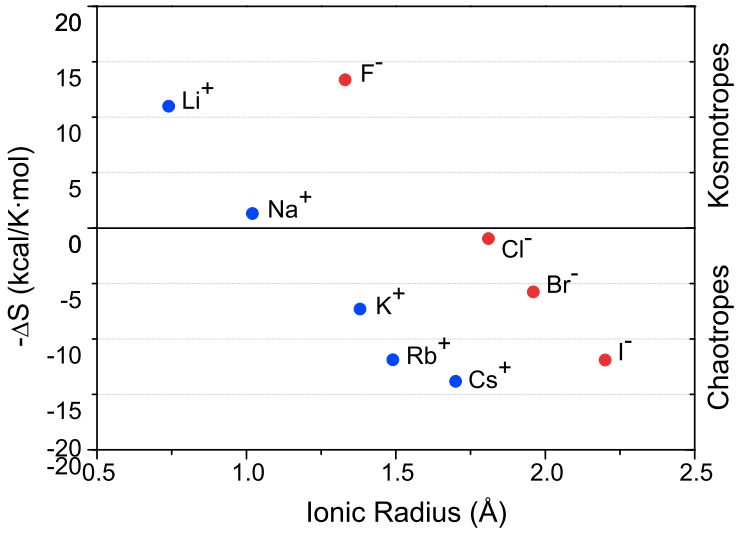

Figure 3.50: The entropy of water near an ion minus the entropy of pure water.

Another important variable is the NaCl quantity present in the solution. The data of these samples have been reported in Table 3.20 and Figure 3.51. The number of ions present in solution has a great importance in order to stabilize the micelles and the particles size. Different ionic concentration means different *ionic strength*[14]. The

[14]The ionic strength μ of a solution is determined by the equation

$$\mu = \frac{1}{2}\sum_{i=1}^{N} c_i z_i^2 \tag{3.22}$$

where c_i is the molar concentration and z_i is the charge of the i-th ion specie.

ionic strength depends to the concentration and the charge of the ions in solution. The alkali halides are formed by monovalent ions and, in all the previous samples, the molarity is constant, so particles size does not depend by this parameter. But, when the amount of the same salt is reduced, the mean diameter increases, as visible in Figure 3.51. Actually, lower is the ionic strength larger is the size, this is probably due to the greater number of water molecules bind into the EDL, which is thicker. When the ion concentration is too high, not homogenous growth is possible, as already reported in literature [109].

Table 3.20: Summary of MZNs with different amount of NaCl 0.1 M samples properties derived from nitrogen isotherms and FE-SEM measurements. The volume ratio has been considered respect to the best ratio (1:1).

Label	ZP:NaCl ratio	BET surface area ($m^2\,g^{-1}$)	Total pore volume ($cm^3\,g^{-1}$)	BJH pore diameter (nm)	FE-SEM average MZNs diameter (nm)
Z10	2:1	110	0.18	6.4 ± 4.1	590 ± 50
Z01	1:1	240	0.23	3.4 ± 1.7	450 ± 20
Z11	1:2	190	0.25	4.9 ± 3.9	n.a.

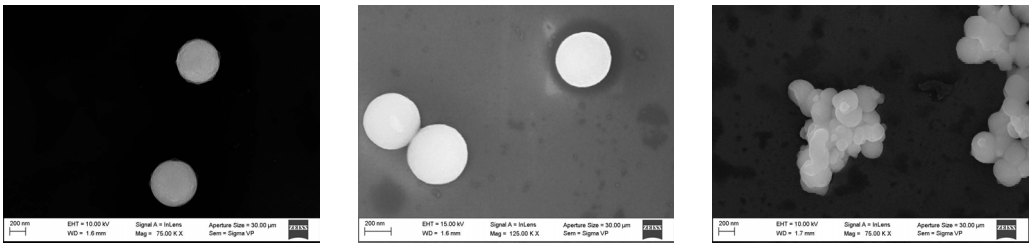

a. 2:1 (Z10) **b.** 1:1 (Z01) **c.** 1:2 (Z11)

Figure 3.51: FE-SEM images of MZNs with different volume ratio ZP:NaCl (0.1 M).

Water amount has also been changed, the relative data of these samples have been reported in Table 3.21 and Figure 3.52. Water has several role in the synthesis: a) creates nucleation germs, b) it is necessary for hydrolysis reaction and c) solubilize the alkali halides salts. A low amount of water, determines a slowing down of the kinetic reaction, increasing the induction time. Moreover larger MZNs grow as demonstrate in the synthesis of sample Z12, where no extra amount of water is added. In this case a mean diameter of 850 nm is obtained, and 800 nm when half amount of water is added. With double water amount, actually, heterogeneous particles rise because of the hydrolysis kinetic is too fast for a controlled growth. The materials are also microporous because of a different micelle conformation. The lower limit of the BJH method is about 1.7 nm, so the data of these samples are not very reliable.

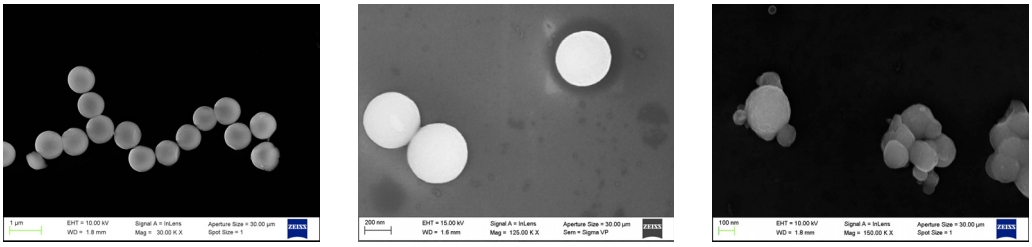

a. 2:1 (Z13) **b.** 1:1 (Z01) **c.** 1:2 (Z14)

Figure 3.52: FE-SEM images of MZNs with different volume ratio ZP:H_2O.

Table 3.21: Summary of MZNs with different amount of water samples properties derived from nitrogen isotherms and FE-SEM measurements. The volume ratio has been considered respect to the best ratio (1:1).

Label	ZP:H_2O ratio	BET surface area ($m^2\,g^{-1}$)	Total pore volume ($cm^3\,g^{-1}$)	BJH pore diameter (nm)	FE-SEM average MZNs diameter (nm)
Z12	1:0	290	0.17	$2.0 \pm 1.9^*$	850 ± 40
Z13	2:1	300	0.17	$1.8 \pm 1.5^*$	800 ± 60
Z01	1:1	240	0.23	3.4 ± 1.7	450 ± 20
Z14	1:2	350	0.22	$2.0 \pm 1.9^*$	n.a.

A different amine surfactant (octadecylamine) has also been tested in order to verify its role on the pore dimension. As reported in Table 3.22 and in Figure 3.53, the use of this surfactant produces a larger pore size with a narrow distribution of the diameter. Differently from the previous case, the pore swelling effect is caused by the longer alkyl chain of the amine. Longer the hydrophobic chain, bigger the micelle diameter. Larger pore size means also a reduced surface area. Finally, the MZNs diameter is also higher.

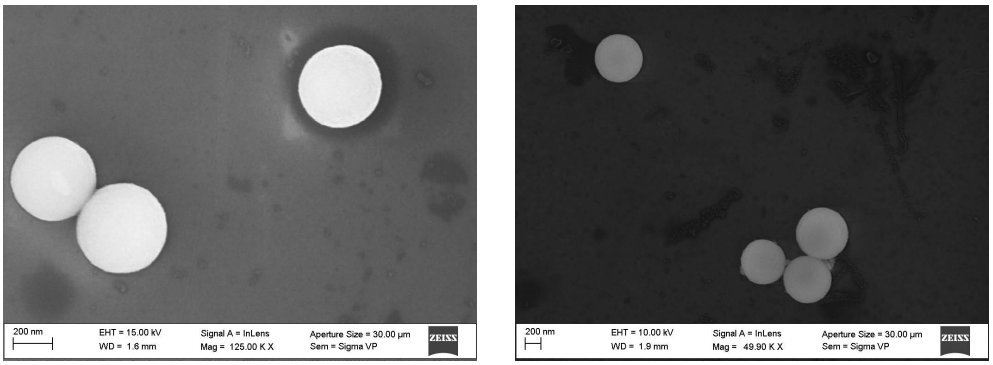

a. HDA (Z01) **b.** ODA (Z09)

Figure 3.53: FE-SEM images of surfactant MZNs series.

Table 3.22: Summary of MZNs with different surfactant samples properties derived from nitrogen isotherms and FE-SEM measurements.

Label	Amine	BET surface area ($m^2\,g^{-1}$)	Total pore volume ($cm^3\,g^{-1}$)	BJH pore diameter (nm)	FE-SEM average MZNs diameter (nm)
Z01	HDA	240	0.23	3.4 ± 1.7	450 ± 20
Z09	ODA	140	0.24	6.5 ± 1.8	620 ± 50

3.5.2 Biological tests

Cytototoxicy

Until now, the possible theranostic use of MZNs must be evaluated and no study about their application as biocompatible delivery system has been reported. To evaluate if the new synthesized MZNs could be a promised nanomaterial in medicine, the MZNs biocompatibility in two cancer cell lines has been tested. The Hela cells, which represent an established model for subcellular localization studies, and the MDA-MB-231 cells, which is an aggressive breast cancer cell line used both for *in vitro* and *in vivo* studies, have been chosen to test the new Drug Delivery System (DDS) loaded with doxorubicin (DOX) efficiency. Z06 sample has been chosen as the more suitable MZNs for DDS, because of its smaller size. The results about the cells treated for 96 hours at different concentration have been reported in Figure 3.54.

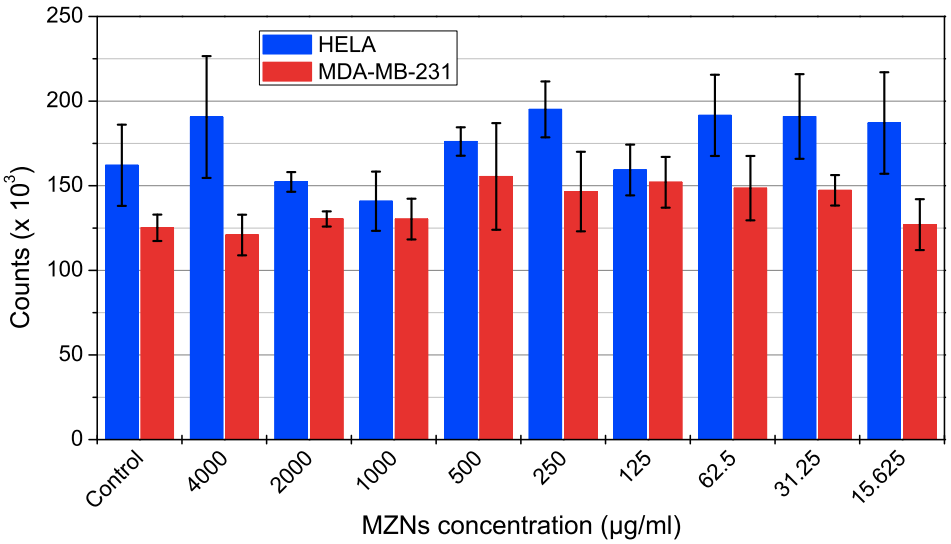

Figure 3.54: *In vitro* cell viability assay. No significant differences between MZNs treated and untreated cells have been found, even at the higher concentration tested.

As shown in Figure 3.54, the MZNs are not toxic up to $4\,mg\,ml^{-1}$ in both the tested cell lines. Comparing separately the counts of the two different cell lines, no significant differences between the treated and untreated (Control columns) samples

is found within the experimental errors.

In order to demonstrate that the NPs capacity to cross the plasma membrane, the cell internalization assay has been conducted. Cells are treated for 2 hours with fluorescent dye loaded MZNs (see Subsection 2.2.2 on page 26). Confocal microscopy analysis, proposed in Figure 3.55, show that MZNs are distributed inside the cytoplasm (red marked) but are excluded from the nucleus (green marked), as can be verified for other DDS [187].

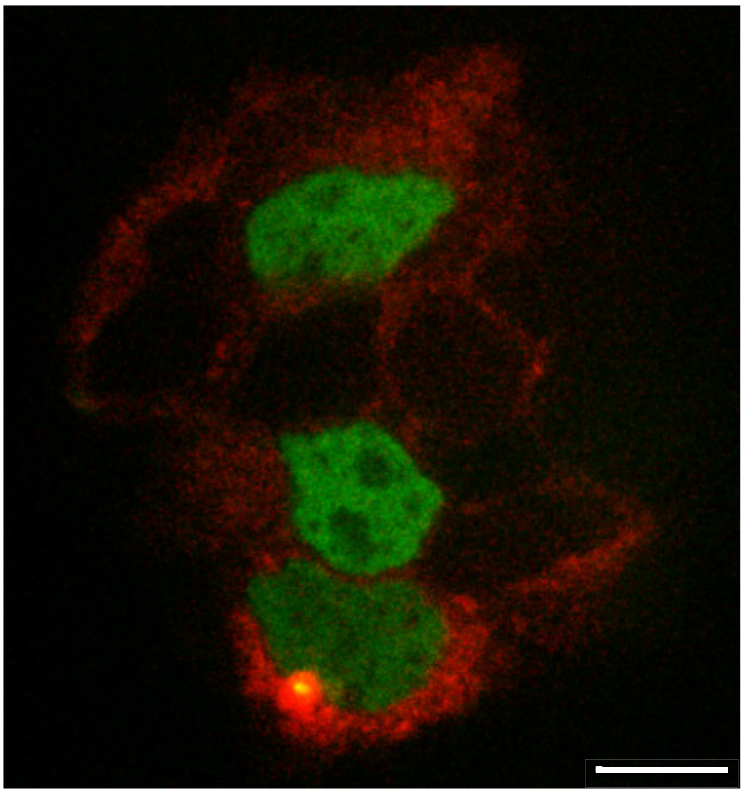

Figure 3.55: Confocal microscope image of MDA-MB-231 cells treated for 2 hours with MZNs (Z06). Scale bar 10 µm.

In vivo biodistribution

As possible new inorganic carrier, MZNs have been characterized *in vivo* in mice. Fluorescent MZNs have been injected intravenously in two mice and the relative biodistribution has been imaged using an IVIS instrument (Figure 3.56). *In vivo* biodistribution experiment is a proof of concept aimed to assess how MZNs behaved once injected. Due to ethical reasons, and since preliminary results have been comparable with existing literature on silica nanoparticles, no further mice have been sacrificed.

In Figure 3.56, the images of the mice different organs have been reported sep-

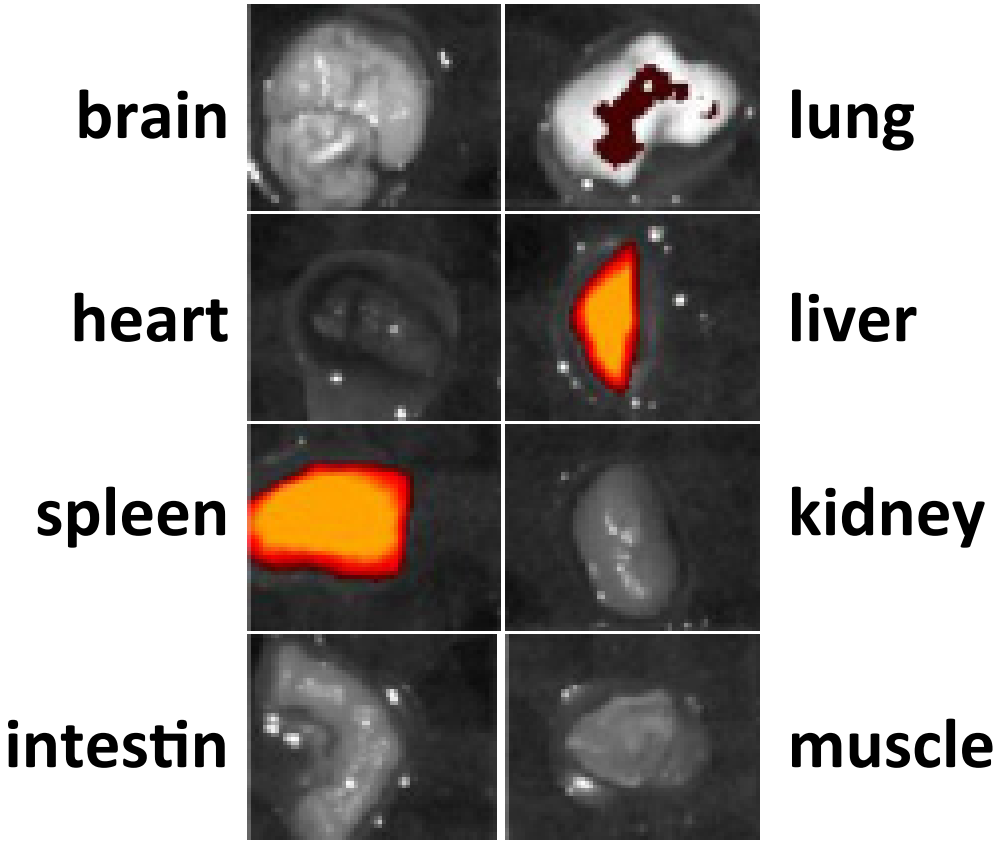

Figure 3.56: *In vivo* biodistribution of MZNs in mice organs. Fluorescence intensity: red (low intensity) yellow (high intensity).

arately. The fluorescence intensity increases from red to yellow. As clearly visible, the MZNs are accumulated principally in the liver and spleen and barely evident in the lungs. A similar behavior in other DDS with analogous size is verified in literature [188]. Another important aspect is the long period observation of the mice, it is worth noting that one month after the injection they do not show any visible signs of toxicity.

Biodegradation

The previous experimental evidences underline that the MZNs are not cytotoxic. A biodegradation test in order to estimate if the MZNs could be degraded when laid for long time into biological fluids has been conducted.

In Figure 3.57 a statistical estimation of the MZNs (Z06) diameter reduction during the test has been proposed. The error bars show the 95% confidence interval of the mean diameter[15].

[15]The range of values around the mean value that will in theory include the population statistic for roughly 95% of all samples drawn.

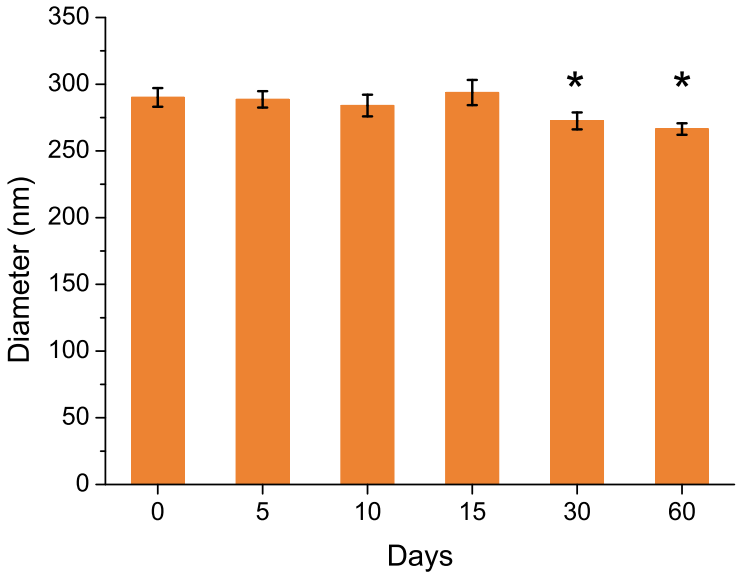

Figure 3.57: MZNs mean diameters estimation during the biodegradation test at different incubation time.

As reported in Figure 3.57, MZNs are stable during the first two weeks of incubation, no statistically significant decrement of the diameter is appreciable from the first column (0 days) until the forth one (15 days). Significant differences (the data marked with $*$), can be measured over one month of incubation. For the last two data, a p-value less than one percent ($p < 0.01$) is found, *i.e.* there is a very low probability that the diameter value (both at 30 and 60 days) is casually different from the initial value. Finally, after two months, an estimation of the diameter reduction more than 7.0%, roughly corresponding to 22% of total volume, is obtained. These data show, once again, the suitability of this zirconia system both for *in vitro* and *in vivo* studies aiming to the development of a possible nanomedicine carrier. Even if the degradation time is longer than the typical data reported for MSNs carrier, some advantages for specific applications, such as bone-directed drug delivery, could be obtained.

Drug loading and release

In order to analyze the MZNs ability to load therapeutic molecules, such as drugs, doxorubicin (DOX) as a probe to test their loading capacity and efficiency has been used. A comparison between other silica carrier examples, which load the same drug, has been proposed in Table 3.23.

Results reported in Table 3.23, show that MZNs can take up to 9.0% of their weight in DOX. This value is a little bit lower than the loading efficiencies found in analogous MSNs systems. This is only due to the intrinsic chemical-physical proper-

Table 3.23: Physical properties and DOX loading efficiencies of different inorganic carrier.

Sample	NP size (nm)	Surface area ($m^2\,g^{-1}$)	Total pore volume ($cm^3\,g^{-1}$)	Pore size (nm)	Loading efficiency (%)	Ref.
MSN	100	751	0.42	2.2	10.0	[189]
mMSN[a]	100	495	0.44	2.4	5.8	[190]
MSN-NH_2	105	390	0.90	2.7	34.0	[191]
hMSN[b]	120	962	1.07	2.7	18.4	[192]
MSN	360	n.a.	0.15	n.a.	21.2	[193]
MZN (Z06)	290	153	0.26	6.4	9.0	[112]

[a] surface modified nanoparticles
[b] hollow MSNs

ties of zirconia, which ensure that the resulting MZNs have a lower pore volume and specific superficial area compared to MSNs. The drug loading efficiency has been calculated with the equation (2.1) at page 27. The relatively high loading capacity of MZNs is probably due to the large pores, which allow an easy encapsulation of the DOX into the NPs. Drug loading leans on different morphological elements, such as surface area, total pore volume and surface charge, and depends by different mechanisms (hydrogen bonding, ionic interactions and dipole interactions) [194]. If the inner pore volume is accessible by the drug, usually the surface area is one of the most important parameters, since guest molecules can be trapped and interact with the carrier [195]. MZNs have a lower surface area compared to the MSNs counterparts, so a lower loading capacity is intrinsically obtained. Moreover, zirconia bulk density ($5.8\,g\,cm^{-3}$) is almost double than silica ($2.2\,g\,cm^{-3}$). If the geometrical shape of the particles is the same, for an equal weight of particles, MZNs will have roughly the half of the available surface. Hence the intrinsic physical properties of the zirconia system give a lower pore volume and a specific superficial area compared to silica one.

The as loaded MZNs have also been tested for drug release process. In Table 3.24 the drug release after 24 h at different pH values has been reported.

Table 3.24: Doxorubicin release at different pHs after 24 h.

pH	DOX released (%)
4.0	7.8 ± 3.7
5.5	13.3 ± 3.1
7.0	16.2 ± 2.9
8.5	27.1 ± 0.7

Preliminary tests, carry out at different pHs, show a good retention till pH 4.0, while drug is released at higher pHs, as reported in Table 3.24. This behavior is quite different from the data usually reported in literature about MSNs system, which

exhibit little or absent release at neutral pH and a good release in acid environments [191]. Therefore MZNs could be considered a valid alternative as drug delivery carrier in those situations where MSNs are lesser efficient or show a low release. Therefore MZNs could be considered a valid drug delivery carrier in all the situations where the zirconia specific properties are required. For example, considering the well-established availability of bulk zirconia in bone implants or in porous scaffolds for bone tissue engineering, MZNs could be chosen as good candidate for bone-directed drug delivery. Moreover, their confirmed stability could be useful in the long-term release applications.

Chapter 4

Conclusions

4.1 Project final remarks

The present thesis investigated some aspect of the wide research field of the zirconia-based materials. The project has been divided into two parts that analyze different features of the zirconia engineering materials and their possible structural and functional applications.

The study of the zirconia polymorphism has been divided into three sections depending on the chosen aliovalent doping cations (Y^{3+}, Eu^{3+} and Ta^{5+}). From the hydroxide co-precipitation process five series of zirconia doped and co-doped samples have been prepared, named ZY, ZYE, ZE, ZYET and ZT (Z: Zirconium, Y: Yttrium, E: Europium and T: Tantalum).

The first section dealt with the analysis of the well-known zirconia Y-doped system using the Cathodoluminescence (CL) technique. From the data, a clear correlation between the CL spectra morphology and the quantitative XRPD analyses has been obtained. A phenomenological equation has been written for the quantitative estimation of the zirconia phases. Another central point has been the role of not-stoichiometric oxygen in the zirconia physicochemical behavior. Since the compound electroneutrality must be preserved, two oxygen vacancies should be formed every Y^{3+} cation. The CL intensity has been correlated to the Y^{3+} content: higher the second, smaller the first. Indeed, the intrinsic vacancies are the most efficient defects and the presence of dopant fell down the CL intensity, progressively. The overall intensity has been correlated to the annihilation of the intrinsic vacancies rather than to the increment of vacancies related to the dopant.

In the second section, in two series (ZE and ZYE) of zirconia stabilized with trivalent cations (Y^{3+} and Eu^{3+}), has been analyzed the tetragonal-to-monoclinic transition ($t \rightarrow m$) with Photoluminescence (PL) technique, and compared with the Rietveld refinements results. The validity of a fast and easy investigation of the

martensitic transformation in zirconia ceramics, *via* luminescence method, has been demonstrated. The metastable tetragonal phase is destabilized progressively by external uniaxial stress, which has induced the $t \rightarrow m$ transition. A clear correlation between XRPD quantitative analyses and PL spectra has been found and the monoclinic content has been monitored by the emission spectrum of Eu-doped zirconia. The ratio between the area of the Electric Dipole and the Magnetic Dipole transitions, gave a first qualitative information about the monoclinic content. Furthermore, a quantitative evaluation has been determined thanks to a linear combination of two pure phases reference spectra (one for monoclinic and one for tetragonal) used for the fit of the experimental spectrum. The more precise quantitative data obtained by the Rietveld refinement, has been compared with the easier and faster luminescence results. As expected, a linear correlation between the monoclinic content and the ratio between the integrated area of the $^7F_2$ Eu^{3+} transition (613 nm) and the total intensity of the hypersensitive transition (600-620 nm) has been found. This good results can open the possibility to monitoring *in situ* the degradation degree of zirconia stabilized materials (*e.g.* in great mechanical components), avoiding to disassemble the pieces and overcoming the difficulties of analyzing them into scientific laboratories with XRD or Raman spectroscopy techniques. Obviously, the presence of a little amount of europium into the materials would be mandatory for the use of this innovative forensic analysis. Another advantage would be the restricted range of spectrum necessary for the test, *e.g.* with an appropriate band-pass optical filter.

In the third section, the oxygen vacancies annihilation inside the zirconia tetragonal stabilized materials has been investigated. If trivalent cations (Y(III) and Eu(III)) introduced oxygen vacancies in order to preserve the electroneutrality, the presence of pentavalent cations (Ta(V)) should drive to the opposite effect. A charge compensation has been obtained in a co-doped samples (ZYET series). As expected, a progressive destabilization of the metastable tetragonal phase is achieved increasing the tantalum content. Unlike the previous case, where the external stress induced the $t \rightarrow m$ transition, here the reduction of the oxygen vacancies produced a less-stabilized tetragonal zirconia. In particular, at high Ta content, the study evidenced the formation of an unexpected crystalline phase, tetragonal, or of quite similar structure. This novelty focused the attention on the study of single Ta-doped zirconia materials in order to understand the pentavalent cation role into the lattice.

A zirconia Ta-doped powders (ZT series) have been prepared in order to understand the pentavalent cation behavior into the zirconia lattice. A systematic study of the XRPD patterns has been performed, supported also by a computational method. Two approaches have been adopted: the first approach considered simply the use of the Rietveld analysis, while the second one utilized the more complex direct

space method followed by a Rietveld analysis. Both of them found almost identical structures. By the first method an orthorhombic cell ($Pca2_1$), already reported in literature for other zirconia compositions has been found. A distorted monoclinic cell ($C2/c$) with the parameters almost identical to the above-mentioned orthorhombic cell have been determined with the second method. From a crystallographic analysis of the parameters and the atomic positions, the two cells almost totally overlap. Since the XRPD analysis does not distinguish between the two structures and to avoid any ambiguity it has been decided to christen this new phase as PN phase. The three most significant samples ZT3, ZT5 and ZT8, have been investigated also by *in situ* synchrotron radiation XRPD measurements, from 100 °C to 1000 °C and during the subsequent cooling, in order to follow the thermal evolution of the crystalline phases. The presence of the PN phase, have been confirmed as stable polymorph until 1000 °C. From the Rietveld refinement of the patterns, a first estimation of the Coefficient of Thermal Expansion (CTE) of the PN phase has also been possible. An average value of CTE higher than the monoclinic zirconia has been found, so it should be possible use as Thermal Barrier Coating (TBC) application. A Raman study has also been performed for all the samples in order to strength the XRPD results, confirming that an uncommon zirconia structure has been isolated.

Finally, the most interesting ZT samples have been used for the production of full-dense sintered materials *via* Spark Plasma Sintering (SPS) technique. In order to achieve higher density it has been used an the operating temperature higher than 1000 °C, and two series at 1150 °C (SPS1150) and 1250 °C (SPS1250) have been prepared. From the WAXS patterns of the bulk specimens shown a different phase composition respect to the calcined powders. Generally, the doping amount was too low for a complete single-phase stabilization. The polished and annealed surfaces of the specimens have been investigated by FE-SEM, with BSE and SE mode, in order to evidence the composition and the grain structure of the specimens. A double phase composition, strong correlated to the grains structure has been verified. From the EDS analyses, very interesting results have been obtained. In particular it has been possible to verify that the two phases had a constant composition, one poor in tantalum and the other with a fixed content around ~16 mol% of Ta related to the PN phase. Mechanical tests have also been performed on some SPS specimens. An interesting behavior of the elastic modulus has been found, supporting the already reported data on the PN phase composition and the mechanical performance.

The second part of the project proposed a facile and versatile method for the production of Mesoporous Zirconia Nanoparticle (MZN). Different techniques and approaches had been tested to obtain the final process presented in the thesis. The template sol-gel synthesis with neutral surfactant produced a mesoporous network materials, while the alkali halides acted as size and shape controller. A hydrothermal

step has also been chosen to obtain spherical zirconia NPs. The purification process with a vacuum extraction instead of calcination step has been chosen to avoid the loss of specific area, caused by the crystallization. All the main parameters have been investigated and a particular correlation between the salts solubility and the average particle sizes has been found. Thanks to the good results, has been investigated a possible use as versatile and theranostic nanosystem for diseases effective treatment. Biological tests, such as biocompatibility, biodistribution and biodegradation of the system have been tested. The MZNs resulted not cytotoxic and shown a long-period degradation. Thanks to the high surface area, the drug loading and the successive release of doxorubicin have been explored with interesting results. The release at different pH shown a good profile release in basic environments. All the results shown as these NPs could be used as inorganic carrier interesting alternative to silica systems.

4.2 Future perspectives

The global study of the aliovalent cations doped zirconia polymorphs is far from being exhaustive. Literature is still full of open questions and quite incomplete works. The thesis results, although encouraging, evidenced some of the future theoretical and technological problems to solve. The Ta-doped zirconia system has been the most interesting among those studied. The possibility to stabilize a new phase with a specific composition (~16mol% Ta) must to be verified and the space group identified. The computational simulations of crystal structure and Raman modes, starting from the first-principles, should be useful instruments. A complete and deeper investigation of the mechanical properties, also for a single-phase specimen, should be performed in order to verify the real possible engineering development of the materials.

The already published (10^{th} August 2015) MZNs process, are currently under patent pending evaluation (patent request number PD2015A000015) since 28^{th} January 2015. The next step to improve the loading efficiency consists into the modification of the chemical properties of MZNs surface, adding functional groups such as $-NH_2$, −COOH or −SH. The zirconium chemistry is different from the silicon one and, at the moment, no suitable precursors are available. Preliminary studies with modified silanes (APTES, CEST) seem to functionalize the zirconia surface, but the mechanism of grafting is still under investigation. The final and far goal concerns the investigation of the adaptability of MZNs to other drugs or imaging agents in order to realize a real personalized therapy. In addition, the physical and chemical properties improvement has to be considered as the starting point for the creation of a smart, easy and cheap theranostic nanosystem platform.

Bibliography

[1] B. Basu and K. Balani. *Advanced Structural Ceramics*. Ed. by The American Ceramic Society. Wiley, 2011. ISBN: 978-0-470-49711-1.

[2] R.B. Heimann. *Classic and Advanced Ceramics: From Fundamentals to Applications*. Wiley-VCH, 2010. ISBN: 978-3-527-32517-7.

[3] A. Benedetti, G. Fagherazzi, and F. Pinna. "Preparation and structural characterization of ultrafine zirconia powders". In: *Journal of the American Ceramic Society* 72 (1989), pp. 467–469. DOI: 10.1111/j.1151-2916.1989.tb06154.x.

[4] A. Benedetti et al. "Structural properties of ultra-fine zirconia powders obtained by precipitation methods". In: *Journal of Materials Science* 25 (1990), pp. 1473–1478. DOI: 10.1007/BF00585468.

[5] I. Freris et al. "Synthesis and optical properties of sub-micron sized rare earth-doped zirconia particles". In: *Optical Materials* 33 (2011), pp. 1745–1752. DOI: 10.1016/j.optmat.2011.06.010.

[6] R. Marin et al. "Monitoring the t→m Martensitic Phase Transformation by Photoluminescence Emission in Eu^{3+}-Doped Zirconia Powders". In: *Journal of the American Ceramic Society* 96 (2013), pp. 2628–2635. DOI: 10.1111/jace.12363.

[7] M. Boffelli et al. "Oxygen Hole States in Zirconia Lattices: Quantitative Aspects of Their Cathodoluminescence Emission". In: *The Journal of Physical Chemistry A* 118 (2014), pp. 9828–9836. DOI: 10.1021/jp506923p.

[8] F. Asaro et al. "Evolution of the nonionic inverse microemulsion-acid-TEOS system during the synthesis of nanosized silica via the sol-gel process." In: *Langmuir : the ACS journal of surfaces and colloids* 26 (2010), pp. 12917–12925. DOI: 10.1021/la101737x.

[9] F. Enrichi et al. "Investigation of luminescent dye-doped or rare-earth-doped monodisperse silica nanospheres for DNA microarray labelling". In: *Optical Materials* 32 (2010), pp. 1652–1658. DOI: 10.1016/j.optmat.2010.04.026.

[10] I. Freris et al. "Encapsulation of submicrometer-sized silica particles by a thin shell of poly(methyl methacrylate)." In: *Journal of Colloid and Interface Science* 331 (2009), pp. 351–355. DOI: 10.1016/j.jcis.2008.11.052.

[11] A. Parma et al. "Structural and photoluminescence properties of ZrO_2:Eu^{3+}@SiO_2 nanophosphors as a function of annealing temperature". In: *Journal of Luminescence* 130 (2010), pp. 2429–2436. DOI: 10.1016/j.jlumin.2010.08.007.

[12] S. Sivestrini et al. "Structural and luminescence properties of europium(III)-doped zirconium carbonates and silica-supported Eu^{3+}-doped zirconium carbonate nanoparticles". In: *Journal of Nanoparticle Research* 12 (2009), pp. 993–1002. DOI: 10.1007/s11051-009-9655-5.

[13] G. Sponchia et al. "Mesoporous silica nanoparticles with tunable pore size for tailored gold nanoparticles". In: *Journal of Nanoparticle Research* 16 (2014), p. 2245. DOI: 10.1007/s11051-014-2245-1.

[14] X. Wang et al. "Mesoporous titanium zirconium oxide nanospheres with potential for drug delivery applications." In: *ACS Applied Materials & Interfaces* 5 (2013). DOI: 10.1021/am4031104.

[15] J. Xie, S. Lee, and X. Chen. "Nanoparticle-based theranostic agents". In: *Advanced Drug Delivery Reviews* 62 (2010), pp. 1064–1079. DOI: 10.1016/j.addr.2010.07.009.

[16] M.S. Muthu et al. "Nanotheranostics - application and further development of nanomedicine strategies for advanced theranostics". In: *Theranostics* 4 (2014), pp. 660–677. DOI: 10.7150/thno.8698.

[17] P.D.L. Mercera et al. "Influence of ethanol washing of the hydrous precursor on the textural and structural properties of zirconia". In: *Journal of Materials Science* 27 (1992), pp. 4890–4898. DOI: 10.1007/BF01105251.

[18] P.C. Guess, W. Att, and J.R. Strub. "Zirconia in Fixed Implant Prosthodontics". In: *Clinical Implant Dentistry and Related Research* 14 (2012), pp. 633–645. DOI: 10.1111/j.1708-8208.2010.00317.x.

[19] T. Archer, C.D. Pemmaraju, and S. Sanvito. "Magnetic properties of ZrO_2-diluted magnetic semiconductors". In: *Journal of Magnetism and Magnetic Materials* 316 (2007), e188–e190. DOI: 10.1016/j.jmmm.2007.02.085.

[20] H. Kondo et al. "Mechanical and Magnetic Properties of Novel Yttria-Stabilized Tetragonal Zirconia/Ni Nanocomposite Prepared by the Modified Internal Reduction Method". In: *Journal of the American Ceramic Society* 88 (2005), pp. 1468–1473. DOI: 10.1111/j.1551-2916.2005.00243.x.

[21] Yan Cong et al. "Synthesis and Optical Property Studies of Nanocrystalline ZrO_2:Ti Long-Lasting Phosphors". In: *Journal of The Electrochemical Society* 155 (2008), K195. DOI: 10.1149/1.2971023.

[22] S. Tang et al. "Hollow Mesoporous Zirconia Nanocapsules for Drug Delivery". In: *Advanced Functional Materials* 20 (2010), pp. 2442–2447. DOI: 10.1002/adfm.201000647.

[23] A. Patra et al. "Upconversion in Er^{3+}: ZrO_2 Nanocrystals". In: *The Journal of Physical Chemistry B* 106 (2002), pp. 1909–1912. DOI: 10.1021/jp013576z.

[24] C. Piconi and G. Maccauro. "Zirconia as a ceramic biomaterial". In: *Biomaterials* 20 (1999), pp. 1–25. DOI: 10.1016/S0142-9612(98)00010-6.

[25] Patrick M. Kelly and L. R Francis Rose. "The martensitic transformation in ceramics - Its role in transformation toughening". In: *Progress in Materials Science* 47 (2002), pp. 463–557. DOI: 10.1016/S0079-6425(00)00005-0.

[26] D.G. Lamas and N.E. Walsöe de Reca. "Oxygen ion displacement in compositionally homogeneous, nanocrystalline ZrO_2-12mol% Y_2O_3 powders". In: *Materials Letters* 41 (1999), pp. 204–208. DOI: 10.1016/S0167-577X(99)00131-7.

[27] R.C. Garvie, R.H. Hannink, and R.T. Pascoe. "Ceramic steel?" In: *Nature* 258 (1975), pp. 703–704. DOI: 10.1038/258703a0.

[28] J. Gao, Y. He, and W. Gao. "Fiber-reinforced Yttria Partially Stabilized Zirconia Thermal Barrier Coatings Processed by Sol-gel Method". In: *High Temperature Materials and Processes* 30 (2011), pp. 289–296. DOI: 10.1515/HTMP.2011.047.

[29] J.R. Kelly and I. Denry. "Stabilized zirconia as a structural ceramic: an overview." In: *Dental Materials* 24 (2008), pp. 289–298. DOI: 10.1016/j.dental.2007.05.005.

[30] E. Tsalouchou et al. "Fatigue and fracture properties of yttria partially stabilized zirconia crown systems." In: *Dental Materials* 24 (2008), pp. 308–18. DOI: 10.1016/j.dental.2007.05.011.

[31] T. Chartier, D. Merle, and J.L. Besson. "Laminar ceramic composites". In: *Journal of the European Ceramic Society* 15 (1995), pp. 101–107. DOI: 10.1016/0955-2219(95)93055-8.

[32] J. Chevalier et al. "The Tetragonal-Monoclinic Transformation in Zirconia: Lessons Learned and Future Trends". In: *Journal of the American Ceramic Society* 92 (2009), pp. 1901–1920. DOI: 10.1111/j.1551-2916.2009.03278.x.

[33] J.P. Goff et al. "Defect structure of yttria-stabilized zirconia and its influence on the ionic conductivity at elevated temperatures". In: *Physical Review B* 59 (1999), pp. 14202–14219. DOI: 10.1103/PhysRevB.59.14202.

[34] J.H. Lee. "Review on zirconia air-fuel ratio sensors for automotive applications". In: *Journal of Materials Science* 38 (2003), pp. 4247–4257. DOI: 10.1023/A:1026366628297.

[35] G. Lu, N. Miura, and N. Yamazoe. "High-temperature hydrogen sensor based on stabilized zirconia and a metal oxide electrode". In: *Sensors and Actuators B* 35-36 (1996), pp. 130–135. DOI: 10.1016/S0925-4005(97)80042-1.

[36] A. Tsoga et al. "Gadolinia-doped ceria and yttria stabilized zirconia interfaces: regarding their application for SOFC technology". In: *Acta Materialia* 48 (2000), pp. 4709–4714. DOI: 10.1016/S1359-6454(00)00261-5.

[37] K. Wincewicz and J. Cooper. "Taxonomies of SOFC material and manufacturing alternatives". In: *Journal of Power Sources* 140 (2005), pp. 280–296. DOI: 10.1016/j.jpowsour.2004.08.032.

[38] P.D.L. Mercera et al. "Stabilized tetragonal zirconium oxide as a support for catalysts Evolution of the texture and structure on calcination in static air". In: *Applied Catalysis* 78 (1991), pp. 79–96. DOI: 10.1016/0166-9834(91)80090-J.

[39] T. Kondo, Y. Takigawa, and T. Sakuma. "High-temperature tensile ductility in TZP and TiO_2-doped TZP". In: *Materials Science and Engineering A* 231 (1997), pp. 163–169. DOI: 10.1016/S0921-5093(97)00072-5.

[40] R. Reisfeld, M. Zelner, and A. Patra. "Fluorescence study of zirconia films doped by Eu^{3+}, Tb^{3+} and Sm^{3+} and their comparison with silica films". In: *Journal of Alloys and Compounds* 300-301 (2000), pp. 147–151. DOI: 10.1016/S0925-8388(99)00714-8.

[41] S.H. Yang et al. "Preparation of yttria-stabilized tetragonal zirconia ceramics for optical ferrule". In: *Journal of Materials Synthesis and Processing* 9 (2001), pp. 275–279. DOI: 10.1023/A:1015203602403.

[42] S. Lawson. "Environmental Degradation of Zirconia Ceramics". In: *Journal of the European Ceramic Society* 15 (1995), pp. 485–502. DOI: 10.1016/0955-2219(95)00035-S.

[43] U. Gross and V. Strunz. "The interface of various glasses and glass ceramics with a bony implantation bed". In: *Journal of Biomedical Materials Research* 19 (1985), pp. 251–271. DOI: 10.1002/jbm.820190308.

[44] W.A. Beresford. *Chondroid Bone, Secondary Cartilage and Metaplasia*. Urban & Schwarzenberg, 1981. ISBN: 978-0-806-70261-2.

[45] X. Liu et al. "Bioactivity and cytocompatibility of zirconia (ZrO_2) films fabricated by cathodic arc deposition." In: *Biomaterials* 27 (2006), pp. 3904–3911. DOI: 10.1016/j.biomaterials.2006.03.007.

[46] J. Chevalier. "What future for zirconia as a biomaterial?" In: *Biomaterials* 27 (2006), pp. 535–543. DOI: 10.1016/j.biomaterials.2005.07.034.

[47] J. Caton et al. "Phase Transformation in Zirconia Heads after THA Myth or Reality". In: *Proceedings of the Ninth BIOLOX Symposium*. 2004, pp. 73–74.

[48] J. Allain et al. "Poor eighth year survival of cemented zirconia-polyethylene total hip replacements". In: *The Journal of Bone and Joint Surgery* 81 (1999), pp. 835–842. DOI: 10.1302/0301-620X.81B5.9454.

[49] K. Haraguchi et al. "Phase transformation of a zirconia cermaic head after total hip arthroplasty". In: *The Journal of Bone and Joint Surgery* 83 (2001), pp. 996–1000. DOI: 10.1302/0301-620X.83B7.12122.

[50] S.A. Catledge et al. "Surface crystalline phases and nanoindentation hardness of explanted zirconia femoral heads". In: *Journal of Materials Science: Materials in Medicine* 14 (2003), pp. 863–867. DOI: 10.1023/A:1025678525474.

[51] S. Röker et al. "Novel 3D biomaterials for tissue engineering based on collagen and macroporous ceramics". In: *Materialwissenschaft und Werkstofftechnik* 40 (2009), pp. 54–60. DOI: 10.1002/mawe.200800413.

[52] K. Suck, L. Behr, and M. Fischer. "Cultivation of MC3T3–E1 cells on a newly developed material (Sponceram®) using a rotating bed system bioreactor". In: *Journal of Biomedical Materials Research Part A* 80 (2006), pp. 268–275. DOI: 10.1002/jbm.a.30965.

[53] T. Albrektsson and C. Johansson. "Osteoinduction, osteoconduction and osseointegration". In: *European Spine Journal* 10 (2001), pp. 96–101. DOI: 10.1007/s005860100282.

[54] N. Tamari, I. Kondo, and M. Mouri. "Mechanical Properties of Tricalcium Phosphate-Zirconia Composite Ceramics". In: *Journal of the Ceramic Society of Japan* 96 (1988), pp. 106–108. DOI: 10.2109/jcersj.96.106.

[55] J.M. Wu and T.S. Yeh. "Sintering of hydroxylapatite-zirconia composite materials". In: *Journal of Materials Science* 23 (1988), pp. 3771–3777. DOI: 10.1007/BF00540526.

[56] G. Gritzner and C. Puchner. "V_2O_5, Nb_{205} and Ta_{205} Doped Zirconia Ceramics". In: *Journal of the European Ceramic Society* 13 (1994), pp. 387–394. DOI: 10.1016/0955-2219(94)90015-9.

[57] F.M. Pitek and C.G. Levi. "Opportunities for TBCs in the ZrO_2–$YO_{1.5}$–$TaO_{2.5}$ system". In: *Surface and Coatings Technology* 201 (2007), pp. 6044–6050. DOI: 10.1016/j.surfcoat.2006.11.011.

[58] M.H. Habibi et al. "An investigation on hot corrosion behavior of YSZ-Ta_2O_5 in Na_2SO_4 + V_2O_5 salt at 1100°C". In: *Corrosion Science* 75 (2013), pp. 409–414. DOI: 10.1016/j.corsci.2013.06.025.

[59] S. Raghavan and M.J. Mayo. "The hot corrosion resistance of 20 mol% $YTaO_4$ stabilized tetragonal zirconia and 14 mol% Ta_2O_5 stabilized orthorhombic zirconia for thermal barrier coating applications". In: *Surface and Coatings Technology* 160 (2002), pp. 187–196. DOI: 10.1016/S0257-8972(02)00393-6.

[60] A.M. Limarga et al. "Thermal conductivity of single- and multi-phase compositions in the ZrO_2–Y_2O_3–Ta_2O_5 system". In: *Journal of the European Ceramic Society* 34 (2014), pp. 3085–3094. DOI: 10.1016/j.jeurceramsoc.2014.03.013.

[61] H. Bestgen, R. Chaim, and A.H. Heuer. "Thin-Foil Phase Transformations of Tetragonal ZrO_2 in a ZrO_2-8wt% Y_2O_3 Alloy". In: *Journal of the American Ceramic Society* 71 (1988), pp. 826–831. DOI: 10.1111/j.1151-2916.1988.tb07530.x.

[62] E.H. Kisi, C.J. Howard, and R.J. Hill. "Crystal Structure of orthorhombic zirconia in partially stabilized zirconia". In: *Journal of the American Ceramic Society* 60 (1989), pp. 1757–1760. DOI: 10.1111/j.1151-2916.1989.tb06322.x.

[63] C.J. Howard et al. "Neutron Diffraction Studies of Phase Transformations between Tetragonal and Orthorhombic Zirconia in Magnesia-Partially-Stabilized Zirconia". In: *Journal of the American Ceramic Society* 73 (1990), pp. 2828–2833. DOI: 10.1111/j.1151-2916.1990.tb06682.x.

[64] C.J. Howard, E.H. Kisi, and O. Ohtaka. "Crystal structures of two orthorhombic zirconias". In: *Journal of the American Ceramic Society* 23 (1991), pp. 2321–2323. DOI: 10.1111/j.1151-2916.1991.tb08307.x.

[65] J. C. Ray, P. Pramanik, and S. Ram. "Formation of Cr^{3+} stabilized ZrO_2 nanocrystals in a single cubic metastable phase by a novel chemical route with a sucrose-polyvinyl alcohol polymer matrix". In: *Materials Letters* 48 (2001), pp. 281–291. DOI: 10.1016/S0167-577X(00)00316-5.

[66] B. Samaranch et al. "Synthesis and Characterization of Ta_2O_5–ZrO_2 Systems: Structure, Surface Acidity, and Catalytic Properties." In: *Chemistry of materials* 19 (2007), pp. 1445–1451. DOI: 10.1021/cm062704z.

[67] J.C. Ray, A.B. Panda, and P. Pramanik. "Chemical synthesis of nanocrystals of tantalum ion-doped tetragonal zirconia". In: *Materials Letters* 3 (2002), pp. 145–150. DOI: 10.1016/S0167-577X(01)00465-7.

[68] A.K. Bhattacharya et al. "Ta_2O_5–Y_2O_3–ZrO_2 system: Experimental study and preliminary thermodynamic description". In: *Journal of the European Ceramic Society* 31 (2011), pp. 249–257. DOI: 10.1016/j.jeurceramsoc.2010.09.009.

[69] C. Zheng and A.R. West. "Compound and solid-solution formation, phase equilibria and electrical properties in the ceramic system ZrO2-La2O3-Ta2O5". In: *Journal of Materials Chemistry* 1 (1991), p. 163. DOI: 10.1039/jm9910100163.

[70] S.P.S. Badwal, M.J. Bannister, and R.H.J. Hannink. *Science and Tecnology of Zirconia V*. Technomic Publishing, 1993. ISBN: 1-55676-073-9.

[71] H. Che et al. "Mesoporous nanocrystalline zirconium oxide: novel preparation and photoluminescence property". In: *Journal of Porous Materials* 18 (2011), pp. 57–67. DOI: 10.1007/s10934-010-9356-6.

[72] U. Ciesla et al. "Highly ordered porous zirconias from surfactant-controlled syntheses: Zirconium oxide-sulfate and zirconium oxo phosphate". In: *Chemistry of materials* 11 (1999), pp. 227–234. DOI: 10.1021/cm980205v.

[73] X. Liu, G. Lu, and Z. Yan. "Preliminary Synthesis and Characterization of Mesoporous Nanocrystalline Zirconia". In: *Journal of Natural Gas Chemistry* 12 (2003), pp. 161–166.

[74] C. Sanchez et al. ""Chimie douce": A land of opportunities for the designed construction of functional inorganic and hybrid organic-inorganic nanomaterials". In: *Comptes Rendus Chimie* 13 (2010), pp. 3–39. DOI: 10.1016/j.crci.2009.06.001.

[75] J. Livage and J. Lemerle. "Transition Metal Oxide Gels and Colloids". In: *Annual Reviews of Materials Science* 12 (1982), pp. 103–122. DOI: 10.1146/annurev.ms.12.080182.000535.

[76] W. Stober, A. Fink, and E. Bohn. "Controlled growth of monodisperse silica spheres in the micron size range". In: *Journal of Colloid and Interface Science* 26 (1968), pp. 62–69. DOI: 10.1016/0021-9797(68)90272-5.

[77] M. Ebelmen. "Sur les combinaisons des acides borique et silicique avec les éthers." In: *Annales de Chimie et de Physique* 16 (1846), pp. 129–166.

[78] T. Graham. "On the properties of silicic acid and other analogous colloidal substances". In: *Journal of Chemical Society* 17 (1864), pp. 318–327. DOI: 10.1039/JS8641700318.

[79] L. Rayleigh. "Periodic precipitates". In: *Philosophical Magazine* 38 (1919), pp. 738–740. DOI: 10.1080/14786441208636008.

[80] W.Z. Ostwald. "Studien über die Bildung und Umwandlung fester Körper". In: *Zeitschrift für physikalische Chemie* 22 (1897), pp. 289–330.

[81] L.L. Hench and J.K. West. "The sol-gel Process". In: *Chemical Reviews* 90 (1990), pp. 33–72. DOI: 10.1021/cr00099a003.

[82] C.T. Kresge et al. "Ordered mesoporous molecular sieves synthsized by a liquid-crystal template mechanism". In: *Nature* 359 (1992), p. 710. DOI: 10.1038/359710a0.

[83] J.S. Beck et al. "A new family of mesoporous molecular sieves prepared with liquid crystal templates". In: *Journal of the American Chemical Society* 114 (1992), p. 10834. DOI: 10.1021/ja00053a020.

[84] S. Biz and M.L. Occelli. "Synthesis and Characterization of Mesostructured Materials". In: *Catalysis Reviews* 40 (1998), pp. 329–407. DOI: 10.1080/01614949808007111.

[85] U. Ciesla, S. Schacht, and G.D. Stucky. "Formation of a Porous Zirconium Oxo Phospate with a High Surface Area by a Surfactant-Assisted Synthesis". In: *Angewandte Chemie (International ed. in English)* 35 (1996), pp. 541–543. DOI: 10.1002/anie.199605411.

[86] G. Pacheco et al. "Mesoporous zirconia obtained with anionic templates". In: *Chemical Communications* (1997), pp. 491–492. DOI: 10.1021/la034824g.

[87] P. Yang et al. "Generalized syntheses of large-pore mesoporous metal oxides with semicrystalline frameworks". In: *Nature* 396 (1998), pp. 152–155. DOI: 10.1038/24132.

[88] M. Kang et al. "Preparation of stable mesoporous inorganic oxides via nano-replication technique". In: *Catalysis Today* 93-95 (2004), pp. 695–699. DOI: 10.1016/j.cattod.2004.06.063.

[89] B. Liu and R.T. Baker. "Factors affecting the preparation of ordered mesoporous ZrO_2 using the replica method". In: *Journal of Materials Chemistry* 18 (2008), pp. 5200–5207. DOI: 10.1039/b807620k.

[90] J.H. Smått et al. "Synthesis of micrometer sized mesoporous metal oxide spheres by nanocasting". In: *Microporous and Mesoporous Materials* 112 (2008), pp. 308–318. DOI: 10.1016/j.micromeso.2007.10.003.

[91] V.G. Kessler et al. "New insight in the role of modifying ligands in the sol-gel processing of metal alkoxide precursors: A possibility to approach new classes of materials". In: *Journal of Sol-Gel Science and Technology* 40 (2006), pp. 163–179. DOI: 10.1007/s10971-006-9209-6.

[92] S.G. Liu et al. "A facile route to synthesize mesoporous zirconia with ultra high thermal stability". In: *Materials Research Bulletin* 42 (2007), pp. 171–176. DOI: 10.1016/j.materresbull.2006.04.035.

[93] A. Dong et al. "General synthesis of mesoporous spheres of metal oxides and phosphates." In: *Journal of the American Chemical Society* 125 (2003), pp. 4976–4977. DOI: 10.1021/ja029964b.

[94] A. Tuel, S. Gontier, and R. Teissier. "Zirconium containing mesoporous silicas: new catalysts for oxidation reactions in the liquid phase". In: *Chemical Communications* (1996), pp. 651–652. DOI: 10.1039/CC9960000651.

[95] D.J. Jones et al. "Surface characterisation of zirconium-doped mesoporous silica". In: *Chemical Communications* (1997), pp. 431–432. DOI: 10.1039/A608145B.

[96] J.A. Knowles and M.J. Hudson. "Preparation and characterisation of mesoporous, high surface area zirconium(IV) oxides". In: *Chemical Communications* (1995), pp. 2083–2084. DOI: 10.1039/c39950002083.

[97] A. Kim et al. "Amphoteric surfactant templating route for mesoporous zirconia". In: *Chemical Communications* (1997), pp. 161–162. DOI: 10.1039/a604578b.

[98] M.S. Kaliszewski and A.H. Heuer. "Alcohol interaction with zirconia powders". In: *Journal of the American Ceramic Society* 73 (1990), pp. 1504–1509. DOI: 10.1111/j.1151-2916.1990.tb09787.x.

[99] J. Widoniak, S. Eiden-Assmann, and G. Maret. "Synthesis and Characterisation of Monodisperse Zirconia Particles". In: *European Journal of Inorganic Chemistry* (2005), pp. 3149–3155. DOI: 10.1002/ejic.200401025.

[100] M.A. Ballem, J.M. Córdoba, and M. Odén. "Mesoporous silica templated zirconia nanoparticles". In: *Journal of Nanoparticle Research* 13 (2011), pp. 2743–2748. DOI: 10.1007/s11051-010-0160-7.

[101] D. Chen et al. "Facile Synthesis of Monodisperse Mesoporous Zirconium Titanium Oxide Microspheres with Varying Compositions and High Surface Areas for Heavy Metal Ion Sequestration". In: *Advanced Functional Materials* 22 (2012), pp. 1966–1971. DOI: 10.1002/adfm.201102878.

[102] J. Livage, K. Doi, and C. Mazieres. "Nature and Thermal Evolution of Amorphous Hydrated Zirconium Oxide". In: *Journal of the American Ceramic Society* 51 (1968), pp. 349–353. DOI: 10.1111/j.1151-2916.1968.tb15952.x.

[103] M.A. Blesa et al. "Hydrous zirconium dioxide: interfacial properties, the formation of monodisperse spherical particles, and its crystallization at high temperatures". In: *Journal of Materials Science* 20 (1985), pp. 4601–4609. DOI: 10.1007/BF00559350.

[104] Michael Sorrentino, Lester Steinbrecher, and Fred Hazel. "The glow phenomenon in colloidal hydrous oxides". In: *Journal of Colloid and Interface Science* 31 (1969), pp. 307 –316. DOI: 10.1016/0021-9797(69)90174-X.

[105] G. Gimblett, A.A. Rahman, and K.S.W. Sing. "Thermal and related studies of some zirconia gels". In: *Journal of Chemical Technology and Biotechnology* 30 (1980), pp. 51–54. DOI: 10.1002/jctb.503300108.

[106] A.C. Pierre. *Introduction to sol-gel processing*. Kluwer Academic Publishers, 1998. ISBN: 978-1-4615-5659-6.

[107] K.S. Mazdiyasni. "Preparation of Ultra-High-Purity Submicron Refractory Oxides". In: *Journal of the American Ceramic Society* 48 (1965), pp. 372–375. DOI: 10.1111/j.1151-2916.1965.tb14764.x.

[108] D. Chen et al. "Synthesis of monodisperse mesoporous titania beads with controllable diameter, high surface areas, and variable pore diameters (14-23 nm)." In: *Journal of the American Chemical Society* 132 (2010), pp. 4438–4444. DOI: 10.1021/ja100040p.

[109] S. Eiden-Assmann, J. Widoniak, and G. Maret. "Synthesis and characterization of porous and nonporous monodisperse colloidal TiO2 particles". In: *Chemistry of Materials* 16 (2004), pp. 6–11. DOI: 10.1021/cm0348949.

[110] V. Meynen, P. Cool, and E.F. Vansant. "Verified syntheses of mesoporous materials". In: *Microporous and Mesoporous Materials* 125 (2009), pp. 170–223. DOI: 10.1016/j.micromeso.2009.03.046.

[111] A.G.S. Prado and C. Airoldi. "Different neutral surfactant template extraction routes for synthetic hexagonal mesoporous silicas". In: *Journal of Materials Chemistry* 12 (2002), pp. 3823–3826. DOI: 10.1039/b204060c.

[112] G. Sponchia et al. "Biocompatible Tailored Zirconia Mesoporous Nanoparticles with High Surface Area for Theranostic Applications". In: *Journal of Materials Chemistry B* 3 (2015), pp. 7300–7306. DOI: 10.1039/C5TB01424G.

[113] E. Burcu. *Sintering Applications*. INTECH, 2013. ISBN: 978-953-51-0974-7.

[114] P. Riello et al. "In situ reaction furnace for real-time XRD studies". In: *Journal of Synchrotron Radiation* 20 (2013), pp. 194–196. DOI: 10.1107/S0909049512039246.

[115] B.K. Kim and H. Hamaguchi. "Mode Assignments of the Raman Spectrum of Monoclinic Zirconia by Isotopic Exchange Technique". In: *Physica Status Solidi B* 203 (1997), pp. 557–563. DOI: 10.1002/1521-3951(199710)203:2<557::AID-PSSB557>3.0.CO;2-C.

[116] C. Viazzi et al. "Structural study of metastable tetragonal YSZ powders produced via a sol–gel route". In: *Journal of Alloys and Compounds* 452 (2008), pp. 377 –383. DOI: 10.1016/j.jallcom.2006.10.155.

[117] K. Fukatsu et al. "Kinetics and the role of off-stoichiometry in the environmentally driven phase transformation of commercially available zirconia femoral heads". In: *Acta Biomaterialia* 8 (2012), pp. 1639 –1647. DOI: http://dx.doi.org/10.1016/j.actbio.2011.12.019.

[118] A. Leto et al. "Bioinertness and fracture toughness evaluation of the monoclinic zirconia surface film of Oxinium™ femoral head by Raman and cathodoluminescence spectroscopy". In: *Journal of the Mechanical Behavior of Biomedical Materials* 31 (2014), pp. 135 –144. DOI: 10.1016/j.jmbbm.2013.10.026.

[119] R. Devanathan et al. "Computer simulation of defects and oxygen transport in yttria-stabilized zirconia". In: *Solid State Ionics* 177 (2006), pp. 1251 –1258. DOI: 10.1016/j.ssi.2006.06.030.

[120] V. Vonk et al. "Atomic structure and composition of the yttria-stabilized zirconia (111) surface". In: *Surface Science* 612 (2013), pp. 69 –76. DOI: 10.1016/j.susc.2013.02.014.

[121] J. Čížek et al. "Defect studies of nanocrystalline zirconia powders and sintered ceramics". In: *Physical Review B* 81 (2010), p. 024116. DOI: 10.1103/PhysRevB.81.024116.

[122] H. Ding, A.V. Virkar, and F. Liu. "Defect configuration and phase stability of cubic versus tetragonal yttria-stabilized zirconia". In: *Solid State Ionics* 215 (2012), pp. 16 –23. DOI: 10.1016/j.ssi.2012.03.014.

[123] H. Nakajima and T. Mori. "Photoluminescence excitation bands corresponding to defect states due to oxygen vacancies in yttria- stabilized zirconia". In: *Journal of Alloys and Compounds* 408 (2006), pp. 728–731. DOI: 10.1016/j.jallcom.2004.11.080.

[124] M. Boffelli et al. "Off-Stoichiometry Spectroscopic Investigations of Pure Amorphous Silica and N-Doped Silica Thin Films". In: *The Journal of Physical Chemistry C* 117 (2013), pp. 3475–3482. DOI: 10.1021/jp311697g.

[125] G. Pezzotti et al. "Quantitative assessments of residual stress fields at the surface of alumina hip joints". In: *Journal of Biomedical Materials Research Part B: Applied Biomaterials* 95B (2010), pp. 250–262. DOI: 10.1002/jbm.b.31706.

[126] G. Pezzotti et al. "On the role of oxygen vacancies and lattice strain in the tetragonal to monoclinic transformation in alumina/zirconia composites and improved environmental stability". In: *Biomaterials* 31 (2010), pp. 6901 –6908. DOI: 10.1016/j.biomaterials.2010.05.035.

[127] J.H. Hur, S. Park, and U.I. Chung. "First principles study of oxygen vacancy states in monoclinic ZrO_2: Interpretation of conduction characteristics". In: *Journal of Applied Physics* 112 (2012), p. 113719. DOI: 10.1063/1.4768894.

[128] M. Kirm et al. "Thin films of HfO_2 and ZrO_2 as potential scintillators". In: *Nuclear Instruments and Methods in Physics Research Section A: Accelerators, Spectrometers, Detectors and Associated Equipment* 537 (2005), pp. 251 –255. DOI: 10.1016/j.nima.2004.08.020.

[129] V. Kiisk et al. "Photoluminescence of sol–gel-prepared hafnia". In: *Physica B: Condensed Matter* 405 (2010), pp. 758 –762. DOI: 10.1016/j.physb.2009.09.101.

[130] N.G. Petrik, D.P. Taylor, and T.M. Orlando. "Laser-stimulated luminescence of yttria-stabilized cubic zirconia crystals". In: *Journal of Applied Physics* 85 (1999), pp. 6770–6776. DOI: 10.1063/1.370192.

[131] N. Korsunska et al. "Nanostructured Y-doped ZrO_2 powder: peculiarities of light emission under electron beam excitation". In: *Physica Status Solidi C* 11 (2014), pp. 1417–1422. DOI: 10.1002/pssc.201300597.

[132] K. Smits et al. "Comparison of ZrO_2:Y nanocrystals and macroscopic single crystal luminescence". In: *Journal of Physics: Conference Series* 93 (2007), p. 012035. DOI: 10.1088/1742-6596/93/1/012035.

[133] K. Smits et al. "Intrinsic defect related luminescence in ZrO_2". In: *Journal of Luminescence* 131 (2011), pp. 2058 –2062. DOI: 10.1016/j.jlumin.2011.05.018.

[134] J.C. Garcia et al. "Structural, electronic, and optical properties of ZrO_2 from ab initio calculations". In: *Journal of Applied Physics* 100 (2006), p. 104103. DOI: 10.1063/1.2386967.

[135] R. French et al. "Experimental and theoretical determination of the electronic structure and optical properties of three phases of ZrO_2". In: *Physical Review B* 49 (1994), pp. 5133–5142. DOI: 10.1103/PhysRevB.49.5133.

[136] C.B. Azzoni et al. "Disorder-induced optical and paramagnetic properties in zirconium dioxide: Role of low-symmetry crystal fields". In: *Physical Review B* 51 (1995), pp. 15942–15946. DOI: 10.1103/PhysRevB.51.15942.

[137] C.B. Azzoni and A. Paleari. "Sevenfold- and sixfold-coordinated Zr^{3+} ions in cubic stabilized zirconia: Crystal-field approach". In: *Physical Review B* 44 (1991), pp. 6858–6863. DOI: 10.1103/PhysRevB.44.6858.

[138] K. Smits et al. "Europium doped zirconia luminescence". In: *Optical Materials* 32 (2010), pp. 827–831. DOI: 10.1016/j.optmat.2010.03.002.

[139] W.A. Dollase. "Correction of Intensities for Preferred Orientation in Powder Diffractometry: Application of the March Model". In: *Journal of Applied Crystallography* 19 (1986), pp. 267–272. DOI: 10.1107/S0021889886089458.

[140] J. Dexpert-Ghys, M. Faucher, and J. Caro. "Site Selective Spectroscopy and Structural Analysis of Yttria-Doped Zirconias". In: *Journal of Solid State Chemistry* 192 (1984), pp. 179–192. DOI: 10.1016/0022-4596(84)90145-2.

[141] P. Bouvier et al. "High-pressure structural evolution of undoped tetragonal nanocrystalline zirconia". In: *Physical Review B* 62 (2000), pp. 8731–8737. DOI: 10.1103/PhysRevB.62.8731.

[142] M.H. Tuilier et al. "X-ray absorption study of the ZrO_2–Y_2O_3 system". In: *Journal of Solid State Chemistry* 69 (1987), pp. 153–161. DOI: 10.1016/0022-4596(87)90021-1.

[143] Yan Cong et al. "Effect of Oxygen Vacancy on Phase Transition and Photoluminescence Properties of Nanocrystalline Zirconia Synthesized by the One-Pot Reaction". In: *The Journal of Physical Chemistry C* 113 (2009), pp. 13974–13978. DOI: 10.1021/jp8103497.

[144] Y. Shen et al. "Low thermal conductivity without oxygen vacancies in equimolar $YO_{1.5}$ + $TaO_{2.5}$- and $YbO_{1.5}$+$TaO_{2.5}$-stabilized tetragonal zirconia ceramics". In: *Acta Materialia* 58 (2010), pp. 4424–4431. DOI: 10.1016/j.actamat.2010.04.040.

[145] D.J. Kim et al. "Fracture Toughness, Ionic Conductivity, and Low-Temperature Phase Stability of Tetragonal Zirconia Codoped with Yttria and Niobium Oxide". In: *Journal of the American Ceramic Society* 81 (1998), pp. 2309–2314. DOI: 10.1111/j.1151-2916.1998.tb02626.x.

[146] H.M. Rietveld. "A profile refinement method for nuclear and magnetic structures". In: *Journal of Applied Crystallography* 2 (1969), pp. 65–71. DOI: 10.1107/S0021889869006558.

[147] R.A. Young. *The Rietveld Method*. Ed. by IUCr. Oxford University Press, 1995. ISBN: 978-0-19-855912-2.

[148] Juan Rodríguez-Carvajal. "Recent advances in magnetic structure determination by neutron powder diffraction". In: *Physica B* 192 (1993), pp. 55–69. DOI: 10.1016/0921-4526(93)90108-I.

[149] G.S. Pawley. "Unit-cell refinement from powder diffraction scans". In: *Journal of Applied Crystallography* 14 (1981), pp. 357–361. DOI: 10.1107/S0021889881009618.

[150] R. Černý and V. Favre-Nicolin. "Direct space methods of structure determination from powder diffraction: Principles, guidelines and perspectives". In: *Zeitschrift fur Kristallographie* 222 (2007), pp. 105–113. DOI: 10.1524/zkri.2007.222.3-4.105.

[151] W.I.F. David and K. Shankland. "Structure determination from powder diffraction data." In: *Acta Crystallographica A* 64 (2008), pp. 52–64. DOI: 10.1107/S0108767307064252.

[152] S. Takeya et al. "Direct space methods for powder X-ray diffraction for guest-host materials: Applications to cage occupancies and guest distributions in clathrate hydrates". In: *Journal of the American Chemical Society* 132.2 (2010), pp. 524–531. ISSN: 00027863. DOI: 10.1021/ja905426e.

[153] J.J.P. Stewart. "Optimization of parameters for semiempirical methods V: Modification of NDDO approximations and application to 70 elements". In: *Journal of Molecular Modeling* 13 (2007), pp. 1173–1213. DOI: 10.1007/s00894-007-0233-4.

[154] G. E. Engel et al. "PowderSolve– a Complete Package for Crystal Structure Solution From Powder Diffraction Patterns". In: *Journal of Applied Crystallography* 32.6 (1999), pp. 1169–1179. ISSN: 0021-8898. DOI: 10.1107/S0021889899009930.

[155] B. Delley. "From molecules to solids with the DMol 3 approach". In: *Journal of Chemical Physics* 113 (2000), pp. 7756–7764. DOI: 10.1063/1.1316015.

[156] J. Andzelm, R.D. King-Smith, and G. Fitzgerald. "Geometry optimization of solids using delocalized internal coordinates". In: *Chemical Physics Letters* 335 (2001), pp. 321–326. DOI: 10.1016/S0009-2614(01)00030-6.

[157] T.A. Halgren and W.N. Lipscomb. "The synchronous-transit method for determining reaction pathways and locating molecular transition states". In: *Chemical Physics Letters* 49 (1977), pp. 225–232. DOI: 10.1016/0009-2614(77)80574-5.

[158] E.H. Kisi and C.J. Howard. "Crystal Structures of Zirconia Phases and their Inter-Relation". In: *Key Engineering Materials* 153-154 (1998), pp. 1–36. DOI: 10.4028/www.scientific.net/KEM.153-154.1.

[159] G. Trolliard, D. Mercurio, and J.M. Perez-Mato. "Martensitic phase transition in pure zirconia: A crystal chemistry viewpoint". In: *Zeitschrift fur Kristallographie* 226 (2011), pp. 264–290. DOI: 10.1524/zkri.2011.1340.

[160] S. Liu et al. "Metastable adaptive orthorhombic martensite in zirconia nanoparticles". In: *Journal of Applied Crystallography* 47 (2014), pp. 684–691. DOI: 10.1107/S1600576714003331.

[161] G. Trolliard, R. Benmechta, and D. Mercurio. "Pure orthorhombic zirconia islands grown on single-crystal sapphire substrates". In: *Acta Materialia* 55 (2007), pp. 6011–6018. DOI: 10.1016/j.actamat.2007.07.009.

[162] A. H. Heuer et al. "On the orthorhombic phase in ZrO_2-based alloys". In: *Journal of Materials Science* 24 (1989), pp. 124–132. DOI: 10.1007/BF00660943.

[163] Z. Liu et al. "HRTEM study of orthorhombic zirconia in MgO-PSZ". In: *Journal of Applied Crystallography* 36 (2003), pp. 1026–1029. DOI: 10.1107/S0021889803009075.

[164] H. Arashi and M. Ishigame. "Raman spectroscopic studies of the polymorphism in ZrO_2 at high pressures". In: *Physica Status Solidi A* 71 (1982), pp. 313–321. DOI: 10.1002/pssa.2210710203.

[165] P. Bouvier, J. Godlewski, and G. Lucazeau. "A Raman study of the nanocrystallite size effect on the pressure–temperature phase diagram of zirconia grown by zirconium-based alloys oxidation". In: *Journal of Nuclear Materials* 300 (2002), pp. 118 –126. DOI: 10.1016/S0022-3115(01)00756-5.

[166] O. Ohtaka et al. "Phase relations and equations of state of ZrO_2 under high temperature and high pressure". In: *Physical Review B* 63 (2001), p. 174108. DOI: 10.1103/PhysRevB.63.174108.

[167] J.M. Leger et al. "Pressure-induced structural phase transitions in zirconia under high pressure". In: *Physical Review B* 47 (1993), pp. 14075–14083. DOI: 10.1103/PhysRevB.47.14075.

[168] Y. Kudoh, H. Takeda, and H. Arashi. "In situ determination of crystal structure for high pressure phase of ZrO_2 using a diamond anvil and single crystal X-ray diffraction method". In: *Physics and Chemistry of Minerals* 13 (1986), pp. 233–237. DOI: 10.1007/BF00308274.

[169] J. Haines et al. "Characterization of the Cotunnite-Type Phases of Zirconia and Hafnia by Neutron Diffraction and Raman Spectroscopy". In: *Journal of the American Ceramic Society* 80 (1997), pp. 1910–1914. DOI: 10.1111/j.1151-2916.1997.tb03073.x.

[170] D.J. Kim, H.J. Jung, and I.S. Yang. "Raman Spectroscopy of Tetragonal Zirconia Solid Solutions". In: *Journal of the American Ceramic Society* 76 (1993), pp. 2106–2108. DOI: 10.1111/j.1151-2916.1993.tb08341.x.

[171] G.A. Kourouklis and E. Liarokapis. "Pressure and Temperature Dependence of the Raman Spectra of Zirconia and Hafnia". In: *Journal of the American Ceramic Society* 74 (1991), pp. 520–523. DOI: 10.1111/j.1151-2916.1991.tb04054.x.

[172] J.F. Shackelford and W. Alexander. *Materials Science and Engineering Handbook*. CRC, 2001. ISBN: 0-8493-2696-6.

[173] H. Xu and H. Guo. *Thermal Barrier Coatings*. Woodhead Publishing, 2011. ISBN: 978-1-84569-658-0.

[174] S Raghavan, H Wang, and WD Porter. "Thermal properties of zirconia co-doped with trivalent and pentavalent oxides". In: *Acta Materialia* 49 (2001), pp. 169–179. DOI: 10.1016/S1359-6454(00)00295-0.

[175] B. Lawn. *Fracture of Brittle Solids*. Cambridge University Press, 1993. ISBN: 978-0-521-40972-8.

[176] C.B. Carter and M.G. Norton. *Ceramic Materials Science and Engineering*. Springer, 2013. ISBN: 978-1-4614-3522-8.

[177] J. Chevalier et al. "Creep Behaviour of Alumina , Zirconia and Alumina". In: *Journal of the European Ceramic Society* 17 (1997), pp. 859–864. DOI: 10.1016/S0955-2219(96)00160-4.

[178] C.J. McHargue et al. *Synthesis and Properties of Advanced Materials*. Kluwer Academic Publishers, 1997. ISBN: 978-0-7923-9816-5.

[179] B. Burton. "Interface reaction controlled diffusional creep: A consideration of grain boundary dislocation climb sources". In: *Materials Science and Engineering* 10 (1972), pp. 9–14. DOI: 10.1016/0025-5416(72)90060-2.

[180] A.C.F. Cocks. "Interface reaction controlled creep". In: *Mechanics of Materials* 13 (1992), pp. 165–174. DOI: 10.1016/0167-6636(92)90044-E.

[181] A.W. Ralston et al. "Boiling Points of n-Alkyl Primary Amines". In: *Industrial and Engineering Chemistry* 32 (1940), p. 1093. DOI: 10.1021/ie50368a015.

[182] K. Horiuchi, Y. Okamoto, and H. Sakurai. "The Synthesis and Properties of a-Alkylaminoethylphosphonic Acid Derivatives". In: *The Journal of the Society of Chemical Industry* 70 (1967), pp. 1762–1765. DOI: 10.1246/nikkashi1898.70.10_1762.

[183] Y.W. Zeng et al. "Short-range structure of zirconia xerogel and aerogel, determined by wide angle X-ray scattering". In: *Journal of Non-Crystalline Solids* 155 (1993), pp. 259 –266. DOI: 10.1016/0022-3093(93)91260-A.

[184] K.S.W. Sing et al. "Reporting physisorption data for gas/solid systems with Special Reference to the Determination of Surface Area and Porosity". In: *Pure and Applied Chemistry* 57 (1985), pp. 603–619. DOI: 10.1351/pac198557040603.

[185] K.D. Collins. "Charge density-dependent strength of hydration and biological structure." In: *Biophysical Journal* 72 (1997), pp. 65–76. DOI: 10.1016/S0006-3495(97)78647-8.

[186] R. Heyrovska. "The effective radii of alkali halide ions in acqueous solutions, crystals and in the gas phase and the interpretation of Stokes radii". In: *Chemical physics letters* 163 (1989), p. 207. DOI: 10.1016/0009-2614(89)80036-3.

[187] S. Poussard et al. "Internalization and fate of silica nanoparticles in C2C12 skeletal muscle cells : evidence of a beneficial effect on myoblast fusion". In: *International Journal of Nanomedicine* 10 (2015), pp. 1479–1492. DOI: 10.2147/IJN.S74158.eCollection2015.

[188] T. Yu et al. "In Vivo Biodistribution and Pharmacokinetics of Silica Nanoparticles as a Function of Geometry, Porosity and Surface Characteristics". In: *Journal of Controlled Release* 163 (2012), pp. 46–54. DOI: 10.1016/j.biotechadv.2011.08.021.Secreted.

[189] X. Hu et al. "Multifunctional hybrid silica nanoparticles for controlled doxorubicin loading and release with thermal and pH dually response." In: *Journal of Materials Chemistry B* 1 (2013), pp. 1109–1118. DOI: 10.1039/C2TB00223J.

[190] Y. Liu et al. "Enzyme responsive drug delivery system based on mesoporous silica nanoparticles for tumor therapy in vivo". In: *Nanotechnology* 26 (2015), p. 145102. DOI: 10.1088/0957-4484/26/14/145102.

[191] L. Pan et al. "Nuclear-targeted drug delivery of tat peptide-conjugated monodisperse mesoporous silica nanoparticles". In: *Journal of the American Chemical Society* 134.13 (2012), pp. 5722–5725. DOI: 10.1021/ja211035w.

[192] Akhilesh Kumar Mishra et al. "Nanoengineered mesoporous silica nanoparticles for smart delivery of doxorubicin". In: *Journal of Nanoparticle Research* 16 (2014), p. 2515. DOI: 10.1007/s11051-014-2515-y.

[193] J. Shen et al. "Mesoporous silica nanoparticles loading doxorubicin reverse multidrug resistance: performance and mechanism". In: *Nanoscale* 3 (2011), pp. 4314–4322. DOI: 10.1039/c1nr10580a.

[194] M.M. De Villiers, P. Aramwit, and G.S. Kwon. *Nanotechnology in Drug Delivery*. Springer, 2009. ISBN: 978-0-387-77667-5.

[195] Z. Chen et al. "Mesoporous silica nanoparticles with manipulated microstructures for drug delivery". In: *Colloids and Surfaces B: Biointerfaces* 95 (2012), pp. 274–278. DOI: 10.1016/j.colsurfb.2012.03.012.